Gas and dust in the Magellanic clouds

A Thesis

Submitted for the Award of the Degree of

Doctor of Philosophy in Physics

To

Mangalore University

by

Ananta Charan Pradhan

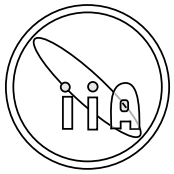

Under the Supervision of

Prof. Jayant Murthy

Indian Institute of Astrophysics
Bangalore - 560 034
India

April 2011

Declaration of Authorship

I hereby declare that the matter contained in this thesis is the result of the investigations carried out by me at Indian Institute of Astrophysics, Bangalore, under the supervision of Professor Jayant Murthy. This work has not been submitted for the award of any degree, diploma, associateship, fellowship, etc. of any university or institute.

Signed:

Date:

Certificate

This is to certify that the thesis entitled **'Gas and Dust in the Magellanic clouds'** submitted to the Mangalore University by Mr. Ananta Charan Pradhan for the award of the degree of Doctor of Philosophy in the faculty of Science, is based on the results of the investigations carried out by him under my supervision and guidance, at Indian Institute of Astrophysics. This thesis has not been submitted for the award of any degree, diploma, associateship, fellowship, etc. of any university or institute.

Signed: _____

Date: _____

Dedicated to my parents

==========

Sri. Pandab Pradhan and Smt. Kanak Pradhan

==========

Acknowledgements

It has been a pleasure to work under Prof. Jayant Murthy. I am grateful to him for giving me full freedom in research and for his guidance and attention throughout my doctoral work inspite of his hectic schedules. I am indebted to him for his patience in countless reviews and for his contribution of time and energy as my guide in this project.

I would like to express my special thanks to Dr. Amit Pathak, Dr. Rekhesh Mohan and Dr. N. V. Sujatha who stood with me in frustrating period of my research career, encouraged me patiently and extended their helping hand whenever it was needed. I thank to our group members, Rita, Shalima, Abhay, Veena, and others for many useful discussions on the subject during our group meetings almost on every Tuesday.

I am thankful to the Director of Indian Institute of Astrophysics, Prof. Siraj Hassan for giving me the opportunity to work in this institute and providing all the facilities required for my research work. I thank to the Dean Academic, Prof. Harish Bhatt, the BGS chair, Prof. S. K. Saha, the BGS Secretary, Prof. R. Ramesh and all the members of the Board of Graduate Studies for providing the necessary facilities to work comfortably in IIA. I thank Prof. B. P. Das, Prof. Dipankar Banerjee, Dr. Gajendra Pandey, Dr. Ravinder Banyal, Prof. Annapurni Subramanium, Prof. G. C. Anupama, Dr. Sivarani Thirupathi, Prof. Rajat Chaudhuri and Dr. Muthumariappan for their advice and fruitful discussions. I thank Dr. Christina Birdie, Mr. B. S. Mohan, Mr. Prabhahar and the other staffs of the library for assisting me in getting the required books and journals in time. I thank Dr. Baba Varghese, Mr. Fayaz and Mr. Ashok for their help in computer related problems.

It is my pleasure to thank my friends Tapan bhai, Bharat, Girjesh, Rumpa, Ramya, Veeresh, Amit, Nataraj, Chanduri, Krishna, Vigeesh, Blesson, Nagaraj, Uday, Malay da, Sam, Arya, Pradeep, Sajal, Jyotirmaya, Avijeet, Drisya, Indu, Ramya P., Sinduja, Ratnakumar, Prasanth, Dinesh, Hema, Arun, Suresh, Vineeth, Anantha, Smitha, Shashi, Vyas, Roopashree, Vaidehi, Narshi, Sagar, Subham and many

more of my juniors with whom I have shared a lot of funs and laughs apart from the various scientific discussions throughout my stay in IIA.

I thank administrative officer Dr. Kumaresan, personnel officer Mr. Narasimha Raju and the administrative staff who are cooperative making the administrative related issues very smooth. I thank Mr. Mohan Kumar, M. G. Mohan, Rajendran, John and Sandip who took good care making our stay in Bhaskara extremly gratified.

Its my pleasure to thank my nearer and dearer friends Babuni, Nandi, Ramani, Kamadev, Rudra bhai, Saumya bhai, Madhusmita didi, Kunmun didi, Subrat bhai and Papu bhai who are with me in pros and cons of my life giving me a lot of confidence and self belief. I would like to thank my friends from IISc, Sankarsan, Pratap, Chakrapani, Sabya, Khatei bhai, Sudhansu bhai, Bapina bhai and Rama bhai for providing joyful atmospheres by arranging weekend cricket matches, badminton tournaments, picnics and champagne parties which were essential to cherish the weekend.

I am extremely thankful to Prof. Balakrishna and Prof. Dharmaprakash of department of physics for their suggestions during registration, conduction of colloquium and other University formalities. I sincerely thank to the Mrs Anita and other administrative staffs of the Mangalore University for helping me at all stages of communications and official procedures.

Most especially, I express my gratitudes to my parents and many many many .. .. thanks to my wife Madhulita Das (Rinky) for *everything*.

List of Publications

1. "Far Ultraviolet Diffuse emission from the Large Magellanic Cloud", **Ananta C. Pradhan**, Amit Pathak, & Jayant Murthy, 2010, **ApJ Letters**, 718, 141 – 144.

2. "Survey of O VI absorption in the Large Magellanic Cloud", Amit Pathak, **Ananta C. Pradhan**, Sujatha, N. V. & Jayant Murthy, 2010, **MNRAS**, 412, 1105 – 1122.

3. "Observations of Far Ultraviolet Diffuse Emission from the Small Magellanic Cloud", **Ananta C. Pradhan**, Jayant Murthy & Amit Pathak, 2011, **ApJ**,743, 80.

4. "Properties of O VI emitting symbiotic stars in the Small Magellanic Cloud", Amit Pathak, Robin Shelton, **Ananta C. Pradhan** & Jayant Murthy, submitted in **MNRAS**.

5. "New light on star birthplace", **Ananta C. Pradhan**, Amit Pathak, & Jayant Murthy, **Nature India**, doi:10.1038/nindia.2010.96; Published online.

6. "Far Ultraviolet Characteristics of the Interstellar Medium of the Magellanic Clouds", Amit Pathak, **Ananta C. Pradhan** & Jayant Murthy, Book Chapter, Nova Science Publishers, Hauppauge, NY 11788-3619, USA.

Presentations

1. Formation of Interstellar Dust.
   Astrosat meeting, 2007, Christ University, Bangalore, India.

2. Data Analysis by Aladin and Simbad.
   Astrosat meeting, 2007, Christ University, Bangalore, India.

3. Formation of Interstellar Dust.
   Young Astronomer Meet, 2007, IIA, Bangalore, India.

4. Ultraviolet Absorption Line Analysis of a **O** type star: BD602522.
   9th COSPAR Capacity building Workshop on Space Optical and UV Astronomy, 2008, Kuala Lumpur, Malaysia.

5. Extinction Mapping through Broad Band Photometry.
   Young Astronomer Meet, 2009, IIT, Kharagpur, India.

6. Extinction Mapping through Broad Band Photometry.
   Dust Workshop, Vainu Bappu Observatory, Kavalur, India, 2009.

7. Far Ultraviolet Diffuse emission from the Large Magellanic Cloud.
   National Space Science Symposium, 2010, Saurashtra University, Rajkot, India.

8. Far Ultraviolet Diffuse emission from the Large Magellanic Cloud.
   Wittfest: Origins & Evolution of Dust, 2010, University of Toledo, USA.

9. Observations of Far Ultraviolet Diffuse emission from the Small Magellanic Cloud.
   Astronomical Society of India, 2011, Pt. Ravishankar Shukla University, Raipur, India.

Abstract

The Magellanic Clouds (MCs) are nearby irregular dwarf galaxies where the gas and dust is known to be different from the Milky Way due to a low metallicity and high gas-to-dust ratio. We have presented the first observations of the far ultraviolet diffuse radiation in the Magellanic Clouds and have shown that it is predominantly due to scattering of starlight from interstellar dust grains. We have also presented a survey of OVI absorption in the Large Magellanic Cloud (LMC), a tracer of hot gas in the interstellar medium (ISM).

We have used serendipitous observations made with the *Far Ultraviolet Spectroscopic Explorer (FUSE)* to measure the diffuse FUV (1000 – 1150 Å) radiations from the MCs. We have analyzed a complete set of *FUSE* data in and around the MCs and obtained 81 suitable FUV diffuse observations in different parts of the LMC and 30 observations in the Small Magellanic Cloud (SMC). These observations are bright, patchy and cover important regions of the MCs with intensities that range from around 10^3 photons cm^{-2} s^{-1} sr^{-1} Å^{-1} to as high as 3×10^5 photons cm^{-2} s^{-1} sr^{-1} Å^{-1}. We also found that the diffuse light in some regions is due to light coming from distant stars scattered by local dust.

A strong correlation between *FUSE* diffuse radiation and the diffuse radiation measured from *Ultraviolet Imaging Telescope (UIT)* was obtained and, based on this, we estimated the contribution of FUV diffuse radiation to the total integrated flux in the MCs. The fraction of the diffuse emission is typically 5%–20% of the total at 1100 Å in the LMC and 34% to 44% in the SMC. In all cases, the behaviour of the diffuse fraction is almost the same, rising by same factor as that of the albedo over the wavelength range of 1000 – 1615 Å. We also found a good correlation between the FUV diffuse emission and Hα emission in the H II regions of the SMC.

UV absorption lines produced by collisional ionization are used to study the hot ISM. O VI is one such ion which is produced at a temperature of 10^6 degrees. We have used high resolution absorption spectra obtained by *FUSE* for 70 lines of sight and presented

a wide survey of O VI column density measurements for the LMC. The column density varies from a minimum of log N(O VI) = 13.72 atoms cm^{-2} to a maximum value of log N(O VI) = 14.57 atoms cm^{-2}. We found a high abundance of O VI in both active (superbubbles) and inactive regions of the LMC. The abundance and properties of OVI absorption are similar in the LMC and the Milky Way (MW) despite the fact that the LMC has lower metallicity than the MW. O VI absorption in the LMC does not correlate with Hα (warm gas) or X-ray (hot gas) but correlates with X-ray emission in the 30 Doradus region, a star forming region of the LMC and decreases with increase in angular distance from the star cluster R136 suggesting that the strength of the stellar wind from the central cluster decreases outwards.

Contents

List of Figures

List of Tables

Abbreviations

ApJ	**A**stro**p**hysical **J**ournal
ApJL	**A**stro**p**hysical **J**ournal **L**etters
ApJS	**A**stro**p**hysical **J**ournal **S**upplement Series
A&A	**A**stronomy & **A**strophysics
MNRAS	**M**onthly **N**otices of the **R**oyal **A**stronomical **S**ociety
AJ	**A**stronomical **J**ournal
PASJ	**P**ublications of the **A**stronomical **S**ociety of **J**apan
PASP	**P**ublications of the **A**stronomical **S**ociety of **P**acific
BASI	**B**ulletin of the **A**stronomical **S**ociety of **I**ndia
BAIN	**B**ulletin of the **A**stronomical **I**nstitutes of the **N**etherlands
A&SS	**A**strophysics and **S**pace **S**cience
ARA&A	**A**nnual **R**eview of **A**stronomy & **A**strophysics
A&AS	**A**stronomy & **A**strophysics **S**upplement Series
SSR	**S**pace **S**cience **R**eviews
IAU	**I**nternational **A**stronomical **U**nion

Chapter 1

Interstellar Medium

Interstellar medium (ISM) is the region between the stars and is composed of 99% gas (atoms, molecules, ions, and electrons) and 1% dust by mass. Of the 99% gas about 89% is hydrogen, 9% is helium and 2% are metals (elements heavier than hydrogen and helium). Apart from the gas and dust, cosmic rays and magnetic fields are also components of the ISM. The ISM has very low density with an average density of 1 atom per cubic centimeter (cc) although it fluctuates up to a million atoms per cc in some regions, where as the best man made vacuum has 10^{12} atoms per cc. The total mass of gas and dust in the ISM is about 10% – 15% of the total mass of the visible matter in the Milky Way (MW). Information about the ISM is obtained by the spectroscopic analysis of the lines produced by the atoms, ions, and molecules present in it. Although it does not shine brightly like stars, it does play an important role in regulating the physical and chemical processes of the Galaxy. The constituents of the ISM and their interactions in our Galaxy have been described in an excellent review by Ferriere (2001).

1.1 History of the ISM

In the late eighteenth century, Sir William Herschel noticed dark patches in between the arbitrarily distributed stars which he described as 'holes in the heavens'. The deep night sky photographic surveys of Edward Barnard showed many more such dark regions with variety of shapes and sizes. Then it was realized that these dark regions or holes are due to dark clouds of interstellar matter obscuring the stars behind them. The first observational evidence of existence of the ISM came from the discovery of Hartmann (1904) in which he found stationary absorption lines of Ca II (3934 Å) in the spectrum of the spectroscopic binary star δ Orionis. To his surprise, he found that these lines were not undergoing periodically varying Doppler shift like broad absorption lines of stars. This fact evinced that these lines must have been produced by the interstellar matter but not by the stars. Further more such stationary lines were detected in spectra of bright O and B type stars revealing presence of several intervening clouds in the line of sight (Beals 1936; Adams 1949). Later on Trumpler (1930) provided the evidence for the existence of interstellar absorption and scattering by the pervasive ISM which led to the confirmation of the presence of interstellar dust.

1.2 ISM Star Cycle

The structure of the ISM is determined by the interplay between massive stars and the ISM. The stars are formed from the coldest and densest molecular gas in the ISM, where the conditions are favorable for the formation of stars. The matter inside the star undergoes a series of thermonuclear reactions, which enriches heavy elements in it. These elements are returned to the ISM through cataclysmic processes like powerful stellar winds, supernova explosions or through mass ejection in the red giant phase of relatively less mass stars. By these methods, the expulsion of matter from the star is accompanied by release of huge amount of energy. This energy generates turbulent motions that stirs the ISM to maintain its hetergenous structure and also causes the heating of the ISM. Under suitable condition of temperature and pressure, the ISM forms molecular clouds that are prone to star

TABLE 1.1: Components of the Interstellar Medium

Components	Fractional Volume	Temperature (K)	Density (atoms/cm^3)	State of Hydrogen
Molecular clouds	$< 1\%$	10 – 20	10^2 – 10^6	molecular
Cold Neutral	1% – 5%	50 – 100	20 – 50	neutral atomic
Warm Neutral	10% – 20%	6000 – 10000	0.2 – 0.5	neutral atomic
Diffuse Ionized	20% – 50%	8000	0.2 – 0.5	ionized
H II regions	$< 1\%$	10^4	10^2 – 10^4	ionized
Hot Ionized	30% – 70%	10^6 – 10^7	10^{-4} – 10^{-2}	highly ionized

formation. The material of the ISM flows in a loop continually like self regulating re-cycling of energy in ecosystem.

1.3 Gas Components of the ISM

The gases in the ISM exist in three main components: the molecular, the atomic and the hot components. The molecular components of the ISM consist primarily of diatomic molecules and a few polyatomic species. The atomic components include both the cold neutral medium and warm neutral medium where as the hot components include three phases: Warm Ionized Medium, diffuse ionized medium and hot ionized medium. The main parameters of these components are listed in Table 1.1.

1.3.1 Molecular Gas

The first molecules (CH, CH^+, and CN) in the ISM were discovered in the optical spectra of stars in 1930. The molecular gases in the ISM are present in the interior of dark, dense clouds which are shielded from the radiative dissociations by ultraviolet (UV) photons and are cold enough to avoid collisional dissociation. These clouds are very cold having a temperature of 10 – 20 K, measured from the peak intensity of CO emission lines (Goldsmith 1987), densities of 10^2 – 10^6 cm^{-3}, occupy $\leq 1.0\%$ volume of the ISM and comprise of 30% of the mass of the

ISM. Most of them are gravitationally bound and are the sites of star formation. The wealth of information on the spatial distribution, physics and chemistry of molecules in the ISM were accumulated after the vast advancement of UV astronomy, particularly by the launch of *Copernicus Satellite*, *International Ultraviolet Explorer (IUE)*, *Far Ultraviolet Spectroscopic Explorer (FUSE)*, and *Hubble Space Telescope (HST)*. The most abundant molecules like H_2 (Carruthers 1970) and CO (Smith & Stecher 1971) were identified from the UV spectrum. Although UV and optical absorption lines are crucial in understanding the interstellar molecules, it is not possible to probe the interior of the molecular clouds at these wavelengths as the interstellar dust associated with the molecules obscure them. Infrared (IR) and radio waves are used to collect valuable information about these complex environments. One can get the knowledge of temperature, density and identify the other molecules present in molecular clouds through IR spectroscopy. H_2 molecule does not possess permanent electric dipole moment to be observed directly by radiao telescopes. The rotational transition lines of CO at radio wavelengths, 2.6 and 1.33 mm are used to trace the H_2 molecule (Scoville & Sanders 1987) as CO luminosity to H_2 ratio is roughly constant in the ISM.

1.3.2 Atomic Gas

The atomic component of the ISM exists in two phases with comparable thermal pressure but with different temperature and density (Field et al. 1969); the cold neutral medium (CNM) and the warm neutral medium (WNM). The neutral component of the ISM mostly includes the neutral hydrogen atom (H I) which was first detected from the 21 cm emission (Ewen & Purcell 1951). The study of the CNM and WNM are mainly possible due to the detection of the 21 cm radio line (ν = 1420 MHz) arising from the hyperfine splitting of the ground state of hydrogen when the spin of electron flips from parallel to anti-parallel state. This 21 cm emission spectra is used to differentiate between the CNM and WNM. The narrow peaks seen in 21 cm emission and absorption is produced in the CNM where as the broader emission feature is due to the WNM. The 21 cm emission line is also

used to determine the column density of H I, N(H I) which is given by the formula,

$$N(HI) \simeq 1.8224 \times 10^{18} \int \Delta T_B(\nu) d\nu \quad atoms/cm^2/(Kkms^{-1}), \tag{1.1}$$

where ΔT_B is the brightness temperature above the background continuum and for smooth profile like Gaussian,

$$N(HI) \simeq 1.8224 \times 10^{18} \Delta T_B \Delta\nu \quad atoms/cm^2, \tag{1.2}$$

where $\Delta\nu$ is full width at half maximum (FWHM) in kms^{-1}.

The cold hydrogen gas is distributed in sheets and filaments and the main tracers are UV absorption lines (Lyman series lines) seen towards bright stars or quasars. The temperature of the CNM is T $\geq$ 50 K (Wolfire et al. 1995). The CNM density is 20 – 50 cm^{-3} and occupies 1% – 5% of the volume of the ISM. The interstellar Lyα line (λ = 1216 Å) that arises due to absorption of UV photons is widely used in imaging studies of local as well as distant galaxies.

The WNM is located mainly in the interface region (photodissociation regions) of H II region and molecular clouds and occupies 10% – 20% of the volume of the ISM. The estimated temperature of the WNM, T $\sim$ 8000 K (Dickey et al. 1978; Kulkarni & Heiles 1987) and density is 0.2 – 0.5 atoms/cm^{-3}.

1.3.3 Ionized Gas

A large fraction of the ISM is filled with ionized gas and the ionization is due to the far ultraviolet radiation of hot stars or by high energy charge particles. The ionized gas is classified into three types: the H II regions, the diffuse ionized medium (DIM) and the hot interstellar medium (HIM).

The hot blue O, B stars emit strong UV radiation that ionize the surrounding hydrogen atoms creating a completely ionized region called H II region. The central star within the H I cloud ionizes a sphere, called Stromgren sphere that

grows with time until an equilibrium between ionization and recombination is reached. The typical temperature of a H II region is around 10,000 K (Anderson et al. 2009) and few examples of H II region are Orion Nebula with a size of 500 pc and the Tarantula nebula in the Large Magellanic Cloud (LMC) with a size of 200 pc. Various types of emissions that characterize the H II regions are continuum emission (free-free radiation, free-bound radiation, and two photon radiation), dust scattered radiation and the radiation from the radio recombination lines and forbidden lines (Lequeux 2004). The notable line in this region is Hα (λ = 6563 Å) emitted by atomic hydrogen. The H II region occupies $\leq$ 1% of the volume of the ISM and its density is 10^2 – 10^4 atoms/cm^3.

Diffused ionized gas exists outside the H II regions and is originated either from leaks of ionized gas out of regions due to champagne effect or from ionization by UV radiation of isolated hot stars. Hα photographic survey (Sivan 1974) and more sensitive Hα spectroscopic scans (Roesler et al. 1978) showed that diffuse Hα exists in all direction outside the H II region. High resolution map of this regions display a complex structure made of patches, filaments and loops (Reynolds 1987). The temperature of the diffuse gas is approximately 8000 K that is measured from the width of the Hα and [S II] (λ = 6716 Å) emission line (Reynolds 1985). It occupies 20% – 50% of the volume of the ISM and its density is 0.2 – 0.5 atoms/cm^3.

The existence of hot gas in the ISM was discovered by Spitzer (1956). The ISM contains huge amount of very hot gas, with temperature T $\geq$ 10^6 K that is traced via UV and X-ray observations (Yao et al. 2009). It occupies very low density of 10^{-2} – 10^{-4} atoms/cm^3 and a high volume of 30% – 70% of the ISM. The hot gas is produced by supernova explosions or by powerful winds from young, hot stars (McCray & Snow 1979; Spitzer 1990). The best tracers of hot gases are the O VI doublet (at λ = 1032 & 1038 Å) and N V doublet (at λ = 1239 & 1243 Å) which have measured ionization temperature of $\sim$ 10^6 K. The presence of such a hot gas was borne out by X-ray and UV observations. Some X-ray observations are, the study of O VII and O VIII by *Chandra* (Yao et al. 2009) and detection of 0.25 keV soft X-ray backgrounds in Draco Nebula by *ROSAT* (Burrows & Mendenhall 1991). Similar observations are made with UV satellites such as analysis of absorption lines of hot gas by *Copernicus* (Jenkins & Meloy 1974), analysis of N V line by

IUE (Sembach & Savage 1992) and *FUSE* (Savage et al. 2003; Bowen et al. 2008). All these observations demonstrate the existence of hot gas at higher temperature of few million degrees.

One of the most important ion in the ISM is five times ionized oxygen atom (O VI), produced at a temperatures of about 3×10^5 K (Cox 2005). Such temperatures are found at the interface of hot (T $>$ 10^6 K) and warm (T $\sim$ 10^4 K) ionized gas in the ISM. Thus, O VI absorption lines at 1031.9 Å and 1037.6 Å are crucial diagnostics of the energetic processes of interface environments in the ISM of galaxies. The gas at such temperatures is cooling radiatively and the cooling is essentially independent of density, metallicity and the heating mechanism (Edgar & Chevalier 1986; Heckman et al. 2002). O VI formation by photo-ionization is unable to explain the observed abundances, given the energy of photons needed to get such high ionization (114 eV). O VI is mostly produced by shock heating and is collisionally ionized (Indebetouw & Shull 2004).

1.4 Dust

Interstellar dust plays an important role in the astrophysics of the ISM. Dust grains are formed mainly in the cool atmospheres of red giant and super giant stars, and in the cores of dense molecular cloud as well as during the cataclysmic events such as novae and supernovae outbursts, where the temperature and pressure are suitable for the condensation of carbonaceous and silicate compounds. They constitute 1% by mass of the ISM and their sizes range from a few nanometers to microns. Despite of a small contribution to the ISM mass, their ubiquitous presence not only affects the appearance of the star and galaxies but also plays a major role in thermodynamics and chemistry of the ISM. Understanding the distribution and properties of dust is essential in order to study the spectra of any of the celestial objects. It causes the formation of stars from atomic gas and serves as the sites of molecular hydrogen formation. Interstellar dust is formed due to condensation of heavier elements, C, Si, N, O, Mg, S, Fe, Al which is confirmed from their depletion from the gas phase of the ISM (Jenkins 1987; Van Steenberg & Shull

1988). The compounds of silicates, Graphites and some organic compounds are also locked up in the bulk of the dust grains.

Presence of dust grains in the ISM is manifested through extinction, reddening and polarization of starlight, reflection nebulae, X-ray halos around X-ray sources, light echos around novae and supernovae, the thermal infrared emissions from Galaxy, and the selective depletion of refractory elements from the gas phase of the ISM (Mathis 1990).

Extinction occurs due to absorption and scattering of starlight by the dust grains. The reddening is due to more scattering of blue light than red light by dust thus, by making the star light of distant star to appear as red. It can be measured by comparing the observed color of a star to its intrinsic color provided the spectral type of the star is known. Similarly, polarization of star light is due to elongated and partially aligned dust grains. Recent enhanced spectroscopic observations of dust in UV, visible, and IR incorporated with various grain models, have increased our knowledge about dust composition, size, shape, distribution as well as the absorption, emission and scattering properties.

1.4.1 Extinction

Interstellar extinction is the combined effect of the absorption and scattering, and is the best-studied property of dust grain as it covers a wide range of wavelengths extending from near-IR to vacuum UV. The study of the wavelength dependence of extinction is a diagnostic of the grain size distribution and composition. Observationally, extinction is measured by pair method; comparing two similar stars of same spectral type and luminosity class where one is heavily affected by reddening and other is absolutely free from reddening. Interstellar extinction in magnitude at wavelength λ is given by,

$$A_\lambda = -2.5log(F_\lambda/F_\lambda^0) = 2.5log(e^\tau) = 1.086\tau \tag{1.3}$$

where F^0_λ is the flux at zero reddening, F_λ is the flux of the reddened star and τ is optical depth. Since the compared pair of stars are never be at the same distance, the extinction A_λ is normalized to optical V band to give normalized extinction, $A_{\lambda-V}$ and to compare the λ-dependence of extinction at different sight lines, $A_{\lambda-V}$ is again normalized by a factor, related to dust; the optical color excess E(B-V) and this yields the most commonly found form for "extinction curves",

$$\frac{E(\lambda - V)}{E(B - V)} = \frac{A_\lambda - A_V}{E(B - V)} \tag{1.4}$$

The total extinction is measured by A_V and the ratio of total to selective extinction is termed as $R_V = \frac{E(\infty,V)}{E(B-V)} = \frac{A_V}{E(B-V)}$, where it is assumed that the extinction at infinite wavelength is zero. R_V characterizes the slope of extinction curve in the optical region ($\lambda = 4400$ – 5500 Å). The typical value of R_V for the MW is 3.1 but it varies from 2.1 to 5.6. Cardelli et al. (1989) have derived a unified parameterized formula for the extinction curve known as 'CCM extinction law' that depends only on R_V and the formula is given by

$$\frac{A_\lambda}{A_V} = a(x) + \frac{b(x)}{R_V} \tag{1.5}$$

where a(x) and b(x) are coefficients that have unique value at a given wave number x (λ^{-1}) and R_V is steep in the diffuse cloud and increases towards the denser clouds.

The regional variation in the optical properties of interstellar dust gives rise to change in the shape of the extinction curve. Fitzpatrick & Massa (1988) characterized this variation by a three component empirical model,

$$\frac{E(\lambda - V)}{E(B - V)} = c_1 + c_2\lambda^{-1} + c_3 D(\lambda^{-1}, \gamma, \lambda_0^{-1}) + c_4 F(\lambda^{-1}) \tag{1.6}$$

where c_1, c_2, c_3, and c_4 are parameters depending on the line of sight. $D(\lambda^{-1}, \gamma, \lambda_0^{-1})$ is Drude profile that represents 2175 Å bump of the extinction curve and

$$D(\lambda^{-1}, \gamma, \lambda_0^{-1}) = \frac{\lambda^{-2}}{(\lambda^{-2} - \lambda_0^{-2})^2 + \gamma^2\lambda^{-2}} \tag{1.7}$$

where λ_0 is the central wavelength (2175 Å) of the bump and γ is the broadening parameter *i.e.*, the full width half maximum of the profile. The FUV rise of the

extinction curve is represented by a polynomial, F(λ^{-1}) where

$$F(\lambda^{-1}) = 0.539(\lambda^{-1} - 5.9)^2 + 0.0564(\lambda^{-1} - 5.9)^3 \tag{1.8}$$

F(λ) = 0 for $\lambda^{-1} < 5.9$ μm and its coefficient c_4 gives the strength of the FUV rise.

Several theoretical dust models have come up considering a specific composition and size distribution of the dust grain to explain various part of the extinction curve. Assuming the dust grains as spheres of radius 'a' and column density N_d, the extinction is given by,

$$A_\lambda = 1.086\ N_d\ \sigma_e = 1.086\ N_d\ \pi\ a^2\ Q_e \tag{1.9}$$

where σ_e is the extinction cross section and Q_e is the extinction efficiency factor which is again the sum of efficiency factors for scattering and absorption *i.e.*, Q_e = Q_s + Q_a. Determination of A_λ in a model depends on the evaluation of Q_a and Q_s which depend on a dimensionless size parameter 'X' and a composition parameter 'm'(refractive index of the grain material) where

$$X = \frac{2\pi a}{\lambda} \quad and \quad m = n - ik \tag{1.10}$$

For small spherical grains, X $\ll$ 1 (Bohren & Huffman 1983) and the efficiency factors are given by,

$$Q_a \simeq 4XIm\left(\frac{m^2-1}{m^2+2}\right) \quad \& \quad Q_s \simeq \frac{8}{3}X^4 Re\left(\frac{m^2-1}{m^2+2}\right) \tag{1.11}$$

In case of pure dielectric grains, 'm' is real, $Q_a = 0$ and $Q_s \propto \lambda^{-4}$. The dielectric grain with size smaller than wavelength undergoes Rayleigh scattering. For dust grains containing weakly absorbing material, $Q_a \propto \lambda^{-1}$ and $Q_s \propto \lambda^{-4}$ and the wavelength dependence of extinction may be dominated by either scattering or absorption. The extinction will be neutral for grains much larger than the wavelengths.

1.4.2 The Average Extinction Curve

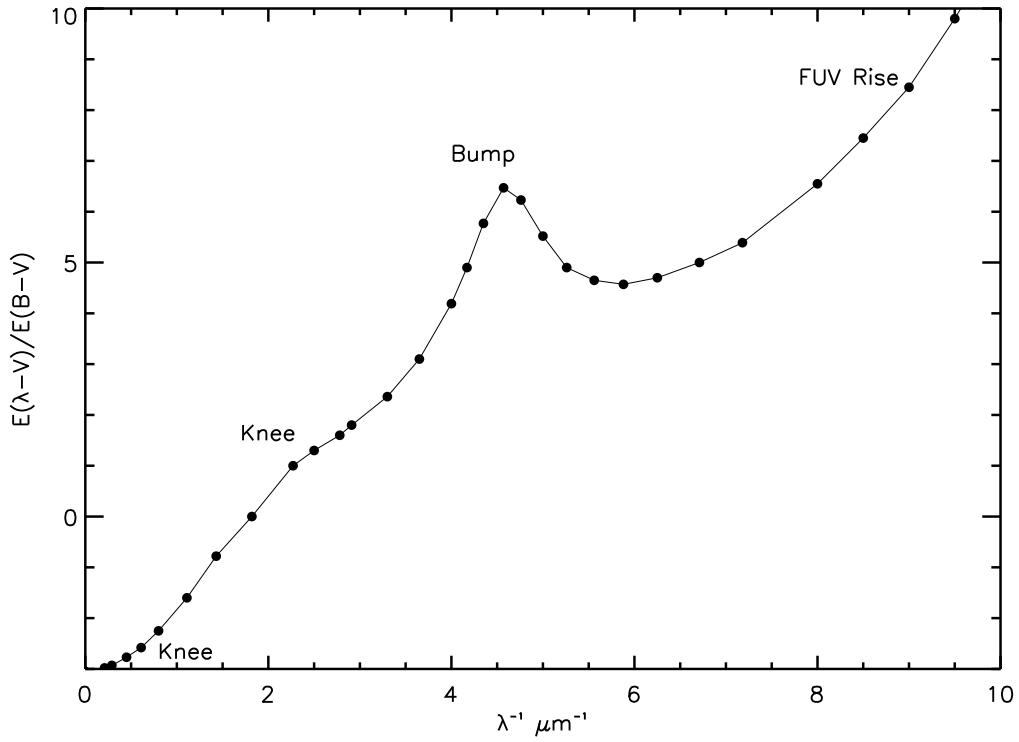

FIGURE 1.1: The average extinction curve in the spectral range 0.2-10 μm^{-1}.

The average interstellar extinction curve from the near IR to UV is shown in Figure 1.1 (Cardelli et al. 1989). It is linear in IR and visible with a 'knee' at $\lambda^{-1} \simeq 0.8$ μm^{-1}, a 'toe' at $\lambda^{-1} \simeq 2.2$ μm^{-1} and, a broad absorption feature at about $\lambda^{-1} \simeq 4.6$ μm^{-1} ($\lambda = 2175$ Å) followed by a steep rise in the far-UV at $\lambda^{-1} \simeq 10$ μm^{-1}. Several methods have been devised to explain different parts of the extinction curve assuming different size distribution and various composition of amorphous silicate and carbonaceous material The models of interstellar dust (Mathis 1996; Li & Greenberg 1997) predict that the composition of dust is mainly carbonaceous materials (Graphites and polycyclic aromatic hydrocarbons (PAHs)) and amorphous silicates and if we consider the shape and structure of the grain, it includes bare grains, grains with mantles, fluffy and porous grains. The population of the large grains are responsible for the IR and visual part of the extinction. Whittet (2003) compared the wavelength variations of the theoretical cross sections of graphite grains of sizes 0.25 μm with observed extinction curve and concluded that the linear portion of the extinction is due to the graphite grains of size 0.25

μm having refractive index, m = 1.5 - 0.05i. The 2175 Å feature is very stable and its center remains almost at same position despite the change of line of sights and this may be due to small aromatic carbonaceous (graphite) materials (Draine 1989), very likely a cosmic mixture of PAH molecules (Li & Draine 2001). The smaller grains of silicate material (Li & Draine 2001) or PAHs (Desert et al. 1990) may be responsible for the FUV rise of the extinction curve.

Interstellar extinction shows regional variation, particularly in the UV wavelength range. The reliable measurements of extragalactic extinction exists only for the Magellanic clouds (MCs) and a quantitative comparison of extinction curves between the MW and the MCs is given by Cardelli et al. (1989); Gordon et al. (2003). The LMC extinction curve displays a weaker 2175 Å bump and a stronger far-UV rise than the Galactic curve (Nandy & Morgan 1978; Koornneef & Code 1981). In the case of Small Magellanic Cloud (SMC), the extinction curves for most sightlines display a nearly linear steep rise with λ^{-1} and an extremely weak or absent 2175 Å bump (Lequeux et al. 1982; Prevot et al. 1984), suggesting that the carriers of dust in the MCs are different from the MW.

1.4.3 Size Distribution of Dust Grain

Various grain models assuming specific composition and size distribution are devised to reproduce the extinction curve. The most used grain size distribution is given by Mathis et al. (1977), the so-called MRN distribution:

$$dn^i = c_i n_H a^{-3.5} da, \quad a_{min} < a < a_{max} \tag{1.12}$$

where c_i is a normalization constant, dn^i is the number of grains of species 'i' with radii between 'a' and 'a+da', and n_H is the density of hydrogen nuclei and Mathis et al. (1977) estimated the value of a_{min} = 0.005 μm and a_{max} = 0.25 μm. The extinction in terms of this size distribution is,

$$A_\lambda = \sum_i \int_{a_{min}}^{a_{max}} 1.086\ N_i(a_i)\ \pi\ a_i^2\ Q_e(a_i, \lambda)\ da_i \tag{1.13}$$

where $N_i(a_i)$ is the column density of grains of species 'i' with radius a_i.

1.4.4 The Dust to Gas Ratio

The gas and dust are well mixed in the ISM and a good correlation exists between them. Using *Copernicus* observations, Bohlin et al. (1978) found that the mean ratio of total hydrogen column density to reddening is, N(H)/E(B – V) = 5.8 × 10^{21} H $cm^{-2}mag^{-1}$. Hence the reddening per H in the MW dust in diffuse cloud is E(B – V)/N(H) = 1.7× 10^{-22} cm^2 mag/H. Similarly, the reddening per H atom for the LMC is 4.5 × 10^{-23} mag cm^2/H (Koornneef 1982) and for the SMC is 2.2×10^{-23} mag cm^2/H (Martin et al. 1989). It is well known that the extinction at wavelength λ is A_λ= 1.086 τ and the optical depth τ is given by

$$\tau_\lambda = \int n_d\ \sigma_e\ dl = \int (\rho_{dust}/m_{dust})\ \sigma_e\ dl = \int n_H\ (\rho_{dust}/\rho_{gas})\ (m_{gas}/m_{dust})\ \sigma_e\ dl \tag{1.14}$$

where ρ_{dust}/ρ_{gas} **= the dust to gas ratio**, n_{dust} is number of dust grains per unit volume, m_{dust} is the mass of a dust grain, and m_{gas} the mean gas particle mass per H nucleon $\sim 1.4m_H$. Extracting the mean values from the integral

$$\tau_\lambda = \langle\rho_{dust}/\rho_{gas}\rangle\langle m_{gas}/m_{dust}\rangle\ Q_e\ \pi\ a^2\ N_H \tag{1.15}$$

$$A_v = 1.086\ N_H\langle\rho_{dust}/\rho_{gas}\rangle\frac{3m_{gas}Q_e}{4\rho_{gr}a} \tag{1.16}$$

where grain specific density is ρ_{sd} and $m_{dust} = 4/3\pi a^3\rho_{sd}$. With $R_V = A_V/E(B\text{-}V)$, $A_V \approx N(H)/1.8\times10^{21}$ mag cm^{-2} H as $R_V = 3.1$ and $m_{gas} \sim 1.4m_H$,

$$\langle\rho_{dust}/\rho_{gas}\rangle = \frac{4\rho_{sd}a}{3\times1.8\times10^{21}\times1.86\times Q_e\times3\times1.4m_H} \tag{1.17}$$

If we assume visual extinction due to grains of 1000 Å $(2\pi a \approx \lambda)$ with typical value of grain specific density ρ_{gr} = 2.5 gm cm^{-3} and $Q_e \approx 1$, then dust to gas ratio is,

$$\langle\rho_{dust}/\rho_{gas}\rangle \approx 0.01 \tag{1.18}$$

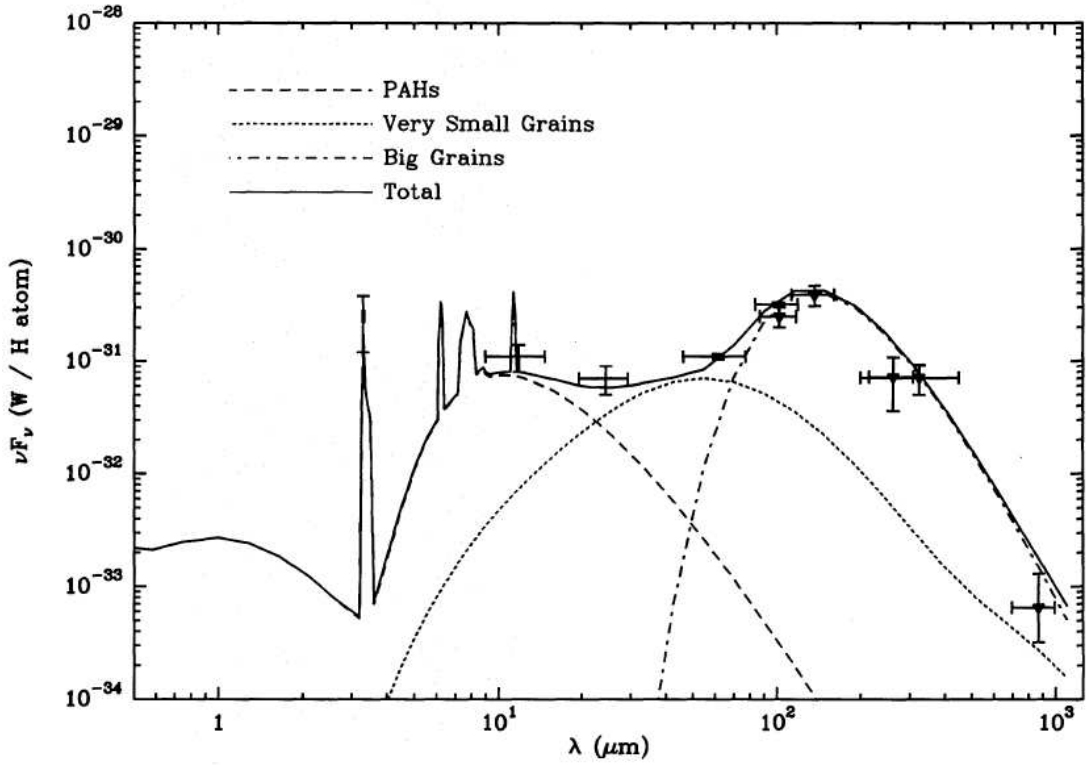

FIGURE 1.2: Dust emission spectrum of the diffuse ISM. The horizontal bars represent the filter width of the observations and the continuous line represents the model spectrum considering the PAHs, VSGs and BGs (Desert et al. 1990).

1.4.5 Dust Absorption and Emission

The light coming from the distant star is either scattered from the line of sight or absorbed by the dust grain. The absorbed photon increases the internal energy of the dust grain and heat the grain upto a temperature of 20 – 80 K and then re-emitted in IR. So, the most suitable wavelength to study the dust properties is IR. Space based IR observatories such as the *Infrared Astronomy Satellite (IRAS)*, the *Diffuse Infrared Background Experiment (DIRBE)* instrument on the *Cosmic-microwave Background Explorer (COBE)*, the *Infrared Space Observatory (ISO)*, the *Spitzer Space Telescope*, the *Herschel* and the *Planck* have provided ample of data from near IR to far IR (2 to 140 micron) of the diffuse emission from the dust grain in the whole sky. Figure 1.2 (Desert et al. 1990) shows the IR emission from dust grains of different size. Schlegel et al. (1998) have constructed an all sky map of the Galactic dust based upon the observations made with *IRAS* and *COBE* (Figure 1.3). The map can be used to derive extinction and dust temperature.

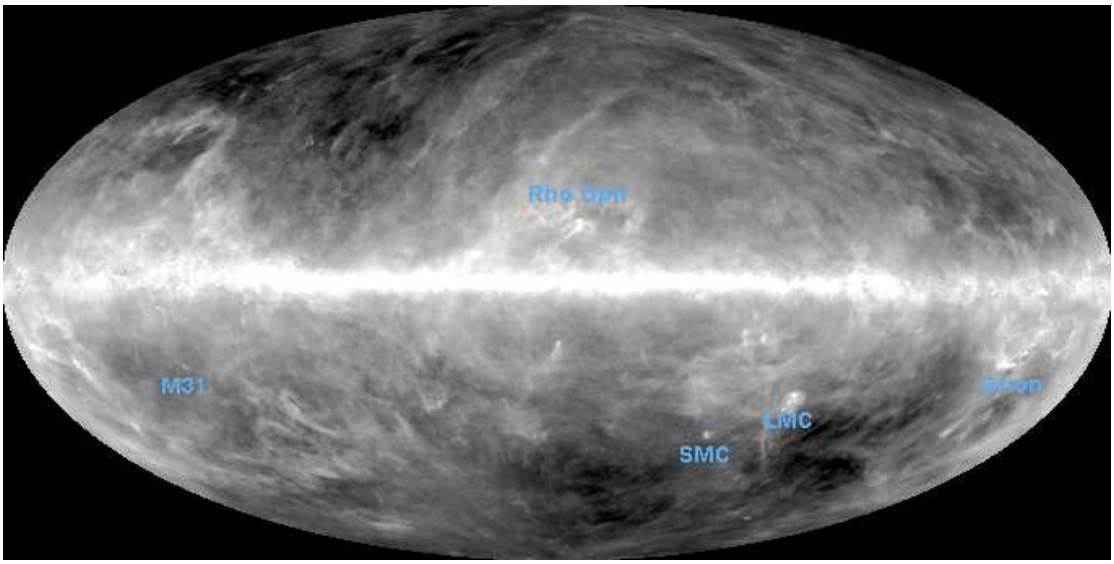

FIGURE 1.3: All sky map of the Galactic dust (Schlegel et al. 1998).

The dust grains show intense IR emission bands at 3.3, 6.2, 7.7, 8.6, and 11.3 μm and are designated as unidentified infrared bands (UIBs). These emission features are observed in spectra of bright reflection nebulae, planetary nebulae, and H II regions. The carriers of these UIBs are very small grains (VSGs) or big molecules such as PAHs (Tielens et al. 1984; Leger & Puget 1984; Draine & Li 2001). Big grains (BGs) with sizes more than 0.01 μm are responsible for the extinction in visible and IR, and the emission from them is observed at wavelengths longwards of 60 μm.

1.4.6 Temperature of Dust Grain

Interstellar dust grains gets heated by absorbing UV and visible radiation from the interstellar radiation field (ISRF) and cooled by re-emitting in IR. If 'a' is the radius of a spherical grain, the power absorbed from the ISRF is

$$E_{abs} = \int_0^\infty Q_a(\nu) J_\nu d\nu \tag{1.19}$$

where J_ν is the mean intensity over all direction and Q_a is the absorption efficiency factor. The power emitted by grains is

$$E_{em} = \int_0^\infty Q_{em}(\nu) B_\nu(T) d\nu \tag{1.20}$$

Where $B_\nu(T)$ is the Planck's function,

$$B_\nu(T) = \frac{2h}{c^2} \frac{\nu^3}{exp(h\nu/kT) - 1} \tag{1.21}$$

If a dust grain is at thermal equilibrium at a temperature T_d, then

$$\int_0^\infty Q_a(\nu) J_\nu d\nu = \int_0^\infty Q_{em}(\nu) B_\nu(T_d) d\nu \tag{1.22}$$

From the Kirchhoff's law, $Q_{em} \simeq Q_a$. To deduce the temperature of the dust from the above equation, one has to determine Q_a that depends on the frequency for a given radius 'a' of the dust. According to the small particle approximation of Mie theory, Q_a is given by

$$Q_a = \frac{8\pi a}{\lambda} Im\left(\frac{m^2 - 1}{m^2 + 2}\right) = aQ_0\nu^\beta \tag{1.23}$$

The value of β is determined theoretically (Tielens & Allamandola 1987) which is 2 for metals and crystalline dielectric substance, and 1 for an amorphous layer lattice. Using $B_\nu(T_d)$ and Q_a in equation (1.22),

$$\int_0^\infty Q_a(\nu) B_\nu(T_d) d\nu = aQ_0 \frac{2h}{c^2} \int_0^\infty \nu^\beta \frac{\nu^3}{exp(h\nu/kT) - 1} d\nu \tag{1.24}$$

$$= aQ_0 \frac{2h}{c^2} \left(\frac{kT}{h}\right)^{4+\beta} \int_0^\infty \frac{x^{3+\beta} dx}{e^x - 1} \tag{1.25}$$

A quick estimation gives, $Q_a \simeq 10^{-23}\ a\nu^2$ ('a' in cm and ν in Hz) which implies $Q_0 = 10^{-23}$ and the approximate value of integral in equation (1.25) for $\beta = 2$ is

$$\int_0^\infty \frac{x^{3+\beta} dx}{e^x - 1} = \int_0^\infty \frac{x^5 dx}{e^x - 1} = 122.08 \tag{1.26}$$

Hence the equation (1.22) becomes

$$\int_0^\infty Q_a(\nu) J_\nu d\nu = 1.47 \times 10^{-6} a T_d^6 \quad [cgs - units] \tag{1.27}$$

If a dust grain is at a distance 'r' from a star of radius 'R', temperature 'T' and luminosity 'L' then the mean intensity reaching the dust grain is

$$J_\nu = \frac{1}{4\pi} \int B_\nu(T_S) cos\theta d\Omega = \frac{1}{4\pi} B_\nu(T_S) \pi R^2 / r^2 = \frac{B_\nu(T_S) \pi R^2}{4\pi r^2} \tag{1.28}$$

where $B_\nu(T_S)$ is the intensity of the star towards the dust grain. The absorption by dust is mostly in UV and $Q_{UV} \simeq 1$. So,

$$\int_0^\infty Q_a(\nu) J_\nu d\nu = \int_0^\infty J_\nu d\nu = \int_0^\infty \frac{B_\nu(T_S) \pi R^2}{4\pi r^2} d\nu = \frac{\pi R^2}{4\pi r^2} \int_0^\infty B_\nu(T_S) d\nu \tag{1.29}$$

The integrated Planck function is defined by

$$\int_0^\infty B_\nu(T_S) d\nu = \frac{\sigma T^4}{\pi} \tag{1.30}$$

Now equation (1.22) becomes,

$$\frac{\pi R^2}{4\pi r^2} \frac{\sigma T^4}{\pi} = \frac{\pi R^2}{4\pi r^2} \frac{\sigma T^4}{\pi} = 1.47 \times 10^{-6} a T_d^6 \quad (cgs - units) \tag{1.31}$$

The luminosity of the star, $L = 4\pi\sigma R^2 T^4$. Finally, the grain temperature is

$$T_d \simeq 4.0 \times (\frac{L}{a})^{\frac{1}{6}} r^{-\frac{1}{3}} \tag{1.32}$$

The typical temperature of the dust grain in the ISM is 10-20 K.

1.4.7 Polarization

Polarization of starlight arises when the light passes through the ISM containing aligned elongated interstellar grains and depends on the degree of alignment with the Galactic magnetic field. The light with electric vector parallel to the longer axis of the aligned dust grain is more extinguished than the vector parallel to the shorter axis and hence the polarization occurs. The wavelength dependence of polarization (P_λ) is given by an empirical formula termed as 'Serkowski's Law' (Serkowski et al. 1975):

$$P_\lambda = P_{max}\ exp\left\{-K\left(ln\left(\frac{\lambda_{max}}{\lambda}\right)\right)^2\right\} \tag{1.33}$$

where λ_{max} ($\approx 0.55\ \mu$m) is the wavelength of the maximum polarizarion $P_{\lambda_{max}}$. λ_{max} value is typically in the range of $0.34 - 1\mu$m with an average value of 0.55μm (Sellgren et al. 1985) but varies for different lines of sight. The quantity, K determines the width of the peak in the curve which was originally taken to be 1.15, but an improved fit (Wilking et al. 1982) gave the value of K = -0.10 + $1.86\lambda_{max}$. It is obvious from the Serkowski's law that the polarization increases with wavelength from near UV and reaches maximum in the optical and then falls in the IR showing a little resemblance to the extinction law. In the IR wavelength range this variation can be further approximated as $P_\lambda \propto \lambda^{-1.8}$ (Martin & Whittet 1990a) with clear resemblance to extinction. Polarization is neither associated with the bump (2175 Å) nor FUV rise of extinction curve implying that small grains are insufficient polarizers (may be spherical or less aligned)(Kim & Martin 1995). Polarization originates from the extinction of the light even though it shows imperfect correlation with extinction. Strong polarization is seen in visible range and its efficiency, $P_{max}/\ A_{\lambda_{max}} \leq 0.03$ and this is the theoretical upper limit on the polarization efficiency.

Apart from absorption, polarization is also observed inside molecular clouds in emission at FIR. In emission, the polarization is largest in the direction of largest absorption which is contrary to the optical polarization. Hildebrand et al. (1999) have discussed the dependence of FIR polarization on optical depth and wavelength in dense cloud cores and envelopes. Even though the grain alignments

are difficult in dense clouds as the dust grains are far from equilibrium with the surrounding, the polarization is due to spinning of the grains due to anisotropic starlight (Draine & Weingartner 1997).

1.4.8 Dust Scattering

Interstellar dust grains scatter electromagnetic radiation (both in ultraviolet and visible) and the scattering efficiency depends on shapes, sizes, compositions and distributions of the dust grains. Determination of intensity of the scattered radiation requires knowledge of relative location of stars and grains. If the scattering geometry is known, one can calculate the amount of radiation scattered in any direction. However, the geometry is so complicated that optical parameters like albedo and asymmetry parameter are used to delineate the scattering properties of dust.

- **Albedo (α)** measures the fraction of the extincted light due to scattering, $\alpha = Q_c/Q_e$. Its value ranges from 0 (pure absorbers) to 1 (pure dielectric) depending on the material of the dust and the observed wavelength.

- **Asymmetry parameter (g)** specifies the degree of scattering in a direction and is defined as the mean value of the cosine of scattering angle weighted with respect to scattering function.

$$g(\theta) = \langle cos\theta \rangle = \frac{\int_0^\pi S(\theta) sin\theta cos\theta d\theta}{\int_0^\pi S(\theta) sin\theta d\theta} = \frac{2\pi}{\sigma_{sca}} \int_0^\pi S(\theta) sin\theta cos\theta d\theta \qquad (1.34)$$

  Its value varies from -1 (completely backward scattering) to 1 (completely forward scattering). Positive value of 'g' signifies scattering more towards the forward direction and negative value means more toward the backward direction where as g = 0 means scattering of light is isotropic.

- **Scattering function S(θ)** describes the angular distribution of scattered light and it is related to scattering cross section (σ_{sca}) of dust grain by

$$\sigma_{sca} = 2\pi \int_0^{\pi} S(\theta) sin\theta d\theta \tag{1.35}$$

An analytic and computationally convenient Henyey-Greenstein phase function (Henyey & Greenstein 1942) is used to measure the scattering radiation, particularly in anisotropic multiple scattering approximations:

$$\phi_0(\theta) = \frac{1}{4\pi} \frac{1 - g^2}{(1 + g^2 - 2gcos\theta)^{3/2}} \tag{1.36}$$

Scattering of light by dust grains is most efficient when the wavelength of light is same as the size of the grains. Three main observational evidence of scattering of light in the ISM are;

1. **Diffuse Galactic light (DGL)** – The scattering of ISRF by diffuse interstellar dust grain constitutes diffuse Galactic light (DGL) which is strong near the Galactic plane. The DGL is difficult to observe and analyze because of its faintness and numerous sources of contamination. Its observation requires careful correction for the contribution of faint stars, airglow and zodiacal light. The DGL is seen from the optical into the UV and its modeling requires knowledge of the spectral dependence of the illuminating source over the entire UV-optical wavelength range. The observed scattering properties of interstellar dust are compared with the dust models to determine grain properties such as albedo and scattering phase function.

2. **Reflection nebulae** – In reflection nebulae, light is scattered by a bright star and is very conspicuous at optical and UV wavelengths when dust is illuminated by the star. Study of scattering properties of dust in reflection nebula is easier than the DGL as the spectral properties of the illuminating star is better known than the ISRF. But reflection nebula suffers some disadvantages due to i) Unknown geometry of star and less known properties of dust. ii) Patchiness of dust is a problem as determination of albedo and scattering function is not easy for such distribution iii) The interpretation of

scattering angle is also a problem due to uncertain position of the star (star may be in front, back or embedded).

3. **Dust clouds** – The dust clouds that are not close to a star are illuminated by ISRF. The geometry of high Galactic dark clouds is better known than a reflection nebula, for e.g., in optical wavelength band, the dark clouds brightened by forward scattering grains where the illuminating source is behind the cloud (FitzGerald et al. 1976). A lot of observations and modelings of UV scattering by clouds at different latitude are done and few of them are; observations of Cirrus cloud by Haikala et al. (1995), *FUSE* and *Voyager* observations of Ophiuchus by Sujatha et al. (2005) and Coalsack by Sujatha et al. (2007) and *SPEAR/FIMS* observations of the Taurus molecular cloud by (Lee et al. 2006).

1.5 Heating Mechanisms in the ISM

There are several sources of energy for the interstellar gas viz., stars, X-rays, cosmic-rays and transient events such as stellar wind, novae and super novae. The ISM is heated by these energy sources which is then balanced by various cooling processes giving rise to a thermal balance between them even though thermodynamic equilibrium is rarely met in the ISM. In general, heating and cooling of the ISM means the transfer of kinetic energy (KE) to and from atoms, molecules and ions of interstellar gas. The heating process starts with photo-ionization where an electron is removed from an interstellar species by an energetic photon. This electron share its KE with other atoms, molecules and ions and heats the medium by thermalization through elastic collision. Various heating mechanism of the ISM are as follows:

1.5.1 Photoionization

Photoionization is the process of interaction of electromagnetic radiation with atomic targets which results either removal or excitation of the electrons of the atom. An energetic UV photon of frequency ν falls on an atom of ionization potential 'I', yielding an electron 'e' with energy *(hν-I) i.e.*,

$$A + h\nu \rightarrow A^{+} + e + (h\nu - I) \tag{1.37}$$

This energy (hν-I) is carried by the electron which in turn heats up the gas by colliding with atoms and ambient electrons of the ISM. In H II regions, photoionization is a major heating process where ionization of H is dominant. Photons with energy less than 13.6 eV also heats the gas by photoionization of heavy atoms, C, Si, Fe and molecules.

1.5.2 Cosmic Rays

Cosmic rays (CRs) are quite efficient in heating the ISM. CRs can penetrate deep into the molecular clouds and neutral ISM producing high temperatures. They transfer energy to gas by ionization and excitation thus by producing free electrons through Coulomb interactions. Low-energy CRs (E < 50 MeV) are more important pertaining to heating mechanism because they are far more numerous than high-energy CRs. The total ionization by CRs, $\xi_{\rm CR}$, including secondary ionizations of H and He is given by

$$n\xi_{\rm CR} = n\xi_{\rm CR}[1 + \phi^{H}(E, x_e) + \phi^{He}(E, x_e)], \tag{1.38}$$

Where the factors ϕ^{H}(E, x_e) and ϕ^{He}(E, x_e) give the number of secondary ionizations of H and He produced per primary ionization (depends on electron energy)

and x_e (n_e/n) is the electron fraction (Wolfire et al. 1995). With a primary ionization rate of 2×10^{-10} s^{-1}, the total ionization rate of CRs is $\xi_{CR} \simeq 3\times10^{-10}$ s^{-1}. The heating rate is given by

$$n\Gamma_{CR} = n\xi_{CR}E_h(E, x_e), \tag{1.39}$$

E_h(E,x_e) is the average heat deposited per primary ionization. For low degrees of ionization, E_h(E,x_e) $\simeq$ 7eV. Then the cosmic-ray heating rate is

$$n\Gamma_{CR} = 3 \times 10^{-10} n \left[\frac{\xi_{CR}}{2 \times 10^{-10}}\right] \quad erg/cm^3/s \tag{1.40}$$

1.5.3 X-Rays

X-ray emission in ISM is produced mainly from the hot gas and is efficient in heating warm, less dense atomic medium (Werner et al. 1970). X-rays remove electrons from atoms and ions which can cause excitations or further ionizations liberating other electrons like cosmic rays,

$$e + H(1s) \rightarrow e + H(2p) \rightarrow e + H(1s) + h\nu \tag{1.41}$$

or

$$e + H(1s) \rightarrow e + H^+ + e \tag{1.42}$$

The electrons liberated will go on ionizing the ISM until its energy is reduced to less than 13.6 eV and there will be no excitation of H atoms when the energy is less than 10.2 eV. The primary ionization rate of species 'i' due to soft X-ray is given by

$$n\xi^i_{XR} = 4\pi n \int \frac{J_\nu}{h\nu} e^{-\sigma_\nu N_H} \sigma^i_\nu d\nu \tag{1.43}$$

where the factor, $e^{-\sigma_\nu N_H}$ is an absorbing layer of warm material of column density N, $\frac{J_\nu}{h\nu}$ is X-ray mean photon intensity, σ_ν is X-ray photoionization cross-section

and σ_ν^i is that of the element 'i' (Wolfire et al. 1995). The heating rate is given by

$$n\Gamma_{\rm XR} = 4\pi n \sum_i \int \frac{J_\nu}{h\nu} e^{-\sigma_\nu N_H} \sigma_\nu^i E_h(E^i, x_e) d\nu \quad cm^{-3}s^{-1} \quad erg/cm^3/s \qquad (1.44)$$

where the summation extends over species which suffer primary ionization and other symbols have usual meaning. Unlike cosmic rays, the X-ray ionization rate and heating rate decreases with increasing depth of a cloud because of attenuation.

1.5.4 Heating by Photodissociation of Molecules

Photodissociation of H_2 starts with absorption of FUV photon from ground electronic state to an excited electronic state followed by a radiative decay into the vibrational continuum of the ground state in which nearly 10% of the molecule dissociates. This radiative decay of the molecule gives rise to an emission of IR photons or the molecule is de-excited through collisions if the density is high (n $\geq$ 10^4), thereby heating the gas. The heating by this process is given by

$$n\Gamma_{\rm pd} = 4 \times 10^{-14} n(H_2) k_{\rm pump} \quad erg/cm^3/s \qquad (1.45)$$

The pump rate of molecular hydrogen is given by

$$k_{\rm pump} = 3.4 \times 10^{-10} \beta(\tau) G_0 e^{(-2.6A_v)} \quad s^{-1}, \qquad (1.46)$$

where $k_{\rm pump}$ is the pumping rate of UV photons that depends on $\beta(\tau)$, the reduction of the FUV pumping radiation due to self-shielding (optical depth τ) by H_2 and the exponential factor takes care of the dust absorption. G_0 is the average interstellar field (the Habing's field). The heating efficiency of this process is given by

$$\epsilon(H_2) \simeq \left(\frac{E_{vib}}{h\nu}\right) f_{H_2} \simeq 0.17 f_{H_2}, \qquad (1.47)$$

where E_{vib} is the vibrational energy converted into heat, hν is the energy of the pumping FUV photon and f_{H_2} is the fraction of the FUV photon pumping H_2.

1.5.5 Chemical Heating

Molecular hydrogen (H_2) is formed on the surface of dust grains when two H atoms meet. This process is exothermic yielding an energy of 4.48 eV. A part of this energy (4.2 eV) lifts the molecule to a rotational and vibrational excited state and rest is converted into kinetic energy (0.2 eV) of the H_2 molecule. This kinetic energy as well as the energy released from de-excitation of the H_2 by inelastic collisions with other atoms and molecules heats the gas. The heating rate is given by

$$\Gamma_{H_2} = R_f n^2 x_H (0.2 + 4.2\eta) \quad eV/cm^3, \tag{1.48}$$

where R_f is the formation rate of H_2 on grain surface, η is the fraction of the excitation energy of H_2 that is used for heating and x_H is the fraction of gas particle that are H atoms. Chemical heating is an efficient process in shocks and dense photodissociation regions.

1.5.6 Photo-electric Heating

Small dust grains and large molecules such as PAH are efficient in photoelectric heating which is an important mechanism in cold diffuse ISM. The UV radiation emitted by hot stars can remove electrons from dust grains. A part of the photon energy is used in removing the electron from dust grain and the remainder of the photon's energy heats the grain providing KE to the ejected electron that in turn heats the gas. According to Mathis et al. (1977), size distribution of dust grains $n(a) \propto a^{-3.5}$, and hence, the area distribution is, $a^2 \times n(a) \propto a^{-1.5}$ (a is the grain radius). This shows that the smallest dust grains dominate photo-electric heating. The photoelectric heating rate as derived by Bakes & Tielens (1994) is:

$$\Gamma_{pe} = 10^{-24} \epsilon G_0 n_H \quad erg/cm^3/s, \tag{1.49}$$

where ϵ is fraction of the energy absorbed by grains that heats the gas,

$$\epsilon = \frac{3 \times 10^{-2}}{1 + 4.2 \times 10^{-4} G_0 T^{0.5}/n_e} \tag{1.50}$$

and G_0 is the FUV flux normalized to Habing value (1.6×10^{-3} erg/s/cm^2) (Habing 1968).

1.5.7 Grain-Gas Heating

At relatively high densities, the collision of gas atoms and molecules with dust grains leads to exchange of energy between them. The gas atoms colliding with the dust grains can gain heat if the dust is warmer than the gas. This is an important heating process in giant molecular clouds where the grains are heated by the FIR radiations coming from outside. This radiation can penetrate deep inside the cloud heating the gas that is at a lower temperature than the dust grain (Falgarone & Puget 1985). The heating rate is given by

$$n\Gamma_{g,d} = n_H n_d \sigma_d \left(\frac{8kT}{\pi m}\right)^{1/2} 2k\alpha(T_d - T) \quad erg/s/cm^3, \tag{1.51}$$

where n_d is number density, $\sigma_d =< \pi a^2 >$ is geometrical cross section, T_d is the temperature of dust grain and T is the gas temperature ($T_d > T$). $\alpha = \frac{T_2 - T}{T_d - T}$ is the accommodation coefficient, measures how well the gas atom accommodates to the grain. T_2 corresponds to an intermediate temperature between T_d and T. In ISM, $\sigma_d n_d = 1.5 \times 10^{-21} n_H$ cm^{-1} and $\alpha = 0.35$ (Burke & Hollenbach 1983). The heating rate is given by

$$n\Gamma_{gd} \simeq 10^{-33} n_H^2 T^{1/2}(T_d - T) \quad erg/s/cm^3, \tag{1.52}$$

1.5.8 Heating by Macroscopic Processes

Apart from the microscopic processes, there are several macroscopic processes such as gravitational collapse of a cloud, Supernova explosions, stellar winds, expansion of H II regions, Magneto-hydrodynamic waves created by supernova remnants play major role in heating the gas although these processes are not delineated explicitly. Gravitational collapse occurs during star formation as well as during the death of

a star. In this process, the material of a massive body is pulled inwards by its own gravity generating a huge amount of energy which is dissipated as heat, thus heating the gas of the ISM. Massive cataclysmic events like supernova explosion and stellar winds pour a huge amount of mechanical energy into the ISM that goes on heating the gas. Expansion of H II regions by champagne effect and collisionless damping of interstellar magneto-hydrodynamic waves also heat up the gas upto some extent.

1.6 Cooling Mechanisms in the ISM

Interstellar gases cool by emitting radiation. An atom, molecule or ion gets excited gaining KE through collision with an energetic particle (electron, H, H^+ etc.) and gets excited. This excited specie undergoes radiative decay giving away its energy as a photon which may escape the cloud thus by cooling the gas. Basically the collisionally excited lines of metal play a critical role in the cooling mechanism. The cooling process to be efficient there should be abundance of species to make the collisions frequent and the gas should be optically thin, so that photons emitted won't be re-absorbed. This cooling process is efficient everywhere in the ISM besides hot gas and regions deep within the molecular clouds. The cooling process is given by

$$X + Y \rightarrow X + Y^{\star} \quad and \quad Y^{\star} \rightarrow Y + h\nu \tag{1.53}$$

This hν amount of energy escapes out of the system and cools the gas. Various cooling mechanism are described below.

1.6.1 Molecular Cooling

In molecular clouds, where temperature is less than few hundred Kelvin, the gas is cooled by IR rotational lines. A molecule is excited by rotational or vibrational transition and then returns to a lower energy state, emitting a photon which can leave the region and cool the cloud. The molecules which contribute to the

cooling are CO, CH, OH and H_2O by their electric dipole transition and H_2 by its quadrupole transition (Goldsmith & Langer 1978). The quadrupole transition of H_2 molecule occurs via ΔJ=$\pm$2 transitions, the life time of which is very long (3 $\times$ 10^{10} sec). So, the population of this level, N_J increases, where

$$N_J \propto (2J+1)e^{(-E_J/kT)}, \tag{1.54}$$

Hence, radiation sheds out of this level slowly that is very unlikely to be re-absorbed by H_2. The cooling rate by H_2 is given by

$$\Lambda_{H_2} = \sum_{J\geq 2} n(H_2, J)\Delta E(J \rightarrow J-2)A(J \rightarrow J-2) \tag{1.55}$$

where the discrete value of energy $E_J = BJ(J+1)$, J=0,1,2... CO molecule is an important coolant in denser clouds even though its abundance is low, $\approx$ $10^{-5} \times N(H_2)$. The cooling rate of CO which possesses a dipole moment transition (ΔJ=$\pm$1) is given by

$$\Lambda_{CO} = \sum_{J} n(CO, J)\Delta E(J \rightarrow J-1)A(J \rightarrow J-1) \quad erg/s/cm^3, \tag{1.56}$$

1.6.2 Cooling by Resonance and Metastable lines

At higher temperature (T > 800 K), collisional excitation of n=2 level (metastable level) of hydrogen will release a Lyα photon upon de-excitation which may escape from the region cooling the cloud. Metastable transitions of C I, C II, O I, O II, Si I, Si II, S I, S II, Fe I, and Fe II also contribute to the cooling (Wolfire et al. 1995). The cooling by Lyα is given by

$$n^2\Lambda(HI) = 7.3 \times 10^{-19} n_e n_{(HI)} e^{-118400/T} \quad erg/s/cm^3, \tag{1.57}$$

1.6.3 Cooling by Dust

Interstellar dust grains are cooler than the gas in neutral diffuse medium and acts as a coolant at high density (n $\geq 10^8$ cm^{-3}) shocks. The cooling rate per unit volume is given by

$$\Lambda_{gr} = 1.2 \times 10^{-31} n^2 \left(\frac{T}{1000K}\right)^{1/2} \left(\frac{100\mathring{A}}{a_{min}}\right)^{1/2} \times [1 - 0.8e(-75/T)](T - T_{gr}) \quad erg/s/cm^3, \tag{1.58}$$

where T_{gr} is the grain temperature, T is the gas temperature and a_{min} is the minimum radius of the grain.

1.6.4 Fine Structure Line Cooling

[C II] has a transition ($^2P_{1/2} \rightarrow {}^2P_{3/2}$) at 158 μm with an energy corresponding to 92 K. This is one of the important coolant of the gas clouds at low temperature. The cooling rate per unit volume for C^+ is

$$\Lambda_{e,CII} = 1.23 \times 10^{-27} n_H^2 d_C e^{-92K/T} (T/100)^{1/2} \quad erg/s/cm^3 \tag{1.59}$$

The quantity d_c is the depletion of carbon. C II can also be excited by collisions with hydrogen atoms (Wolfire et al. 1995) and this gives

$$\Lambda_{H,CII} = 7.9 \times 10^{-27} n_H^2 d_C e^{-92K/T} \quad erg/s/cm^3 \tag{1.60}$$

where it is assumed that C and H nuclei are in C II and H I atoms.

1.6.5 Recombination

The radiative recombination of an electron with a proton or ionized species in an ionized gas can cool the gas. The KE of the electron is removed from the thermal energy of the gas, the energy loss of which is given by

$$\Lambda_{reco} = n_e \; n_p \; k \; T_e \; \beta(T_e), \tag{1.61}$$

where n_e = electron density, n_p = proton density, T_e = electron temperature, and β = recombination coefficient.

1.6.6 Bremsstrahlung

A plasma of gas emits bremsstrahlung radiation due to interaction of free electrons with ions and this radiation escapes out of the plasma carrying a part of the internal energy thus by cooling the gas. The bremsstrahlung cooling rate integrated over frequency is given by

$$\Lambda_{brem} = 1.4 \times 10^{-27} Z^2 T^{1/2} n_e n_p g_B \quad erg/s/cm^3 \tag{1.62}$$

where g_B is the frequency averaged Gaunt factor and is of the order of unity and Z is charge on the ion.

Chapter 2

Diffuse Background Radiation in the Ultraviolet: Observations and Data Reduction

2.1 Diffuse UV Background

Diffuse celestial backgrounds occur at all measurable wavelengths from radio wave to gamma rays that carry a lot of information about the Universe. The origin of the background emissions is related with wide variety of sources starting from the local ISM to the farthest reach of the observable Universe. The diffuse background radiation at UV occurs in the wavelength range of 900 – 3200 Å. Over the past forty years, studies of the diffuse UV backgrounds either by observations or model calculations suggest that the possible sources of this could be Galactic and extragalactic. Although the extragalactic sources have already been identified, the amount of extragalactic light coming to our Galaxy is poorly constrained (Bowyer 1991).

The first observations of the diffuse UV radiation field were made by Hayakawa et al. (1969) and Lillie & Witt (1969) from sounding rocket experiments who claimed that diffuse UV light is due to star light scattered by dust. Subsequently, more observations were made to measure the intensity of the diffuse UV background to investigate its

connection to the origin of Universe and Galactic evolution. There are excellent reviews by Paresce & Jakobsen (1980); Bowyer (1991); Henry (1991); Murthy (2008) where they have discussed the present status of observations and theories of the diffuse UV background. Although several components contribute to the diffuse UV light, it is dominated by radiation from hot stars scattered by interstellar dust grains, called Cosmic UV background. A review by Leinert et al. (1998) on diffuse night sky brightness explains all the components of diffuse radiation field over a wide range of wavelengths from far UV to far IR in great detail.

2.2 Components of the Diffuse UV Radiation

- **Dark Counts:** Dark count is the instrumental background arising generally through fast particles hitting the detector. It is inherent with the instrument and difficult to remove. The typical count rate for low Earth orbit is of the order of 5 counts cm^{-2} s^{-1}. The count rate corresponding to this will depend on the calibration and the field of view.

- **Airglow:** Airglow arises in the Earth's atmosphere which is a strong function of time of observation and height as it varies with changes in atmosphere and solar activity (Meier 1991). It is produced by the collision of charged particles from space, mainly from the Sun, with atoms and molecules in the upper atmosphere. Airglow lines are the most deceptive sources that come into play while measuring the diffuse UV radiation from satellites above the atmosphere. There are 20 major airglow lines found above the earth's atmosphere and the brightest among them are the Lyman series lines(Lyα, Lyβ, Lyγ) seen upto the Lyman limit at 912 Å where solar radiation is resonantly scattered by interplanetary hydrogen atoms in the upper atmosphere at altitudes of greater than 1000 km. Other airglow lines are less significant at night at 600 km or higher.

- **Zodiacal light:** Zodiacal light results from solar light scattered by interplanetary dust grains. It mainly dominates in visible and IR, and less significant in the UV, even its contribution to diffuse UV background drops to zero below 2000 Å. It is generally assumed that the colour of zodiacal light is similar to solar color with moderate amount of reddening with respect to the Sun. Distribution of the zodiacal light in the UV follows that in the visible.

- **Unresolved stars:** Unresolved stars influence the results of diffuse UV background as they come into the field of view of the instrument attempting to measure the same. This problem may be solved by reducing the field of view of the instrument and restricting the observations to high galactic latitudes where number of hot stars are less and far apart. For fainter stars, theoretical stellar emission models and luminosity functions may be used with suitable stellar catalog to eradicate the stellar contribution from the background measurements.

- **Extragalactic light:** In early 80s, it has been predicted that a measureble amount of extragalactic diffuse background exists at all wavelengths with little observational evidence. Expected sources of extragalactic background light in UV are thought to be mainly from redshifted star light from unresolved galaxies, integrated light from galaxies and QSOs, radiative decay of massive particles, collisional excitation in dense IGM etc. and all these processes are delineated vividly in reviews by Paresce & Jakobsen (1980); Paresce (1990). With the advent of UV detectors with better sensitivity and resolution it has been proved that majority of the UV background sources are within the Galaxy and a very small amount being extragalactic, the possible upper limit of which is about 50 to 300 Photons cm^{-2} s^{-1} sr^{-1} $Å^{-1}$ (Leinert et al. 1998).

2.3 Cosmic UV Background

Cosmic UV background is the component which originates beyond the solar system and is mainly due to the scattering of star light by interstellar dust grains. Intensity of this background depends on the distribution of hot stars, amount and distribution of dust, optical depth, and the optical parameters of dust; albedo and phase function. Other components of the cosmic background include atomic and molecular emission lines from O VI (Shelton et al. 2007; Welsh et al. 2007; Dixon et al. 2001), C IV (Welsh et al. 2007), and molecular hydrogen (Martin et al. 1990b; Duley & Williams 1980). Based upon observations made by *FUSE* (Murthy & Sahnow 2004) and *Voyager* (Murthy et al. 1999), the diffuse radiation field over many different locations of the sky has been mapped and it is argued that the diffuse FUV sky is patchy with regions of intense emissions near bright stars (Figure 2.1).

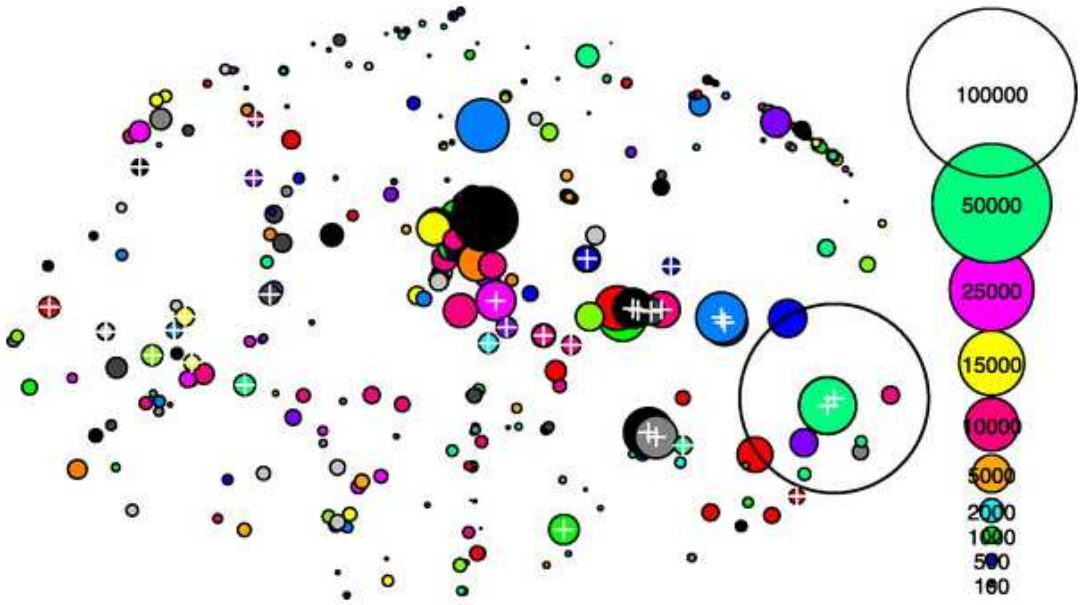

FIGURE 2.1: Combination of the Voyager observations of Murthy et al. (1999) and the FUSE observations of Murthy & Sahnow (2004) into an Aitoff projection of the diffuse FUV background with the Galactic center at the center of the image and ±180 at the left and right edges, respectively. The area of each circle is proportional to the observed surface brightness with the large open circle at the bottom right having a brightness of 2.9 × 10^5 photons cm^2 sr^{-1} s^{-1} $Å^{-1}$.

The background emission in UV and IR are important tracers of interstellar dust grains as the scattering by dust in UV is complementary to that of the emission in IR. The connection between the two wavelength bands can give good estimation of the dust parameters. However, the value of the albedo and scattering phase function that determines the scattering properties of dust spans over a wide range of values when estimated from the model calculations. Several works have attempted to study the relation of diffuse UV with IR wavelength as well as the line of sight neutral hydrogen column density for different celestial regions. Jakobsen et al. (1987); Perault et al. (1991); Haikala et al. (1995); Sasseen & Deharveng (1996); Schiminovich et al. (2001) have showed that a strong correlation exists between IR intensity at 100 μm as measured by IRAS and the diffuse background intensity in the FUV wavelengths. Haikala et al. (1995) using the *FAUST* data in FUV bands for a Galactic cirrus cloud, G251.2+73.3, near the north Galactic pole have demonstrated that scattered UV light is correlated with the IRAS 100 μm surface brightness and the authors have also modelled the scatter light to estimate the dust optical properties albedo (a=0.13±0.05 to 0.6±0.01) and scattering phase function (g=0.0 to 0.9). Schiminovich et al. (2001) using *NUVIEWS* instrument mapped the scattered UV light in four narrow UV bands which covers a one quarter of the sky

and found a good correlation of diffuse UV radiation with the IRAS 100 μm surface brightness and a moderate albedo (a=0.45±0.05) and highly forward scattering phase function parameter (g=0.77±0.1) over the same region. The existence of these properties thus provides strong observational support for the dust-scattered origin of most of the FUV background.

A series of investigations were carried out to find the relation of UV background with other Galactic parameters to provide an evidence to its origin. The most obvious parameter was the line of sight neutral hydrogen column density which showed a good correlation between the two at high and intermediate Galactic latitudes (Paresce & Jakobsen 1980; Maucherat-Joubert et al. 1980b; Joubert et al. 1983; Jakobsen et al. 1984; Onaka & Kodaira 1991; Hurwitz et al. 1991; Schiminovich et al. 2001) even though there is no such strict relation between them. Existence of this correlation gives evidence of Galactic component to the diffuse UV background due to scattering of starlight by high latitude interstellar dust mixed with neutral hydrogen. Besides the positive correlation, a positive offset of few hundred Photons cm^{-2} s^{-1} sr^{-1} $Å^{-1}$ is obtained which has been thought to be due to contaminations or extragalactic component to the diffuse UV background (Hurwitz et al. 1991). The correlation of diffuse UV background with Galactic latitude has also been tried (Weller 1983; Fix et al. 1989; Wright 1992; Sujatha et al. 2009, 2010; Murthy et al. 2010). Sujatha et al. (2009, 2010); Murthy et al. (2010) found that the diffuse UV background follows a cosecant law with Galactic latitudes.

The satellites which are now producing exciting results on the diffuse UV radiation field are Spectroscopy of Plasma Evolution from Astrophysical Radiation instruments (SPEAR, also known as Far Ultraviolet Imaging Spectrograph or FIMS) and Galexy Evolution Explorer (GALEX). The SPEAR/FIMS is a dual-channel FUV imaging spectrograph (S-band: 900-1150 Å and L-band: 1350-1750 Å) which covers 80% of the sky. GALEX has observed 75% of the sky in two ultraviolet bands (FUV: 1350-1750Å and NUV: 1750-2850 Å). A similar instrument to be launched by the Indian Space Research Organization (ISRO) in end of 2012 is the Ultraviolet Imaging Telescope (UVIT) which aims to observe the sky with a spatial resolution of 1.5 arcsecond in two UV channels (FUV: 1200-1800 Å and NUV: 1800-3000 Å). Lee et al. (2006) measured diffuse FUV continuum from the Taurus molecular cloud region with the SPEAR/FIMS imaging spectrograph and observed an anticorrelation of this with molecular hydrogen fluorescent which indicates that molecular hudrogen is not a major contributor of diffuse UV background. Similarly Seon et al. (2011) have presented far-ultraviolet (FUV: 1370-1720

Å) continuum background over most of the sky, obtained with the SPEAR/FIMS instrument finding a good correlation of diffuse FUV continuum intensity with N(HI), 100 μm, and Hα intensities. Recently, some studies on diffuse UV observations (Sujatha et al. 2009, 2010; Murthy et al. 2010) have done using data obtained with GALEX in both FUV and NUV bands. Sujatha et al. (2009, 2010) have identified dust scattered diffuse UV emissions for Draco and Sandage Nebulosity using Galex observations. Apart from airglow and zodiacal emissions, they found an additional amount due to line emissions from species such as CIV (1550 Å) and Si II (1533 Å) and H_2 fluorescent. Similar studies have made by Murthy et al. (2010) where they have mapped diffuse UV background which covers 75% of the sky except the Galactic plane and Magellanic Clouds. They found that diffuse UV surface brightness correlates strongly with IR 100 μm emission and follows cosecant law with Galactic latitude.

We used serendipitous observations made with the *FUSE* to report measurements of the diffuse FUV (1000 - 1150 Å) emission from the Magellanic Clouds (MCs). This section comprises of the description on the *FUSE* and *UIT* along with the data reduction technique to extract the diffuse FUV emission.

2.4 Far Ultraviolet Spectroscopic Explorer

The *FUSE* was launched in June, 1999 on a Delta II rocket into a nearly circular, low-Earth orbit with an inclination of 25° to the equator and reached its termination in October, 2007. The spacecraft and mission of *FUSE* have been described by Moos et al. (2000) and Sahnow et al. (2000). The *FUSE* data is archived at the Multimission Archive at the Space Telescope Science Institute (MAST). It was designed to observe sky in the FUV spectral range from 905 to 1187 Å upto a high resolving power of 20,000 ($\Delta\lambda/\lambda$). The primary purpose of *FUSE* was to explore the UV Universe with much greater sensitivity and resolving power which was not achieved by any other instrument then.

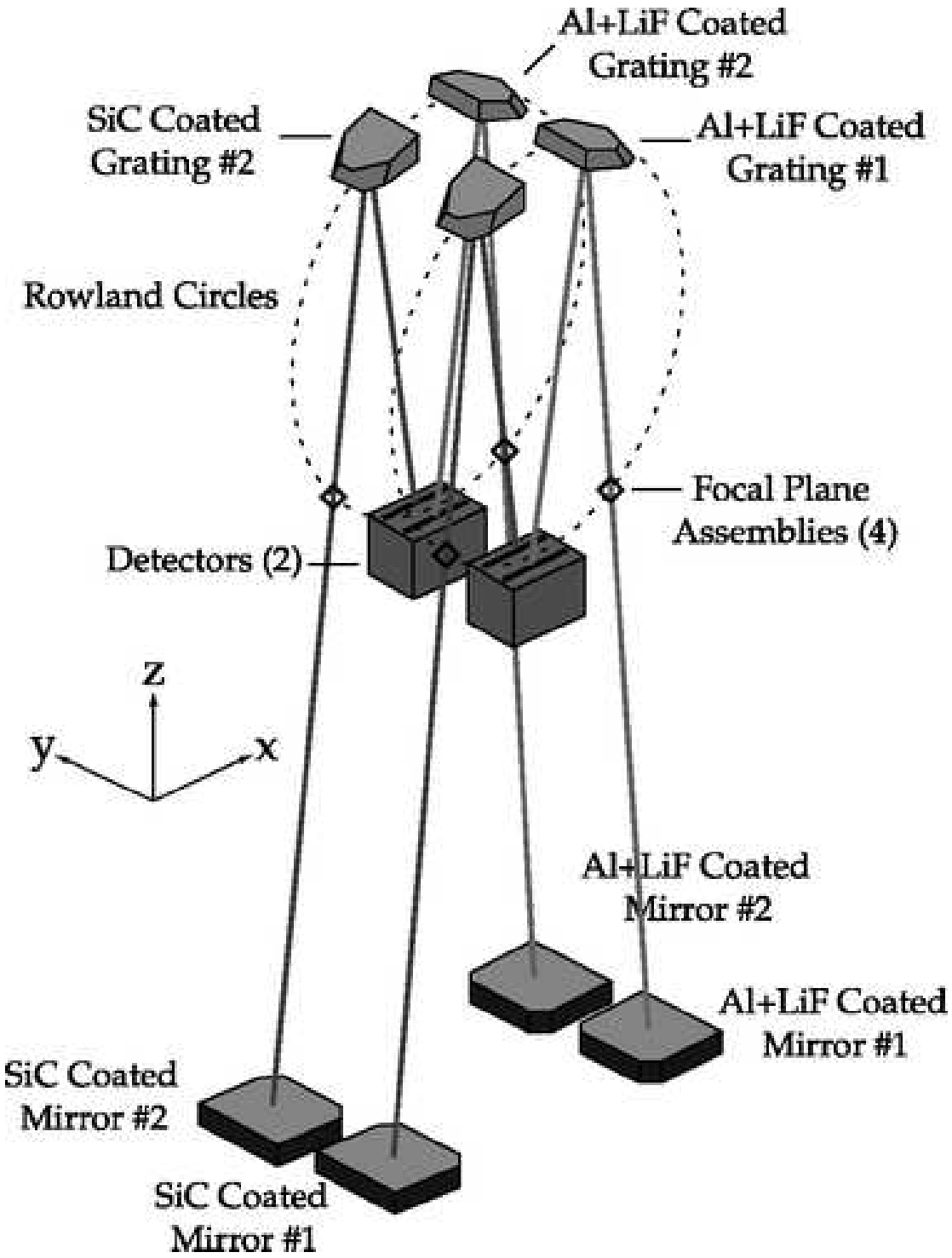

FIGURE 2.2: Optical design of the *FUSE* instrument showing the mirrors, focal plane assembly(FPA), gratings and detectors. The track of the light is from mirror to the rowland grating through the FPA and then reflects to the detector.

2.4.1 *FUSE* Instrument

The *FUSE* Instrument was fabricated in Rowland circle design. It consisted of four optical channels and each channel consisted of a mirror, a focal plane assembly (FPA), a diffraction grating and a portion of a detector. The four optical channels were co-aligned properly and provided with actuators on the FPA to obtain the maximum throughput. The two of the four mirrors and gratings were coated with silicon carbide (SiC) while the other two mirrors and gratings were coated with lithium fluoride (LiF) over aluminum (Figure 2.2). The four channels had two nearly identical sides of the instrument, where a side consisted of one LiF and one SiC channel. Each channel had a bandpass of about 200 Å , together covering the entire 290 Å wavelength range of the instrument (905 – 1187 Å). The spectra from the four channels were imaged onto two photon counting microchannel plate (MCP) detectors (labeled 1 and 2) and each detector had one SiC spectrum and one LiF spectrum imaged onto it. Each detector was divided into two functionally independent segments A and B; separated by a small gap. To ensure that the gaps do not fall at the same wavelength region in both detectors, they were offset slightly with respect to each other. Nearly the entire wavelength range was covered by more than one channel and the four channels overlapped 1015 – 1075 Å range, providing the highest effective area.

2.4.2 *FUSE* Apertures

At the prime focus of each mirror lies a FPA containing three spectrograph entrance apertures; the low-resolution aperture (LWRS; $30'' \times 30''$), used for most observations, the medium-resolution aperture (MDRS; $4'' \times 20''$) and the high-resolution aperture (HIRS; $1''.25 \times 20''$). Since these apertures were offset in the spatial direction, light passed by each of the apertures was imaged onto a different section of the detector.

The LWRS aperture was the most used or default aperture through out the missions because it avoided the thermal image motions that occurred on orbit and was intended to observe both the point sources and faint extended objects.

On-orbit thermal drifts of the channels with respect to the LiF guide channel resulted in limited use of the MDRS aperture due to the effort required to maintain alignment.

It was intended to observe mostly the point sources.

The HIRS aperture was designed to maintain the highest resolution at the expense of photometric accuracy. Its throughput was as high as 90% with minimum sky background. Because of the difficulties encountered with maintaining channel alignment on-orbit, this aperture was used sparingly during the mission.

The science data obtained from a detector for an exposure yielded four data files for each spectrum (LiF and SiC), labeled 1A, 1B, 2A, and 2B. All the three apertures of a channel were open to the sky at a time producing three spectra, one from each of the aperture.

2.4.3 Data Reduction Pipeline

The *FUSE* data is reduced by a data reduction software package, called CalFUSE. The entire *FUSE* data set available at MAST has been reprocessed with CalFUSE v3.2, the latest version of this software. The CalFUSE software takes care of the effect of spacecraft motion, the instrumental effects, thermal drift correction, geometric distortion correction, heliocentric velocity correction, dead time correction, wavelength calibration, background subtraction, astigmatism correction, and screens the data for low quality and unreliability. It is written in C programming language which consists of a series of modules called by a shell script and each module corrects an effect during its execution. The operation pipeline unified system (OPUS) is the data processing system used in CalFUSE to combine spectra from each channel and exposures into a set of observational level spectra. The data reduction and calibration process using CalFUSE v3.2 is described by Dixon et al. (2007).

2.4.4 *FUSE* Observations

The primary purpose of the *FUSE* mission was to take high resolution spectra ($\lambda/\Delta\lambda$ $\approx$ 20,000) of Galactic and extra-galactic sources. Although only the LWRS with its relatively large field of view was useful for diffuse observations, there were many fields

in which the primary aperture was either the HIRS or the MDRS leaving the LWRS aperture (separated from the other two apertures by 105″ and 210″, respectively) to observe a nominally blank region of the sky. We downloaded the data from the MAST archive at STScI and examined all for suitability for diffuse measurements. We rejected all point source observations within the LWRS using the Object Class from the *FUSE* archive. Then we were left with observations that were from two classes of targets: observations of point sources through either the MDRS or HIRS apertures; or calibrations where the apertures were pointed at nominally blank areas of the sky in order to allow the spectrographs to thermalize before an instrumental realignment. We processed all these observations using the latest version of the data pipeline software, CalFUSE v3.2 (Dixon et al. 2007). Murthy & Sahnow (2004) have described the analysis of these serendipitous background observations and we have followed their extraction of diffuse surface brightnesses from the *FUSE* spectra.

The *FUSE* data consists of observations of both the day and the night part of the orbit. Because of the faintness of the diffuse background, we have used only the night part of the observations, thereby reducing the effect of all the airglow lines other than the Lyman lines of atmospheric hydrogen. There are also additional lines like the weak O I lines around 1040 Å and N I lines at 1134 Å but these lines don't contribute significantly to the continuum emission. Although the diffuse signal is visible in all the apertures, we have used the data from LiF LWRS aperture because its throughput is much greater than the others.

In each of the observations the diffuse signal in the LiF LWRS aperture clearly stands out above the background. Still we found that the standard background subtraction by CalFuse overestimates the instrumental background for the faint extended sources. So, we have followed the procedure of Murthy & Sahnow (2004) to empirically estimate the instrumental background, which is the counts between the regions on either side of the aperture. We have set the limits to measure the diffuse flux and the instrumental background from the detectors.

Figure 2.3 is an image of detector segment 1A of a *FUSE* observation. The LiF apertures are imaged onto the top half and the SiC onto the bottom half of the image. Note that the LiF 1A wavelength scale is increasing to right while the SiC 1A scale is increasing to left. The enhancements due to the diffuse signal in the LiF LWRS aperture is clearly seen. In the procedure of measuring the diffuse flux, we have treated *FUSE* as a broad

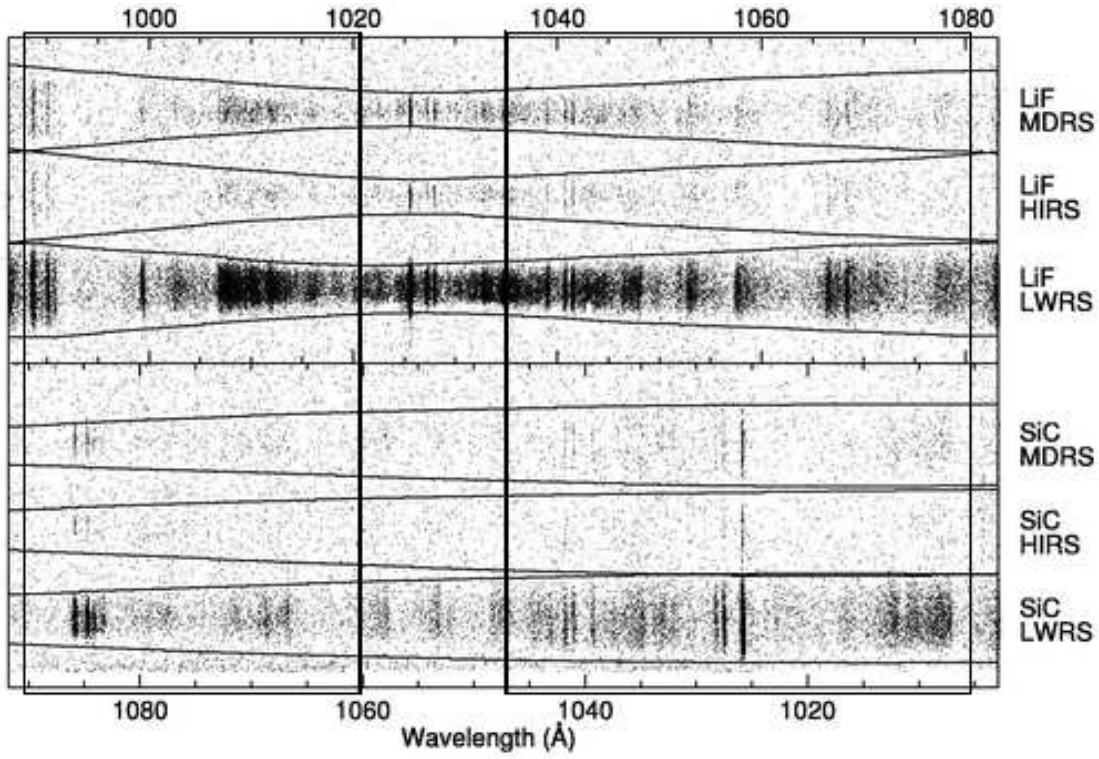

FIGURE 2.3: Image of the 1A detector segment of an observation. The LiF apertures are imaged onto the top half of the image and the SiC onto the bottom half with the terrestrial Lyβ line seen as the strongest line in each of the six apertures. Note that the defined bands (shown by the two large boxes) exclude the geocoronal Lyβ lines seen in the image (Murthy & Sahnow 2004).

band photometer and collapsed the spectra into two wavelength bands per detector, excluding the terrestrial airglow lines (primarily Lyβ, 1026 Å). The two boxes drawn across the image show the wavelength limits of of the two bands (1A1: 988 – 1021 Å and 1A2: 1035 – 1081 Å) on either side of the Lyβ line. The bands have been collapsed into corresponding effective wavelengths (1A1: $\lambda_{\rm eff}$ = 1003.93 Å and 1A2: $\lambda_{\rm eff}$ = 1058 Å) to measure the integrated flux in each band.

The signal in the LiF LWRS aperture is plotted in the Figure (2.4) and we have then fitted this profile with a Gaussian with uncertainties defined by the rms deviations adjacent to the aperture and found 90% confidence limits on the level of the diffuse background using the procedure of Lampton et al. (1976). The Gaussian was integrated out to measure the diffuse emission in the band and the background was derived from the strips off the spectrum and subtracted from the band flux. Similar procedure was followed for all other detector segments and this resulted in seven wavelength bands with effective wavelengths at 1004 Å (1A1), 1058 Å (1A2), 1117 Å (1B1), 1157 Å (1B2), 1159

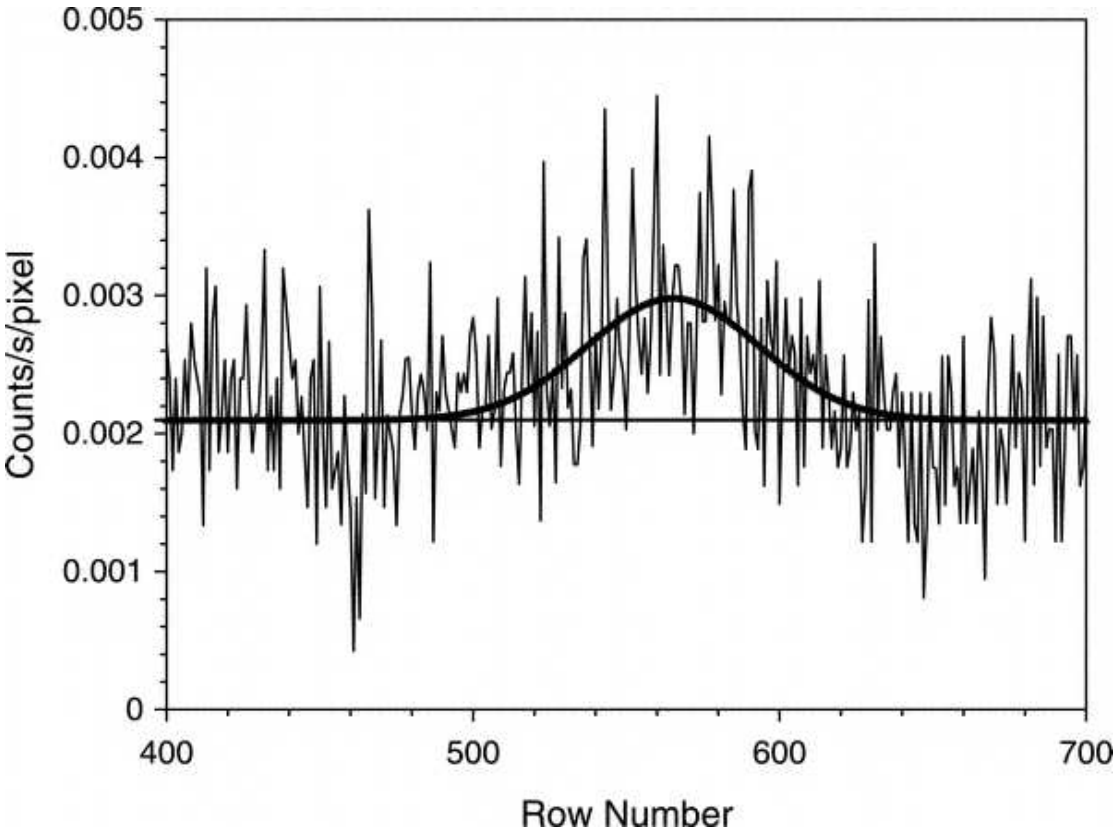

FIGURE 2.4: Profile of LiF LWRS aperture used to measure the integrated diffuse emission at band 1A2. The aperture limit is 510 – 620 and the background limits are the rows 450 – 520 and 620 – 670. The fitted Gaussian is with confidence limit of 90% which is shown by thick line (Murthy & Sahnow 2004).

Å (2A1), 1112 Å (2A2), 1056 Å (2B1). The data from the 2B2 detector do not add any value to the diffuse sky determination because of its much lower sensitivity. The bands used for the extraction diffuse emission are listed in Table 2.1 and shown in Figure (2.5) on top of a spectrum of the diffuse observation in N11, one of the brighter diffuse region of the LMC. The integrated flux of each band is marked by a solid circle at its effective wavelength.

Although we immediately rejected all observations which specifically observed a bright star in the LWRS aperture, there were others where a star was coincidentally in the aperture in the regions of high stellar density. These were identified and rejected through their FWHM (Figure 2.4), which is less than 20 pixels for a point source but about 30 pixels for an aperture filling diffuse source.

TABLE 2.1: Bands Used for Extraction of Diffuse Emission

Number	Bands	Wavelength Range (Å)	Effective Wavelength (Å)
1	1A1	987.70 – 1020.77	1003.93
2	1A2	1034.84 – 1081.37	1058.11
3	1B1	1100.28 – 1133.69	1117.00
4	1B2	1133.70 – 1180.07	1156.88
5	2A1	1175.32 – 1141.97	1158.65
6	2A2	1128.57 – 1095.03	1111.80
7	2B1	1069.11 – 1035.41	1056.00

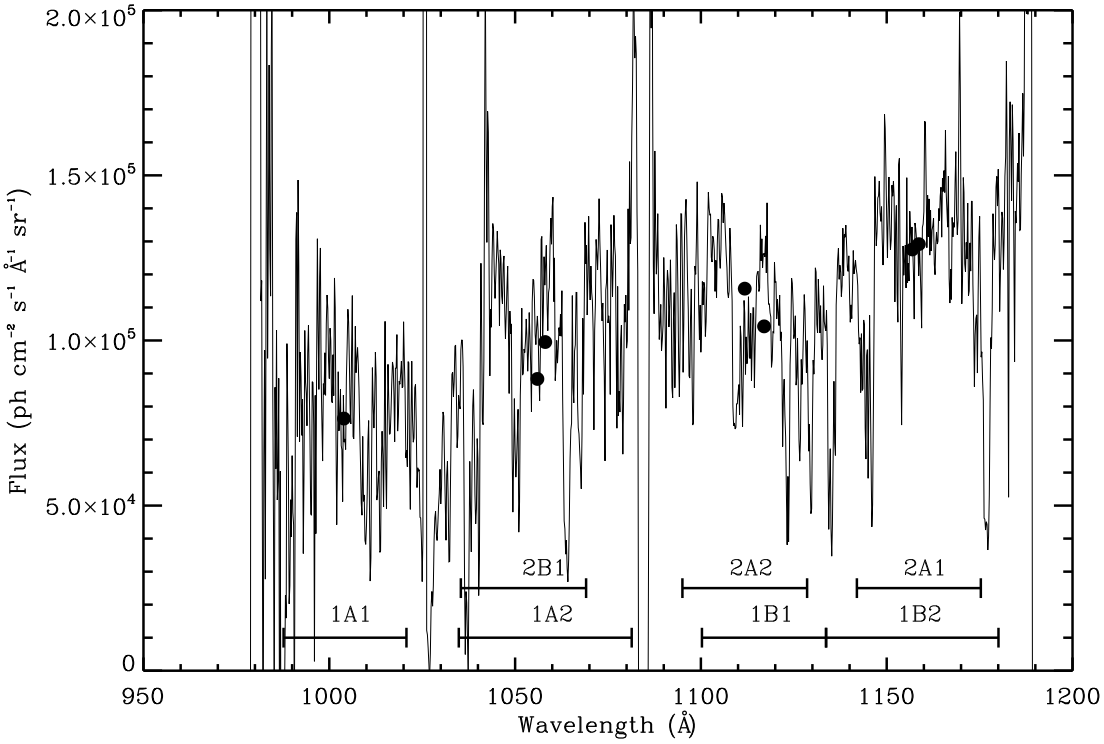

FIGURE 2.5: Spectrum of N11 (PGMW-3053) showing the seven wavelength bands that have been integrated to obtain the FUV diffuse emission. The wavelength range is marked by horizontal bars at the bottom of the spectrum and the integrated fluxes of each band by solid circle at their effective wavelengths.

2.5 *Ultraviolet Imaging Telescope (UIT)*

2.5.1 *UIT* Instrument

The *Ultraviolet Imaging Telescope (UIT)* flew onboard the Space Shuttle Columbia as part of the Astro payload in December 1990 and again in March 1995. This payload consisted of three co-mounted ultraviolet instruments: the *UIT*, the *Hopkins Ultraviolet Telescope (HUT)*, and the *Wisconsin Ultraviolet Photo-Polarimeter Experiment (WUPPE)*. The *UIT* is an f/9 Ritchey-Chretien telescope with 38cm aperture. It was equipped for UV (1200 – 3300 Å) images of astronomical objects with a field of view of $40'$ and resolution of about $3''$. It contained two detector systems: one in the far UV ('B' filters) and one in the near UV ('A' filters). Images were recorded on 70 mm photographic film. The details of the *UIT* instrumentation, pipeline, data reduction and calibration are explained by Stecher et al. (1997). The *UIT* data from both the Astro missions are available at MAST.

2.5.2 *UIT* Observations of the MCs

We have used the calibrated and geometrically corrected images of the *UIT* (2048 x 2048) from the MAST that overlap with some of the *FUSE* observations and are analyzed by Parker et al. (1998) for the LMC and by Cornett et al. (1997) for the SMC. All these images are observed with FUV B-Camera filters: B1 ($\lambda_{\rm eff}$ = 1521 Å and $\Delta\lambda$ = 354 Å) and B5 ($\lambda_{\rm eff}$ = 1615Å and $\Delta\lambda$ = 225 Å) of the *UIT*. But the *FUSE* LWRS aperture size is $30''$ x $30''$ which is much larger than the $1''.13$ pixels of the *UIT*, therefore, we have integrated the $37'$ *UIT* images over 27 x 27 pixel box to measure the *UIT* diffuse flux which is then compared with the diffuse fluxes of the *FUSE* bands.

2.5.3 Conversion of *UIT* flux to Photon units

In order to compare the *FUSE* observations with the *UIT*, the fluxes observed by both the instruments should have the same physical units. The *UIT* fluxes have been converted

from erg cm^{-2} s^{-1} $Å^{-1}$ to photons cm^{-2} s^{-1} sr^{-1} $Å^{-1}$ (Fλ/hν). The effective wavelength of the *UIT* B1 and B5 filters are 1521 Å and 1615 Årespectively. For B1 filter: F erg cm^{-2} s^{-1} $Å^{-1}$ = 1521×F/(6.62×3×10^{-9}) photons cm^{-2} s^{-1} $Å^{-1}$. 1″ equivalent solid angle is $\Omega = (\pi/180 \times 1/3600) \times (\pi/180 \times 1/3600)$. The *UIT* images are with 1″.13 pixels and the solid angle of 1″.13 is $\Omega = (\pi/180 \times 1.13/3600) \times (\pi/180 \times 1.13/3600)$ steredian. For B1 filter: F erg cm^{-2} s^{-1} $Å^{-1}$ = 1521×F/(6.62×3×$10^{-9}/\Omega$) photons cm^{-2} s^{-1} sr^{-1} $Å^{-1}$ and same procedure is followed for B5 filter.

2.6 Stellar Radiation Field Model

We have used Stellar Radiation Field Model of Sujatha et al. (2004), that is one of the tools in Tauvex web page (http://tauvex.iiap.res.in/htmls/tools/fluxcalc) to translate flux of a star from the *UIT* band to the *FUSE* bands. This calculation is based on Kurucz models (Kurucz 1992) and scaled down to visual magnitude which requires three parameters (Visual magnitude, extinction and spectral type) as input to obtain the spectrum of a star in a wavelength range of 900 – 10000 Å. The theory involved in this model is as follows:

If I_0 is the intensity at the surface of a star, then the reduced intensity of the beam of the star after traveling through a dust cloud of optical depth τ is,

$$I = I_0 e^{-\tau} \tag{2.1}$$

$$but \quad I = 4\pi d^2 f \quad and \quad I_0 = 4\pi r^2 f_0 \tag{2.2}$$

$$So, \quad 4\pi d^2 f = 4\pi r^2 f_0 e^{-\tau} \tag{2.3}$$

where f = flux of a star at a distance 'd' and r = radius of the star.

$$f = (r/d)^2 f_0 e^{-\tau} \tag{2.4}$$

If f_0 = Kurucz flux at 5500 Å= K, then

$$f = (r/d)^2 K e^{-\tau} = \Gamma K e^{-\tau} \tag{2.5}$$

where Γ = Scaling factor. From the flux magnitude relation, we know,

$$m_1 - m_2 = -2.5log(f_1/f_2) \tag{2.6}$$

The most popular standard and reference for all broad band photometry is the star Vega (spectral type A), whose apparent magnitude is zero. Substituting the flux density in a given filter of Vega for f_2 and putting $m_2 = m_{vega} = 0$, the zero magnitude flux ($3.64e^{-9}$ erg $cm^{-2}sec^{-1}\mathring{A}^{-1}$) and m_1 = V, we get

$$f = 3.64e^{-9} \times 10^{-V/2.5} \tag{2.7}$$

Hence finally,

$$\Gamma K(5500\mathring{A})e^{-\tau} = 3.64 \times 10^{-9} \times 10^{-V/2.5} \tag{2.8}$$

where $\tau = A_V/1.0863 = E(B\ \ V).R_V/1.0863$. The extinction and visual magnitude are the unknown parameters which is to be supplied. Assuming these and using the Kurucz model flux (K) of appropriate spectral type, the scale factor, Γ is estimated and then the modeled spectrum of a star is obtained.

2.7 Calculation of Errors in Diffuse Fraction

FUV diffuse fraction = diffuse flux/(diffuse flux + stellar flux)
DF = Diffuse *FUSE* flux
DU = Diffuse *UIT* flux
R = slope of the *FUSE*- *UIT* correlation = *FUSE*/UIT
SF = Stellar flux
df = *FUSE* diffuse fraction
DF = R × DU
er_{DF} = (er_R/R + er_{DU}/DU) × DF
where er_R is the error in R calculated from the least square fitting of *FUSE* and *UIT* correlation, er_{DU} is error in DU = 10% obtained (Parker et al. 1998).
df = DF/(DF + SF)
df_{max} = (DF + er_{DF})/[(DF - er_{DF}) + (SF - er_{SF})]
df_{min} = (DF - er_{DF})/[(DF + er_{DF}) + (SF + er_{SF})]
Maximum error in df = df_{max} - df
Minimum error in df = df - df_{min}

Chapter 3

Far Ultraviolet Diffuse Emission from the Large Magellanic Cloud

3.1 Introduction

The LMC and the SMC are two dwarf irregular galaxies visible in the southern hemisphere known as Magellanic Clouds (MCs). The irregular structure of MCs may be due to the tidal interaction between them and with the MW. The MCs were discovered by Ferdinand Magellan on his voyage in 1519. Both the galaxies are orbiting the MW and thus, are members of the local group of galaxies.

A long tail of gas extending from the MCs is called the Magellanic Stream. This is only visible in radio wavelength and its origin is believed to be due to the gravitational interaction between the MW and the MCs. There is a bridge of neutral hydrogen gas connecting the SMC and the LMC, which is evidence of tidal interaction between both the galaxies. Streamers of gas that is being stripped from the MCs and falling into the MW is called the Leading Arm (Figure 3.1).

The LMC spans 8° across the sky with the center RA: 05h 23m 34.5s (80.89°) and Dec: -69° 45′ 22″ (-69.76°) (gl = 280.46° and gb = -32.88°). It was considered the nearest galaxy to the MW (50 kpc; Feast 1999) until the discovery of the Sagittarius

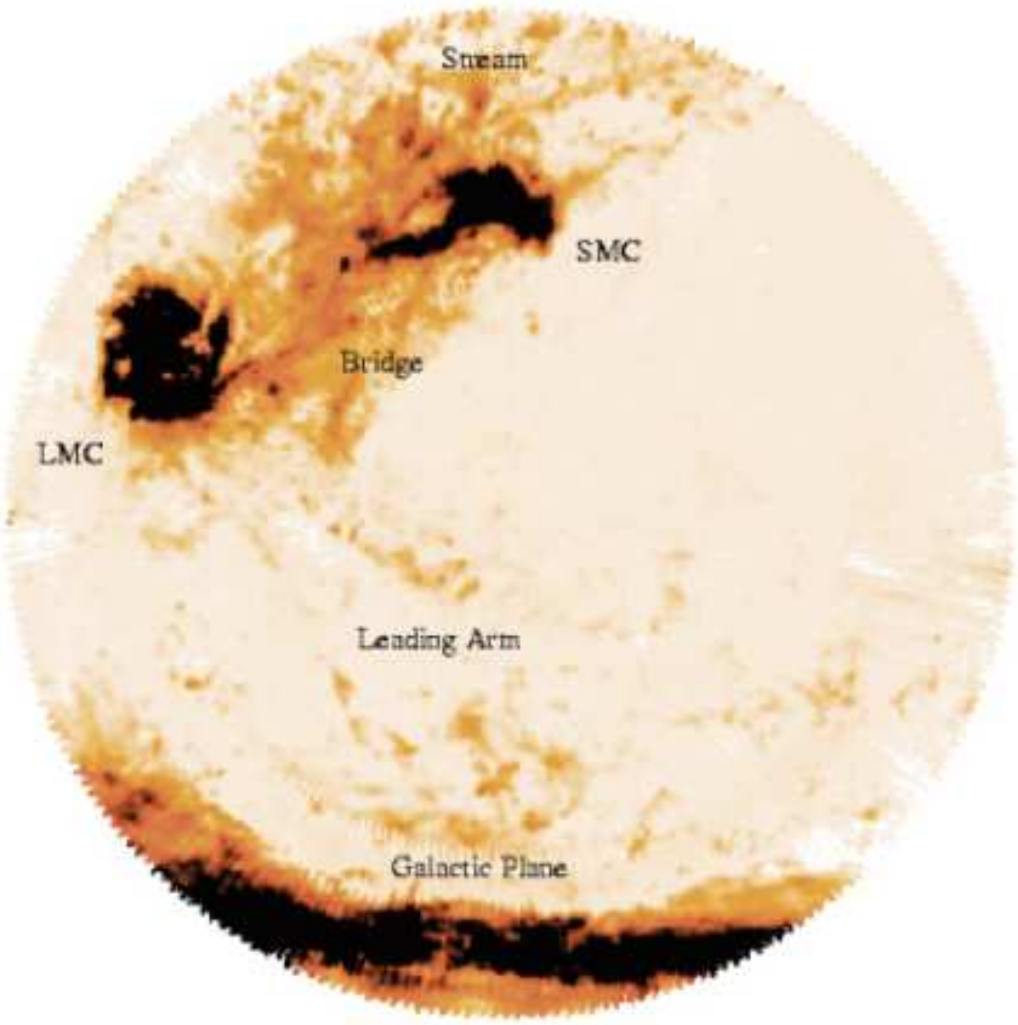

FIGURE 3.1: CSIRO's Parkes radio telescope image of the MCs.

Dwarf Elliptical Galaxy and Canis Major Dwarf Galaxy. It is a treasure house of variety of astronomical objects with rich in gas and dust, and home to the supernova 1987A, 60 globular clusters, 400 planetary nebulae, 700 open clusters, 32 known supernova remnants, and more than 30 billion stars. Two morphologically analogous and immense star forming regions in the LMC are the 30 Doradus , and the N11 region, present in diametrically opposite end of the prominent central Bar. 30 Doradus, the largest H II region in the LMC is the largest star forming region in the local group of galaxies. The energy for this nebula comes from a central star cluster R136 (comprising of O type stars) which makes the nebula visible. N11 is the second largest H II region in the LMC after 30 Doradus, and is home to several associations of massive stars; LH9, LH10, LH13, and LH14 (Lucke & Hodge 1970). The LMC has a mass of 9 $\times 10^9 M_\odot$ (van der

Marel et al. 2002), and a star formation rate of 0.1 $M_{\odot}$/yr (Whitney et al. 2008).

The LMC provides a very different view of the ISM than is possible either from observations of the MW or of other, more distant galaxies. At a distance of 50 kpc (Feast 1999), it is far enough that we can get an overview of processes in the entire galaxy but close enough that we can distinguish between the different sources. It is also oriented almost face-on (viewing angle of 35°; van der Marel & Cioni 2001) which allows study of the ISM emissions without any confusion along the line of sight. The LMC has lower metallicity ($Z \approx 0.3 - 0.5\ Z_{\odot}$; Westerlund 1997) consistent with the reduced dust to gas ratio ($\frac{E_{B-V}}{N_H} \simeq 4.5 \times 10^{-23}$ mag cm^2/H; 26% less than the MW). The ratio, $\frac{A_V}{N_H}$ increases from the outskirts of the LMC towards the 30 Doradus star-forming region which could be either due to a systematic increase of the dust abundance or the presence of an additional gas component not traced by H I. The extinction curve of the LMC with a weaker bump at 2175 Å and a steeper FUV rise is different from the MW (Clayton & Martin 1985; Misselt et al. 1999; Gordon et al. 2003) although it is similar in the visible and near-IR (Clayton & Martin 1985).

Since its discovery, LMC has been center of many surveys at different wavelengths. The distribution of H I has been mapped at low resolution by Luks & Rohlfs (1992) and at high resolution by Kim et al. (1998) showing that N(H I) in the LMC is chaotic with hundreds of clumps, shells, filaments. The ionized-gas content has been imaged in Hα photographs (Meaburn 1980; Kennicutt & Hodge 1986) and in the radio continuum (Haynes et al. 1991; Dickel et al. 2005) and both shows a variety of interstellar shells, ranging more than a few hundred parsecs across. The stellar contents of the LMC have been widely studied by photometry of stars from the near-IR to the UV bands (Parker et al. 1998; Ita et al. 2004; Zaritsky et al. 2004; Blum et al. 2006; Kato et al. 2007). Soft X-ray images of the LMC have been obtained by *ROSAT* (Snowden & Petre 1994), revealing a variety of discrete sources like supernova remnants and X-ray binaries. CO surveys of molecular gas (Israel et al. 1986; Cohen et al. 1988; Fukui et al. 1999, 2008) depicts individual molecular structures in the LMC. Howk et al. (2002a) surveyed the distribution and kinematics of highly ionized gas O VI towards 12 early type stars and Lehner & Howk (2007) analyzed the absorption of O VI, C IV, Si IV and N V ions towards four early type stars in the LMC which provide crucial details about the environments that may be probed through the study of these ions.

The recent high angular resolution IR studies by *Spitzer* Surveying the Agents of Galaxy

Evolution (SAGE) legacy survey (Meixner et al. 2006; Bernard et al. 2008) and low angular resolution surveys by *IRAS* and *DIRBE* (Sauvage et al. 1990; Sakon et al. 2006) have allowed the observer to resolve separation of the diffuse emission from the point sources. This is an important pre-requisite for understanding the physics of dust emission, since the emission depends strongly on the intensity of the ISRF and on the relative distribution of dust and stars. The most comprehensive survey of dust and gas in the LMC has come from Bernard et al. (2008) and Paradis et al. (2009) using a variety of sources including new observations with the *Spitzer Space Telescope* (Meixner et al. 2006). Bernard et al. (2008) found that there was a modification of the dust population in the LMC as compared with the MW, perhaps through the erosion of large grains in the ISM.

Different regions in the LMC have significantly varying stellar population,dust and gas distribution. The 30 Doradus, N11, N4, N70 regions are rich in OB associations and young stars while the LMC bar region is mostly populated by old stars. The LMC bar region is rich in gas and molecules incorporated with fresh dust out flowing from AGB stars where as the 30 Doradus and the regions around it have a more evolved and relatively bigger size dust population (Paradis et al. 2009). The results of Paradis et al. (2009) show that each dust component could have different origin and evolution in the ISM; they predicted that VSGs could have originated from shattering of BGs where as PAHs could have been injected into the ISM during the mass loss from old stars. The relative abundance of PAHs is more in bar and molecular cloud regions where as the VSGs abundance is more over the 30 Doradus region. The distinct spatial distribution of the PAHs and VSGs agrees the trend that PAHs abundance follows the more quiescent environments while the VSGs abundance follows the star formation activity. It is also evidenced that these two dust components could have different origin or different processing in the ISM of the LMC (Paradis et al. 2009).

3.2 Ultraviolet Observations of the LMC

The LMC is an ideal location to study the connection between dust and diffuse UV light. The first imaging observations of the LMC in the UV were by Page & Carruthers (1981) using the S201 FUV camera during the Apollo 16 mission followed by Smith et al. (1987) from a rocket experiment and Parker et al. (1998) from the *UIT* on board the Space

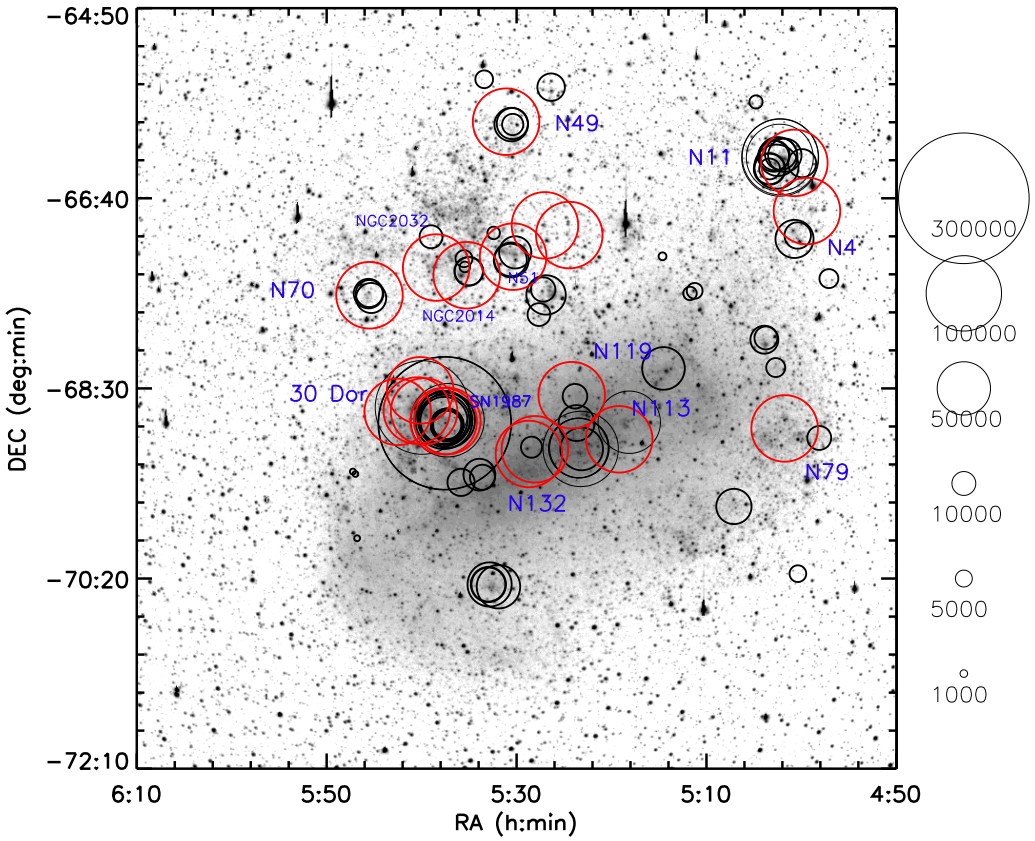

FIGURE 3.2: LMC R-band image from Bothun & Thompson (1988) with the *FUSE* observations represented as circles with area proportional to the observed surface brightness.The red circles represent the 37′ *UIT* field of observations.

Shuttle Columbia. Observations of the diffuse UV light track the transfer of radiation from the stellar radiation to the interstellar medium with the absorbed radiation re-emitted as thermal emission in the infrared. The diffuse UV radiation is about 25% of the total radiation emitted from the LMC (Parker et al. 1998) and understanding its distribution is important to models of galactic evolution. More recently, Cole et al. (1999a) used the rocket-borne *Wide-Field Imaging Survey Polarimeter (WISP)* to map the scattered light in the near ultraviolet (2150 Å), finding that the scattered light is actually a complex combination of the relative geometry of the dust and the stars. It is not sufficient to merely have bright stars or to have dust: both must be present to show the scattered light. In this work, we use serendipitous observations made with the *FUSE* to report, for the first time, measurements of the diffuse FUV (1000 - 1150 Å) emission in an external galaxy.

3.3 FUV Diffuse Emissions in the LMC

There were more than 600 *FUSE* observations within 5° of the LMC. We downloaded them and first rejected all point source observations within the LWRS using the Object Class from the *FUSE* archive. This gave a total of 172 observations. Then we were left with 81 observations of the diffuse radiation in different parts of the LMC after checking the FWHM of the LWRS aperture for the diffuse sources. The details of the diffuse observations are given on Table 3.2. The intensities of FUV diffuse radiation range from around 10^3 photons cm^{-2} s^{-1} sr^{-1} Å^{-1} to as high as 3×10^5 photons cm^{-2} s^{-1} sr^{-1} Å^{-1} near 30 Doradus. Although we have listed all the diffuse values for completeness, we note that the effective lower limit for the detection of diffuse radiation with *FUSE* is about 2000 photons cm^{-2} s^{-1} sr^{-1} Å^{-1} (Murthy & Sahnow 2004). The LMC is at a high Galactic latitude where the contribution from the Galactic diffuse radiation will be relatively small and we have estimated it to be on the order of 500 photons cm^{-2} s^{-1} sr^{-1} Å^{-1}, based on nearby *Voyager* observations by Murthy et al. (1999). We have plotted the diffuse flux in one of the *FUSE* bands (1B1 at 1117 Å) as circles with areas proportional to the observed surface brightness in Figure 3.2. There is an excellent correlation between the diffuse FUV flux observed in 1B1 and each of the other *FUSE* bands with linear correlation coefficients of better than 0.9 in each case and a similar plot would be obtained for any of the other bands. One of the correlation plots between the *FUSE* bands is shown in Figure 3.3. The correlation co-efficient of the plot is 0.99 and the best fit line is with slope 0.62 and an offset of -32 photons cm^{-2} s^{-1} sr^{-1} Å^{-1}.

Cole et al. (1999a) found that their diffuse light (2150 Å) was dominated by the N11 complex in the northwest LMC with a surface brightness of 10^4 photons cm^{-2} s^{-1} sr^{-1} Å^{-1}, which they identified as a giant reflection nebula. Although, certainly bright in our *FUSE* observations, by far the brightest of our observed regions is around 30 Doradus (the Tarantula Nebula), which was not observed by *WISP*. As mentioned above, the *FUSE* targets have been selected for their proximity to bright stars and as a result, almost all of our observed diffuse regions are also bright. The FUV diffuse emission in the LMC is predominantly due to the scattering of the star light from the OB associations and shows a large variation in a small angular scale, particularly in 30 Doradus and N11 regions (Figure 3.2). These regions are rich in hot OB stars of UV magnitudes less than 10 (Parker et al. 1998) and show significant variation in stellar density in a small angular scale.

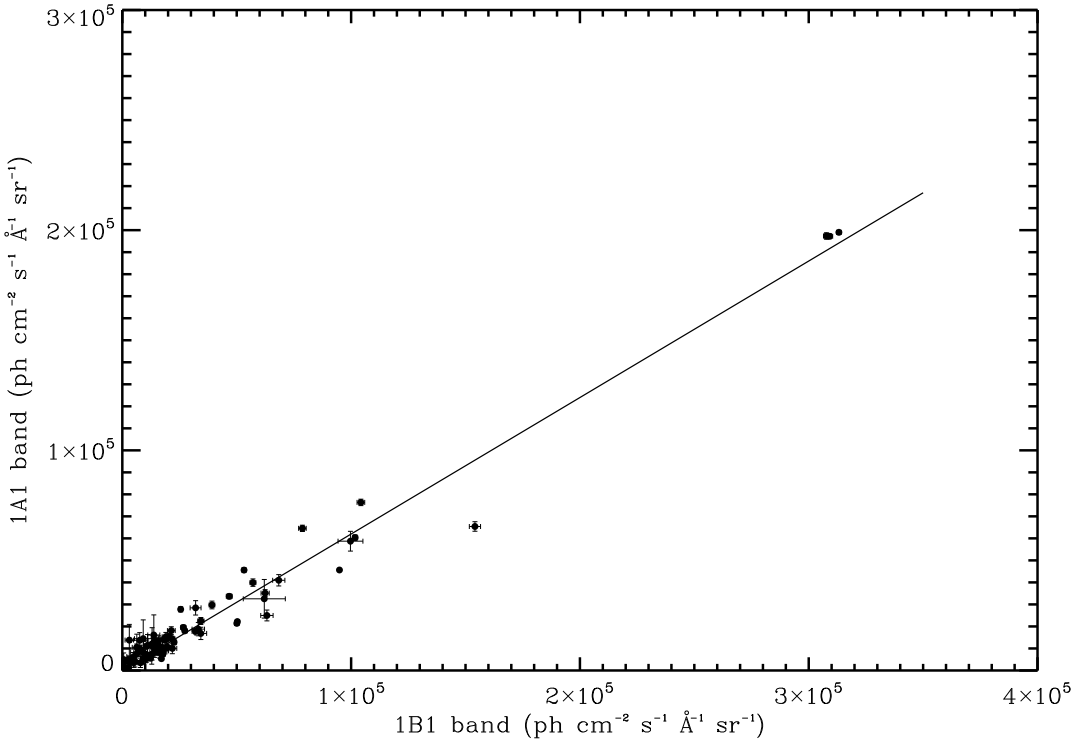

FIGURE 3.3: The correlation between 1A1 and 1B1 band of *FUSE*.

3.4 *FUSE* – *UIT* Correlation

We have extensively used the *UIT* data to estimate the fractional contribution of FUV diffuse radiation in the LMC. Wide field far ultraviolet images of the regions of nebulosity cataloged by Davies et al. (1976)(DEM) have been obtained by the *UIT*. Of the H II regions in the catalog of DEM, the *UIT* covers 102 regions in the LMC and 74 regions in the SMC. Out of them 16 fields from the LMC have been analyzed by Parker et al. (1998) and we have used their images for the calculation of diffuse UV emission. Parker et al. (1998) have measured the total integrated aperture flux as well as stellar flux within each of the regions and they have also provided a catalog of FUV magnitudes derived from point spread function photometry for 37,333 stars of these regions.

Of the 81 *FUSE* locations, 43 overlapped with 10 *UIT* field of observations in the LMC for which we measured the *UIT* flux. The *UIT* fluxes were then converted from erg cm^{-2} s^{-1} $Å^{-1}$ to photons cm^{-2} s^{-1} sr^{-1} $Å^{-1}$. We found a strong correlation between *UIT* flux and diffuse flux in 1B1 band (Figure 3.4). Three points in the 30 Doradus region

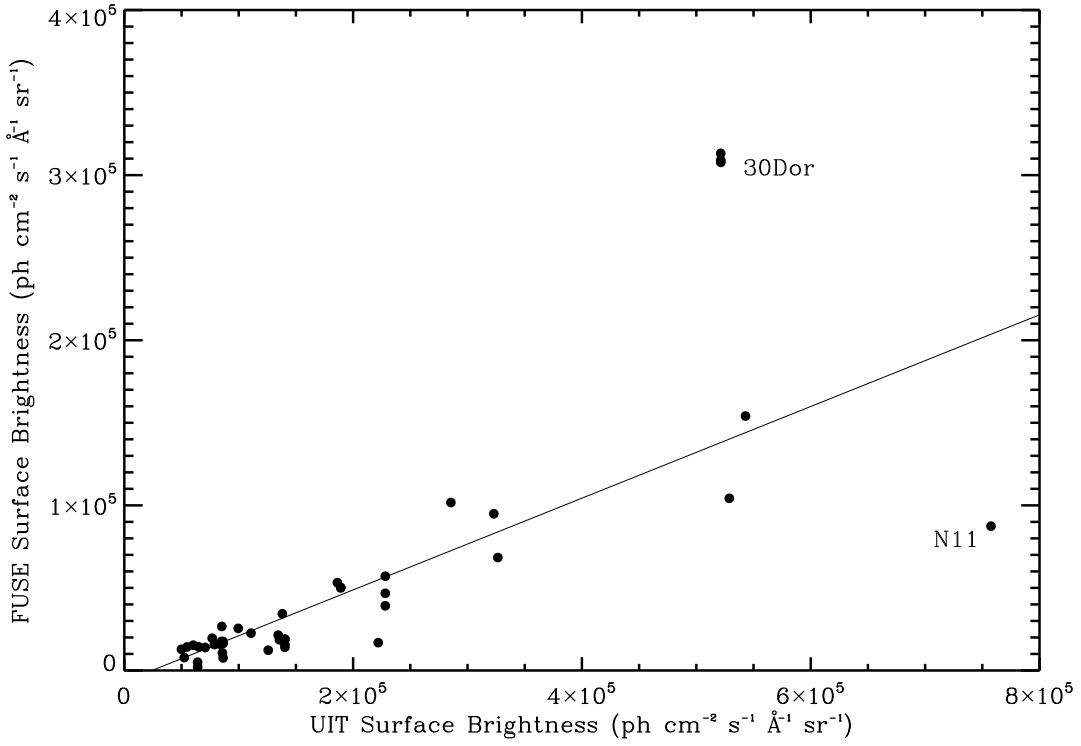

FIGURE 3.4: Correlation between the *FUSE* (1B1) and the *UIT* surface brightness is shown. The correlation coefficient is 0.78 but rises to 0.92 if four points (three of the 30 Doradus and one of the N11 points) are removed. The best fit is the line with slope 0.28 and an offset of -6730 photons cm^{-2} s^{-1} sr^{-1} $Å^{-1}$. Similar plots are obtained for the other six *FUSE* bands. Errors in the observations are small (relative to Y-axis scale) to be visible and are not shown.

have a relatively higher *FUSE* flux because the radiation field is dominated by O stars in the nebula whereas one observation in N11 had a relatively higher *UIT* flux because the stellar spectrum is much flatter than in other regions. Similar correlation plots of *UIT* diffuse flux with other *FUSE* bands were obtained to determine the best fit slope i.e., *FUSE*/*UIT* ratio.

3.4.1 Calculation of Diffuse Fraction

Rather than deal with absolute values, a useful comparison is to find the fractional amount of diffuse radiation in the field defined as diffuse radiation over total radiation (diffuse + stellar) in each of the *UIT* regions. We obtained the FUV magnitudes of all

TABLE 3.1: Calculation of Far Ultraviolet Diffuse Fraction (DF) for the *FUSE* 1B1 (1117 Å) band.

UIT Field	Total flux *UIT*	DF(*UIT*)	$\frac{FUSE}{UIT}$	Total flux *FUSE*	Stellar flux *FUSE*	DF *FUSE*
30 Doradus	1.50e-10	0.50	0.26	1.91e-11	2.31e-10	0.077
SN1987	3.00e-10	0.28	0.26	2.14e-11	5.63e-10	0.037
N51	1.40e-10	0.55	0.26	1.97e-11	1.89e-10	0.094
NGC-2014	1.50e-10	0.58	0.26	2.22e-11	1.12e-10	0.166
N113	1.30e-10	0.43	0.26	1.43e-11	2.31e-10	0.058
N119	1.90e-10	0.41	0.26	1.99e-11	1.73e-10	0.103
N132	1.20e-10	0.61	0.26	1.87e-11	1.02e-10	0.155
N4	1.00e-10	0.69	0.26	1.76e-11	8.64e-10	0.169
N11	2.10e-10	0.43	0.26	2.31e-11	2.74e-10	0.078
N70	6.30e-11	0.84	0.26	1.35e-11	2.17e-11	0.384

the stars contained in each of the *UIT* field from the catalog of Parker et al. (1998). The magnitude was converted to flux using Hayes & Latham (1975) formula: m(λ) = -2.5logF(λ) - 21.1. Then the flux of a star of given spectral type was translated from *UIT* bands to *FUSE* bands using Stellar Radiation Field Model of Sujatha et al. (2004) that is based on Kurucz models (Kurucz 1992) and the fluxes of all the stars in a given field were summed to obtain the total stellar flux in *FUSE* bands. The total integrated aperture flux and the fraction of the total flux in diffuse radiation in each field in the *UIT* band is estimated by Parker et al. (1998). With the observed *FUSE*/*UIT* diffuse ratio, we could then calculate the total amount of diffuse radiation at each of the *FUSE* bands which is the *FUSE*/*UIT* times the total *UIT* diffuse flux of that region and thus, the fraction of total light emitted as diffuse emission *i.e.*, diffuse/(stellar + diffuse). We have not considered extinction as it will affect both the stellar and diffuse flux equally and so will cancel out. Table 3.1 shows the calculation of diffuse fraction for the *UIT* fields at 1B1 band of the *FUSE*. These fractions range from 5% to 20% of the total at 1100 Å, with a high of 45% in the superbubble N70, with an observed error of 12% – 17%. The comparable estimate for the MW is 10% (Parravano et al. 2003). The error bars in the diffuse fraction were empirically calculated by taking the extremes of the observed fluxes.

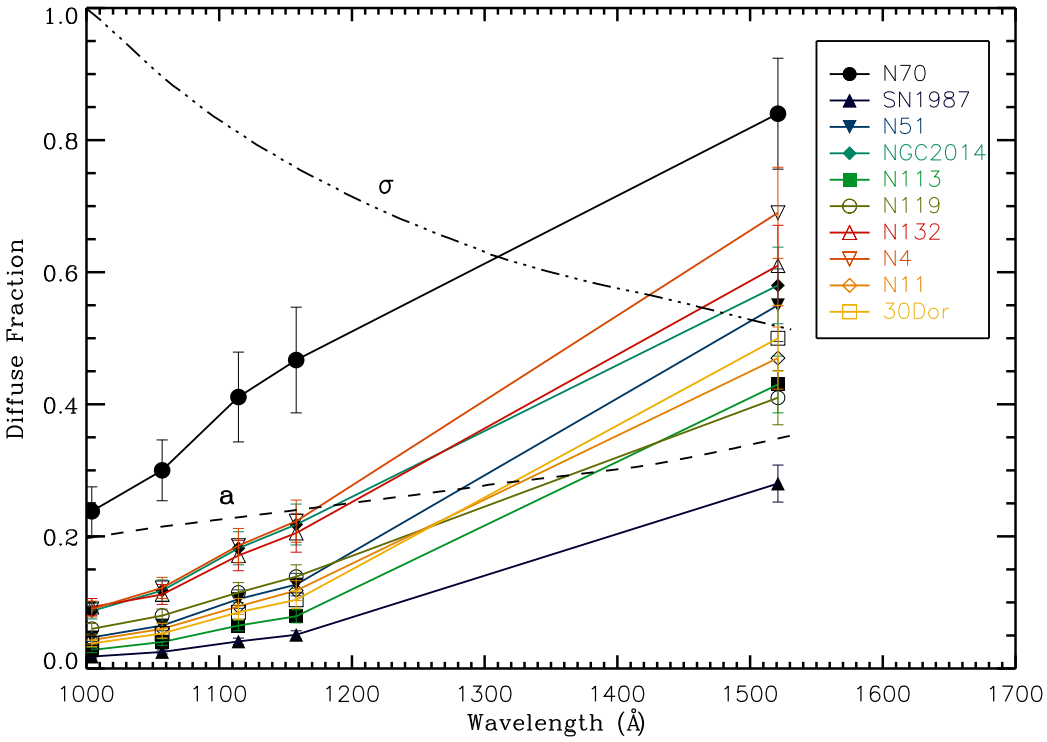

FIGURE 3.5: Variation of diffuse fraction against wavelength for different *UIT* regions of the LMC. Also plotted are the albedo (dashed line) and cross-section (dot-dashed line divided by 7.6×10^{-22}) from model calculations by Weingartner & Draine (2001). The seven observed *FUSE* bands are shown at four wavelengths (1004, 1057, 1114.5 and 1158 Å), where the intensities at 1057, 1114.5 and 1158 Å are average of the 1A2 & 2B1 bands, 1B1 & 2A2 bands, and 1B2 & 2A1 bands respectively. The error bars were empirically calculated by taking the extremes of the observed fluxes which range from 12% – 17% of the data.

3.5 Discussion

Although some part of the variation of diffuse fraction in different regions of the LMC may be due to the dust distribution, it is likely that much of the stellar radiation is non-local, as noted by Cole et al. (1999a) *i.e.*, the diffuse light may come from stars far away from the observed area. In our Galaxy, this is seen as scattering of galactic plane star light by high latitude dust clouds (Jura 1980); in the LMC, light from the OB associations will be scattered by distant dust. The shape of the diffuse fraction is essentially the same in all the 10 regions rising by a factor of about 5 from 1000 to 1500 Å. The lower value of diffuse fraction at shorter wavelength implies that most of the heating of the interstellar dust comes in the FUV which is well proved by Law et al.

(2011) for star forming galaxies using Spitzer data and dusty radiative transfer model. The variation of diffuse fraction with wavelength is consistent with variation of albedo (dashed line) and cross-section (dot-dashed line) of the grains in the FUV (Figure 3.5) saying that less light is scattered in FUV.

Cole et al. (1999b) have attempted to model the distribution of diffuse light in the *WISP* data by scattering the light of OB associations in the LMC from a dust distribution which decays exponentially with radius and with a hyperbolic secant with distance from the plane. They found that although their models did match the overall morphology of the observations, it was difficult to constrain the parameters because of the uncertainty in many of the physical properties of the ISM in the LMC, particularly in its clumping. Nevertheless they did find that 30 Doradus dominated the diffuse emission in the eastern LMC, a conclusion borne out by our *FUSE* observations in the FUV.

3.6 Conclusions

We have obtained the first FUV (1000 – 1150 Å) spectra of the diffuse radiation in an external galaxy using serendipitous *FUSE* observations of targets in the LMC. Most of these observations are near OB associations and the diffuse emission is bright, ranging from 5% to 20% of the total flux in the region. This fraction is much less than the corresponding fraction emitted at 1500 Å suggesting that the largest part of the heating of the interstellar dust occurs in the FUV.

TABLE 3.2: Details of the *FUSE* observations in the LMC.

Target Name	RA	Dec	LiF 1A1	LiF 1A2	LiF 1B1	LiF 1B2	LiF 2A1	LiF 2A2	LiF 2B1
SK-68.75	80.91	-68.15	(14.46 ± 8.52)E+03	(4.94 ± 1.41)E+03	(9.12 ± 3.79)E+03	(8.11 ± 2.98)E+03	(7.02 ± 2.31)E+03	(4.87 ± 1.20)E+03	(4.55 ± 1.25)E+03
SK-67.106	81.65	-67.55	(18.12 ± 1.73)E+03	(20.55 ± 1.05)E+03	(21.41 ± 1.71)E+03	(25.25 ± 1.76)E+03	(23.17 ± 1.50)E+03	(22.83 ± 1.51)E+03	(20.15 ± 1.52)E+03
SK-67.107	81.67	-67.55	(14.10 ± 1.47)E+03	(168.88 ± 8.97)E+02	(18.59 ± 1.57)E+03	(19.56 ± 1.85)E+03	(19.50 ± 1.35)E+03	(17.36 ± 1.06)E+03	(19.80 ± 1.48)E+03
PGMW-3053	74.30	-66.39	(76.34 ± 1.46)E+03	(995.20 ± 8.89)E+02	(104.27 ± 1.67)E+03	(127.56 ± 1.91)E+03	(129.17 ± 1.34)E+03	(115.69 ± 1.17)E+03	(88.34 ± 1.36)E+03
PGMW-3070	74.31	-66.39	(64.55 ± 1.42)E+03	(798.40 ± 8.64)E+02	(78.71 ± 1.66)E+03	(86.39 ± 2.00)E+03	(107.84 ± 1.72)E+03	(101.11 ± 1.57)E+03	(87.35 ± 1.56)E+03
PGMW-3168	74.36	-66.38	(19.53 ± 1.09)E+03	(247.82 ± 6.65)E+02	(26.67 ± 1.13)E+03	(28.34 ± 1.04)E+03	(35.18 ± 1.17)E+03	(33.51 ± 1.27)E+03	(26.56 ± 1.18)E+03
PGMW-3223	74.29	-66.35	(8.92 ± 2.49)E+03	(12.61 ± 1.51)E+03	(17.59 ± 2.61)E+03	(19.16 ± 3.60)E+03	(22.85 ± 1.62)E+03	(6.73 ± 1.14)E+03	(17.96 ± 2.41)E+03
PGMW-3264	74.45	-66.37	(10.00 ± 1.77)E+03	(12.39 ± 1.08)E+03	(15.69 ± 2.38)E+03	(13.34 ± 2.57)E+03	(19.55 ± 1.69)E+03	(17.68 ± 1.33)E+03	(17.17 ± 2.32)E+03
PGMW-3271	74.48	-66.38	(8.86 ± 1.63)E+03	(126.68 ± 9.93)E+02	(16.86 ± 1.69)E+03	(17.20 ± 1.51)E+03	(18.51 ± 2.22)E+03	(19.01 ± 2.15)E+03	(14.50 ± 1.60)E+03
SK-67D168	82.98	-67.51	(6.32 ± 3.84)E+03	(5.21 ± 2.33)E+03	(5.02 ± 3.05)E+03	(7.74 ± 4.48)E+03	(5.02 ± 1.80)E+03	(5.82 ± 1.53)E+03	(9.02 ± 1.97)E+03
SK-65D15	75.05	-65.81	(13.78 ± 7.13)E+03	(5.45 ± 4.33)E+03	(3.05 ± 1.85)E+03	(4.69 ± 1.72)E+03	(20.73 ± 1.22)E+03	(19.32 ± 1.41)E+03	(15.33 ± 1.59)E+03
SK-65D63	82.17	-65.59	(4.00 ± 2.43)E+03	(5.71 ± 1.47)E+03	(5.51 ± 3.35)E+03	(2.21 ± 1.34)E+03	(1.88 ± 1.14)E+03	(1.82 ± 1.11)E+03	(16.10 ± 9.78)E+03
N132D	81.25	-69.58	(9.68 ± 1.78)E+03	(11.80 ± 1.08)E+03	(7.81 ± 2.04)E+03	(16.26 ± 1.72)E+03	(18.48 ± 1.09)E+03	(15.65 ± 1.13)E+03	(11.41 ± 1.47)E+03
DEML71SW	76.56	-67.91	(3.74 ± 2.27)E+03	(6.39 ± 1.38)E+03	(3.17 ± 1.92)E+03	(4.00 ± 2.43)E+03	(3.21 ± 1.95)E+03	(3.06 ± 1.86)E+03	(6.32 ± 3.84)E+03
SK-66-40	74.56	-66.52	(8.40 ± 2.86)E+03	(12.73 ± 1.74)E+03	(16.39 ± 3.08)E+03	(16.90 ± 2.57)E+03	(16.13 ± 3.19)E+03	(14.26 ± 1.63)E+03	(10.60 ± 2.44)E+03
SK-66-40	74.56	-66.52	(13.72 ± 3.46)E+03	(13.25 ± 2.10)E+03	(7.61 ± 3.64)E+03	(8.30 ± 3.81)E+03	(18.75 ± 2.73)E+03	(10.53 ± 1.76)E+03	(11.29 ± 2.80)E+03
SK-66-40	74.56	-66.52	(10.42 ± 3.20)E+03	(13.38 ± 1.94)E+03	(17.52 ± 3.56)E+03	(22.74 ± 5.57)E+03	(21.06 ± 3.11)E+03	(29.38 ± 9.22)E+02	(9.35 ± 2.16)E+03
LH91486	74.38	-66.49	(22.49 ± 1.57)E+03	(283.49 ± 9.56)E+02	(34.33 ± 1.35)E+03	(35.21 ± 1.53)E+03	(35.17 ± 1.51)E+03	(320.63 ± 8.21)E+02	(28.48 ± 1.17)E+03
LH103073	74.3	-66.38	(60.34 ± 1.26)E+03	(820.77 ± 7.71)E+02	(101.72 ± 1.14)E+03	(97.21 ± 1.52)E+03	(92.71 ± 4.40)E+03	(80.79 ± 2.77)E+03	(64.62 ± 3.68)E+03
LH103204	74.18	-66.36	(10.71 ± 1.72)E+03	(12.81 ± 1.05)E+03	(19.54 ± 1.70)E+03	(18.85 ± 1.83)E+03	(14.09 ± 1.61)E+03	(13.68 ± 1.38)E+03	(12.82 ± 1.96)E+03
BREY22	79.73	-69.61	(58.72 ± 4.49)E+03	(79.45 ± 2.73)E+03	(99.70 ± 5.44)E+03	(104.37 ± 6.25)E+03	(138.96 ± 5.32)E+03	(114.94 ± 5.14)E+03	(92.29 ± 4.08)E+03
BREY22	79.70	-69.61	(28.45 ± 5.35)E+03	(40.47 ± 2.94)E+03	(51.77 ± 5.81)E+03	(58.89 ± 6.43)E+03	(58.77 ± 6.49)E+03	(44.62 ± 5.57)E+03	(42.09 ± 3.99)E+03
BREY22	79.77	-69.60	(35.13 ± 1.59)E+03	(487.56 ± 9.67)E+02	(62.41 ± 1.78)E+03	(60.65 ± 2.15)E+03	(61.66 ± 1.67)E+03	(58.06 ± 1.57)E+03	(50.30 ± 1.29)E+03
BREY22	79.79	-69.60	(24.99 ± 2.46)E+03	(47.62 ± 1.49)E+03	(63.18 ± 2.70)E+03	(77.61 ± 2.35)E+03	(103.57 ± 1.93)E+03	(94.36 ± 1.88)E+03	(74.09 ± 1.95)E+03
BREY22	79.80	-69.60	(32.56 ± 8.77)E+03	(34.36 ± 5.33)E+03	(62.03 ± 9.18)E+03	(7.43 ± 1.23)E+04	(103.28 ± 7.50)E+03	(83.77 ± 9.68)E+03	(45.06 ± 6.62)E+03
SK-71D41	82.50	-71.07	(18.77 ± 3.03)E+03	(27.40 ± 1.84)E+03	(33.19 ± 2.72)E+03	(42.37 ± 2.90)E+03	(18.73 ± 2.57)E+03	(8.54 ± 1.29)E+03	(17.16 ± 2.55)E+03
SK-71D46	82.79	-71.04	(16.83 ± 2.78)E+03	(26.17 ± 1.69)E+03	(34.31 ± 2.52)E+03	(28.06 ± 3.01)E+03	(34.47 ± 2.19)E+03	(28.35 ± 1.57)E+03	(23.25 ± 2.18)E+03
LH114-7	85.74	-67.8	(7.25 ± 4.41)E+03	(5.88 ± 2.68)E+03	(12.86 ± 4.72)E+03	(10.97 ± 1.95)E+03	(8.50 ± 5.16)E+03	(5.85 ± 3.56)E+03	(6.64 ± 4.03)E+03
SK-67D250	85.76	-67.8	(8.97 ± 1.91)E+03	(10.12 ± 1.16)E+03	(15.34 ± 1.81)E+03	(15.52 ± 2.17)E+03	(16.25 ± 1.38)E+03	(15.30 ± 1.47)E+03	16.81 ± 1.60)E+03
SK-69D243	84.52	-69.08	(65.40 ± 2.17)E+03	(9.77 ± 1.32)E+03	(154.11 ± 2.45)E+03	(149.49 ± 2.92)E+03	(190.82 ± 1.67)E+03	(167.48 ± 2.35)E+03	(105.54 ± 1.60)E+03
SNR0450-709	72.62	-70.84	(3.58 ± 2.18)E+03	(3.39 ± 1.32)E+03	(4.89 ± 1.02)E+03	(6.93 ± 1.45)E+03	(1.72 ± 1.04)E+03	(8.10 ± 2.68)E+02	(11.07 ± 4.72)E+03
SNR0454-672	73.64	-67.21	(5.65 ± 1.26)E+03	(112.02 ± 7.70)E+02	(12.27 ± 1.19)E+03	(132.76 ± 9.51)E+02	(80.80 ± 9.16)E+02	(56.81 ± 7.92)E+02	(11.29 ± 1.34)E+03
SNR0454-665	73.70	-66.43	(11.90 ± 2.96)E+03	(25.40 ± 1.80)E+03	(13.92 ± 2.33)E+03	(15.17 ± 2.45)E+03	(9.34 ± 1.65)E+03	(9.09 ± 2.74)E+03	(14.17 ± 2.41)E+03
SNR0509-687	77.25	-68.73	(17.74 ± 1.06)E+03	(342.29 ± 6.45)E+02	(31.94 ± 1.46)E+03	(30.18 ± 1.53)E+03	(51.46 ± 1.43)E+03	(45.98 ± 1.16)E+03	(33.9 ± 1.26)E+03
SNR0523-679	80.77	-67.88	(5.33 ± 1.62)E+03	(81.80 ± 9.85)E+02	(10.46 ± 1.70)E+03	(13.00 ± 1.87)E+03	(8.93 ± 1.60)E+03	(95.59 ± 9.76)E+02	(9.62 ± 1.78)E+03
SNR0534-699	83.50	-69.92	(12.09 ± 7.35)E+03	(8.75 ± 4.46)E+03	(13.00 ± 2.50)E+03	(20.57 ± 6.80)E+03	(14.16 ± 2.23)E+03	(11.72 ± 1.98)E+03	(25.49 ± 9.03)E+03
SNR0547-697A	86.83	-69.69	(15.11 ± 9.18)E+02	(10.75 ± 5.58)E+02	(6.06 ± 3.68)E+02	(7.26 ± 4.41)E+02	(11.76 ± 7.15)E+02	(13.32 ± 8.10)E+02	(8.70 ± 5.29)E+03
SNR0547-697B	86.76	-69.72	(3.30 ± 2.00)E+03	(1.41 ± 1.22)E+03	(5.72 ± 3.47)E+02	(7.68 ± 4.67)E+02	(5.72 ± 3.47)E+02	(7.68 ± 4.67)E+02	16.44 ± 9.99)E+03
SNR0528-672	82.11	-67.25	(13.26 ± 4.79)E+02	(22.67 ± 2.91)E+02	(27.58 ± 5.54)E+02	(41.01 ± 5.23)E+02	(45.47 ± 4.53)E+02	(45.84 ± 4.80)E+02	(38.14 ± 5.65)E+02
SNR0455-687	73.93	-68.65	(7.58 ± 4.44)E+03	(5.66 ± 2.70)E+03	(6.31 ± 1.31)E+03	(6.52 ± 1.48)E+03	(21.39 ± 8.53)E+02	(15.44 ± 6.88)E+02	(11.18 ± 6.00)E+03

Continued on Next Page...

Table 3.2 – Continued

Target Name	RA	Dec	LiF 1A1	LiF 1A2	LiF 1B1	LiF 1B2	LiF 2A1	LiF 2A2	LiF 2B1
SK-68D15	74.29	-68.34	(5.35 ± 2.35)E+03	(6.62 ± 1.43)E+03	(9.22 ± 1.29)E+03	(11.53 ± 1.92)E+03	(5.72 ± 1.53)E+03	(4.92 ± 1.10)E+03	(8.51 ± 2.67)E+03
SK-68D16	74.33	-68.36	(16.1 ± 9.13)E+03	(9.23 ± 5.55)E+03	(13.75 ± 2.63)E+03	(15.89 ± 3.27)E+03	(13.75 ± 2.89)E+03	(8.55 ± 2.55)E+03	(15.23 ± 9.36)E+03
SK-70D32	74.87	-70.18	(10.02 ± 2.39)E+03	(15.05 ± 1.45)E+03	(21.87 ± 1.92)E+03	(23.52 ± 2.00)E+03	(15.51 ± 1.71)E+03	(13.27 ± 1.51)E+03	14.95 ± 1.98)E+03
SK-67D205	83.86	-67.25	(8.15 ± 4.95)E+03	(8.38 ± 3.01)E+03	(9.22 ± 5.60)E+03	(7.74 ± 4.70)E+03	(45.49 ± 2.62)E+03	(49.03 ± 2.29)E+03	(36.57 ± 1.32)E+03
SNR0449-693	72.42	-69.36	(7.43 ± 3.94)E+03	(6.28 ± 2.39)E+03	(10.05 ± 1.43)E+03	(9.12 ± 1.46)E+03	(5.02 ± 1.10)E+03	(6.94 ± 1.21)E+03	(20.57 ± 6.18)E+03
SNR0521-657	80.43	-65.70	(10.95 ± 3.76)E+03	(13.45 ± 2.29)E+03	(13.29 ± 1.04)E+03	(15.12 ± 1.21)E+03	(14.10 ± 1.63)E+03	(14.35 ± 1.34)E+03	(14.69 ± 1.32)E+03
N49-KNOT	81.47	-66.09	(3.48 ± 2.12)E+03	(9.59 ± 1.28)E+03	(7.92 ± 1.17)E+03	(15.68 ± 2.84)E+03	(8.38 ± 2.60)E+03	(7.64 ± 1.81)E+03	(14.80 ± 7.34)E+03
N49-W	81.48	-66.08	(53.71 ± 7.88)E+02	(112.63 ± 4.79)E+02	(170.86 ± 9.18)E+02	(162.75 ± 9.18)E+02	(59.95 ± 9.73)E+02	(82.85 ± 8.11)E+02	(8.79 ± 1.30)E+03
LMCN70-POS2	85.70	-67.85	(11.3 ± 4.42)E+03	(17.01 ± 2.68)E+03	(15.90 ± 2.75)E+03	(18.81 ± 3.13)E+03	(21.49 ± 3.63)E+03	(19.43 ± 3.67)E+03	(29.01 ± 7.38)E+03
HD269217	78.24	-69.32	(40.98 ± 2.57)E+03	(55.38 ± 1.56)E+03	(68.37 ± 2.66)E+03	(72.50 ± 3.18)E+03	(42.52 ± 2.40)E+03	(36.74 ± 2.14)E+03	(31.83 ± 2.11)E+03
SN1987A	83.80	-69.29	(12.95 ± 1.82)E+03	(20.15 ± 1.11)E+03	(14.07 ± 1.32)E+03	(12.48 ± 1.42)E+03	(14.07 ± 1.32)E+03	(12.48 ± 1.42)E+03	(14.07 ± 1.32)E+03
SN1987A	83.80	-69.29	(15.31 ± 1.97)E+03	(22.39 ± 1.20)E+03	(19.03 ± 1.60)E+03	(22.62 ± 1.58)E+03	(9.80 ± 3.62)E+03	(11.89 ± 3.02)E+03	(14.23 ± 3.81)E+03
SN1987A	83.80	-69.29	(13.57 ± 1.13)E+03	(220.86 ± 6.87)E+02	(15.67 ± 1.19)E+03	(21.92 ± 1.50)E+03	(9.71 ± 2.87)E+03	(12.86 ± 3.21)E+03	(14.10 ± 4.03)E+03
SN1987A	83.80	-69.29	(14.09 ± 1.25)E+03	(223.01 ± 7.65)E+02	(18.73 ± 1.08)E+03	(21.08 ± 1.12)E+03	(14.31 ± 2.83)E+03	(16.13 ± 2.45)E+03	(17.29 ± 3.93)E+03
SK-67005	72.65	-67.64	(10.52 ± 5.97)E+03	(5.17 ± 3.62)E+03	(6.30 ± 1.98)E+03	(4.34 ± 1.69)E+03	(6.30 ± 1.98)E+03	(4.34 ± 1.69)E+03	(6.30 ± 1.98)E+03
SN1987A	83.89	-69.24	(29.74 ± 1.74)E+03	(38.74 ± 1.06)E+03	(39.17 ± 1.23)E+03	(44.76 ± 1.58)E+03	(46.51 ± 1.51)E+03	(43.27 ± 1.31)E+03	(34.36 ± 1.28)E+03
SN1987A	83.89	-69.24	(33.67 ± 1.11)E+03	(433.91 ± 6.78)E+02	(46.72 ± 1.27)E+03	(55.68 ± 1.74)E+03	(48.31 ± 1.50)E+03	(46.97 ± 1.23)E+03	(37.27 ± 1.31)E+03
SN1987A	83.89	-69.24	(39.91 ± 1.68)E+03	(53.48 ± 1.02)E+03	(57.08 ± 1.27)E+03	(67.14 ± 1.37)E+03	(61.12 ± 2.34)E+03	(57.83 ± 1.54)E+03	(45.31 ± 1.30)E+03
SN1987A-STAR3	83.78	-69.24	(45.61 ± 1.12)E+03	(622.53 ± 6.80)E+02	(531.92 ± 6.65)E+02	(652.21 ± 7.98)E+02	(57.62 ± 4.17)E+03	(57.70 ± 3.59E+03)	(47.74 ± 1.77)E+03
SN1987A	83.87	-69.24	(456.43 ± 5.94)E+02	(708.79 ± 3.61)E+02	(949.00 ± 5.00)E+02	(1056.00 ± 5.91)E+02	(104.00 ± 1.12)E+03	(892.33 ± 8.35)E+02	(573.13 ± 8.10)E+02
SN1987A-STAR3	83.87	-69.21	(222.15 ± 6.96)E+02	(345.93 ± 4.23)E+02	(502.81 ± 7.98)E+02	(502.53 ± 7.29)E+02	(585.03 ± 6.97)E+02	(517.18 ± 4.93)E+02	(345.56 ± 7.23)E+02
SN1987A-STAR2	83.87	-69.21	(214.02 ± 8.33)E+02	(330.85 ± 5.06)E+02	(500.27 ± 9.84)E+02	(49.52 ± 1.16)E+03	(597.29 ± 6.08)E+02	(507.96 ± 6.48)E+02	(338.42 ± 6.46)E+02
0519-69.0	79.89	-69.04	(109.06 ± 8.71)E+02	(145.05 ± 5.29)E+02	(106.27 ± 9.70)E+02	(111.78 ± 9.95)E+02	(62.67 ± 6.66)E+02	(51.04 ± 5.74)E+02	(5.87 ± 1.06)E+03
0509-67.5	77.38	-67.52	(4.61 ± 1.15)E+03	(30.68 ± 7.00)E+02	(10.78 ± 6.55)E+02	(10.14 ± 6.16)E+02	(9.02 ± 4.95)E+02	(17.05 ± 6.80)E+02	(13.55 ± 7.85)E+03
0505-67.9	76.43	-67.88	(5.34 ± 1.45)E+03	(103.66 ± 8.82)E+02	(43.92 ± 8.48)E+02	(53.49 ± 7.54)E+02	(85.56 ± 6.25)E+02	(83.21 ± 4.93)E+02	(87.30 ± 7.17)E+02
0548-70.4	86.96	-70.41	(4.95 ± 3.00)E+03	(1.49 ± 1.82)E+03	(6.09 ± 3.70)E+02	(10.05 ± 6.11)E+02	(10.58 ± 6.43)E+02	(6.47 ± 3.34)E+02	(9.288 ± 4.70)E+03
N44C-NEBULA	80.69	-67.94	(179.90 ± 7.72)E+02	(229.21 ± 4.69)E+02	(27.30 ± 1.02)E+03	(27.76 ± 1.16)E+03	(28.85 ± 3.99)E+03	(25.61 ± 3.40)E+03	(23.99 ± 3.67)E+03
SK-71D45-BKGD	82.83	-71.04	(14.39 ± 1.19)E+03	(188.98 ± 7.28)E+02	(21.69 ± 1.29)E+03	(22.95 ± 1.38)E+03	(236.98 ± 9.82)E+02	(226.97 ± 9.25)E+02	(20.95 ± 1.11)E+03
SK-71D45-BKGD	82.83	-71.04	(15.33 ± 1.48)E+03	(199.23 ± 9.01)E+02	(20.32 ± 1.37)E+03	(24.53 ± 1.34)E+03	(24.10 ± 1.15)E+03	(226.91 ± 9.27)E+02	(19.44 ± 1.37)E+03
SK-67D166-BKGD	82.97	-67.60	(4.42 ± 1.45)E+03	(95.50 ± 8.84)E+02	(1.97 ± 1.20)E+03	(4.82 ± 2.61)E+03	(24.67 ± 6.69)E+02	(18.28 ± 8.13)E+02	(9.07 ± 1.59)E+03
SK-67D166-BKGD	82.86	-67.65	(10.49 ± 1.76)E+03	(12.65 ± 1.06)E+03	(14.34 ± 1.74)E+03	(15.12 ± 1.69)E+03	(9.87 ± 1.75)E+03	(8.49 ± 1.42)E+03	(14.95 ± 2.11)E+03
SK-67D14-BKGD	73.72	-67.25	(27.77 ± 1.16)E+03	(286.84 ± 7.06)E+02	(255.05 ± 7.73)E+02	(26.98 ± 1.07)E+03	(312.98 ± 8.76)E+02	(290.23 ± 683	(314.42 ± 4.97)E+02
BREY22-BKGD	79.85	-69.33	(12.84 ± 1.14)E+03	(176.75 ± 6.95)E+02	(22.59 ± 1.11)E+03	(24.74 ± 1.11)E+03	(231.83 ± 8.71)E+02	(174.92 ± 9.88)E+02	(205.21 ± 9.57)E+02
SK-67D104-BKGD	81.53	-67.47	(14.00 ± 1.46)E+03	(174.94 ± 8.88)E+02	(18.23 ± 1.62)E+03	(17.52 ± 1.71)E+03	(24.14 ± 1.47)E+03	(22.65 ± 1.16)E+03	(27.38 ± 1.41)E+03
AADOR-BKGD	82.82	-69.88	(11.32 ± 4.98)E+03	(7.39 ± 3.03)E+03	(11.02 ± 1.24)E+03	(103.01 ± 9.53)E+02	(6.99 ± 1.34)E+03	(63.95 ± 8.22)E+02	(8.88 ± 2.49)E+03
AADOR-BKGD	82.91	-69.85	(7.50 ± 1.13)E+03	(109.77 ± 6.91)E+02	(177.56 ± 9.90)E+02	(20.66 ± 1.05)E+03	(13.45 ± 1.05)E+03	(11.01 ± 1.03)E+03	(11.60 ± 1.55)E+03
BKGD	82.87	-67.65	(8.56 ± 2.62)E+03	(12.54 ± 1.59)E+03	(14.24 ± 2.21)E+03	(14.00 ± 2.40)E+03	(7.92 ± 2.85)E+03	(8.96 ± 2.14)E+03	(11.60 ± 2.09)E+03
N49	81.51	-66.09	(104.75 ± 9.24)E+02	(774.29 ± 5.62)E+02	(197.42 ± 5.97)E+02	(220.38 ± 9.18)E+02	(179.84 ± 9.50)E+02	(145.21 ± 7.54)E+02	(30.01 ± 1.03)E+03
SN1987A	83.87	-69.27	(1990.20 ± 9.04)E+02	(2610.30 ± 5.49)E+02	(3131.80 ± 9.46)E+02	(310.93 ± 1.11)E+03	(3170.10 ± 8.94)E+02	(2992.90 ± 9.25)E+02	(2331.50 ± 8.80)E+02
SN1987A	83.87	-69.27	(197.23 ± 1.13)E+03	(2601.90 ± 6.88)E+02	(309.07 ± 1.39)E+03	(310.44 ± 1.49)E+03	(309.97 ± 1.35)E+03	(295.56 ± 1.02)E+03	(2284.90 ± 8.78)E+02
SN1987A	83.87	-69.27	(197.36 ± 1.47)E+03	(2611.90 ± 8.94)E+02	(307.73 ± 1.27)E+03	(312.68 ± 1.86)E+03	(314.02 ± 1.01)E+03	(297.78 ± 1.00)E+03	(228.51 ± 1.21)E+03

Notes: Units of right ascension and declination are in degrees.
This table presents the diffuse surface brightness of 81 diffuse *FUSE* targets and 43 *UIT* diffuse observations. The diffuse surface brightness *FUSE* bands are in units of 10^4 photons cm^{-2} s^{-1} sr^{-1} $Å^{-1}$ and the uncertainties are 1σ error bar. The *UIT* surface brightness in units of 10^4 photons cm^{-2} s^{-1} sr^{-1} $Å^{-1}$ and the error in the data is around 10% (Parker et al. 1998).

Chapter 4

Far Ultraviolet Diffuse Emission from the Small Magellanic Cloud

4.1 Introduction

The SMC is a dwarf irregular galaxy located at a distance of about 60 Kpc (Hilditch et al. 2005) from the MW and 20 Kpc from the LMC. It is present in the southern constellation of Tucana spanning 5° of the sky. This galaxy is the fourth closest galaxy to the MW with center at RA: 00h 52m 44.8s (13.19°) and Dec: -72° 49′ 43″ (-72.83°) (gl = 302.80 and gb = -44.30). The important regions in the SMC are the *SMC bar*, an active star forming region populated by young stars, the *SMC wing* which connects part of the SMC to the Magellanic bridge and is associated with modest star formation, and the *SMC tail* which extends from the wing comprising of the gas and dust (Figure 4.1). The tail of the SMC is the torn off the main body of the Galxy due to gravitational tides. The SMC has a mass of 2.5 $\times 10^9 M_\odot$, and a star formation rate of 0.05 $M_\odot$/yr (Wilke et al. 2003). Henrietta Leavitt discovered the period-luminosity relation of Cepheid variables in the SMC, which is since then used as the most reliable method for determining large cosmic distances.

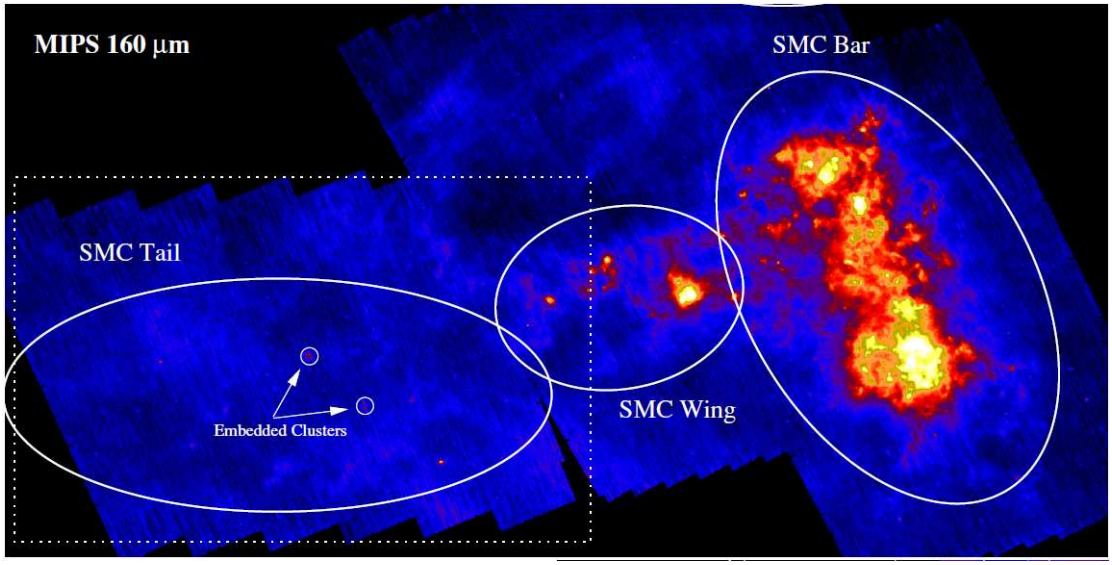

FIGURE 4.1: 160 micron image of the SMC from Gordon et al. (2009) showing different regions of the SMC.

The ISM of the SMC is relatively different from the MW and the LMC because of its low metallicity (Z $\approx$ 0.005; Dufour 1984; Asplund et al. 2004), under-abundance of dust (8 times smaller than the MW; Bouchet et al. 1985) and interstellar UV radiation field 4–10 times higher than that in the solar neighborhood (Vangioni-Flam et al. 1980). Hence, it provides a nice extragalactic astrophysical laboratory like the LMC to probe the gas and dust and the star formation activity. The SMC is oriented nearly face on with a foreground Galactic extinction of 0.02 mag (Hutchings 1982) furnishing an unimpeded view of the small scale structure. The ISM of the SMC is similar to that of high redshift galaxies because of its low metallicity and therefore may be a stepping stone to our understanding of the ISM in them (Witt & Gordon 2000).

Dust in the SMC is quite different from either the MW or the LMC as shown, for instance, by the absence of 2175 Å bump (Gordon et al. 2003). Models of the dust in the SMC typically attribute the absence of the 2175 Å bump to a lack of carbonaceous dust (Weingartner & Draine 2001). Recently several IR studies have been used to explore the dust properties in the SMC. Using high resolution *IRAS* data Stanimirovic et al. (2000) concluded that the diffuse cool dust and gas of the SMC is dominated by large grains with a low value of dust-to-gas ratio and dust mass compare to the MW. Bot et al. (2004) modeled the SEDs of dust to

find the contribution of emission from the dust components; PAHs, VSGs, and BGs. The authors found a substantial 60 μm excess that could be caused by an enhanced interstellar radiation field in the SMC or due a change in the grain size distribution with respect to the Galaxy. *Spitzer* results report the properties of the dust, gas, IR sources, and the abundance of PAHs which is a major component of dust in the ISM of the SMC. Using the *Spitzer* survey, Leroy et al. (2007) studied dust emission in the far-infrared finding an excess of emission which is tracing H_2 gas but no CO in the molecular clouds leading to conclusion that the intense radiation field (UV photons) destroys the CO while H_2 is survived by shelf-shielding (Maloney & Black 1988) in the SMC. From the modelling of the UV absorption and FIR emission data (Weingartner & Draine 2001; Li & Draine 2002; Clayton et al. 2003), it is found that there is a deficit of PAHs and VSGs, and accumulating a dust composition with more silicate and fewer graphite grains to reproduce the observations.

There have been a number of observations of the SMC in the near UV (Nandy & Morgan 1978; Vangioni-Flam et al. 1980; Maucherat-Joubert et al. 1980a; Cornett et al. 1994) who have mapped the surface brightness and integrated magnitudes of the bright regions of the SMC. Here, we present the first observations of diffuse FUV emission from the SMC. These were serendipitous observations made with the *FUSE* and include several different environments in the SMC, from those near hot stars in the bar region to those further out in the edges of the galaxy. The diffuse emission tracks the interaction of the radiation field with the dust and is an important input into models of distant galaxies (da Cunha et al. 2008). The SMC offers an opportunity to test these models at high spatial resolution and to distinguish the different components of the galaxy.

4.2 FUV Diffuse Emission from the SMC

There were a total of 220 observations in and around the SMC but most are of stars through the LWRS aperture leaving 30 pointings from which we could extract the diffuse background. The observational details of these pointings are

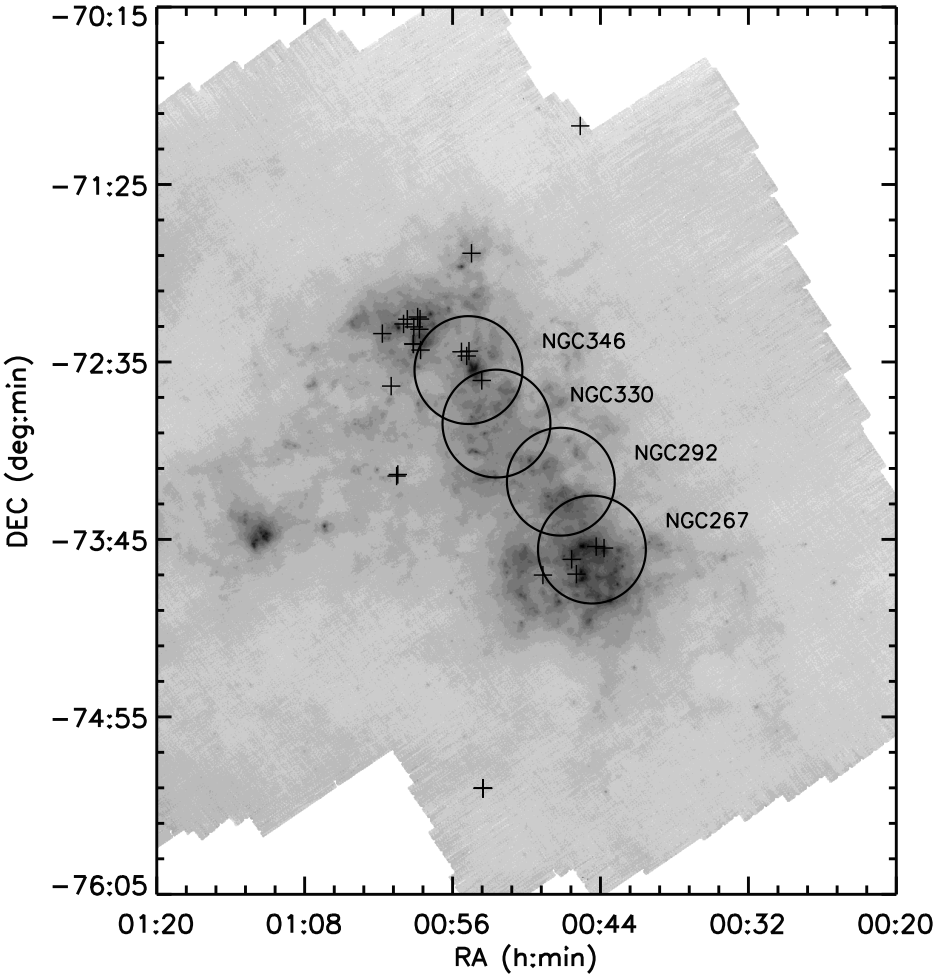

FIGURE 4.2: SMC 160 micron image from Gordon et al. (2009) with the location of *FUSE* observations marked by '+' signs and the *UIT* fields are by circles.

given in Table 4.1. Most of the regions observed are either active areas of star formation or H II regions, such as NGC 346 and NGC 330. The data selection and analysis procedure have been explained in detail by Murthy & Sahnow (2004). The background was subtracted from the data which was then collapsed into two wavelength bands per segment, avoiding airglow lines (Feldman et al. 2001). This resulted in a total of 6 bands from 3 segments. The noise was too high to observe the diffuse background in segment 2B and so we didn't use it. In addition, a few of the data points in the 2A segment were anomalous and were also rejected.

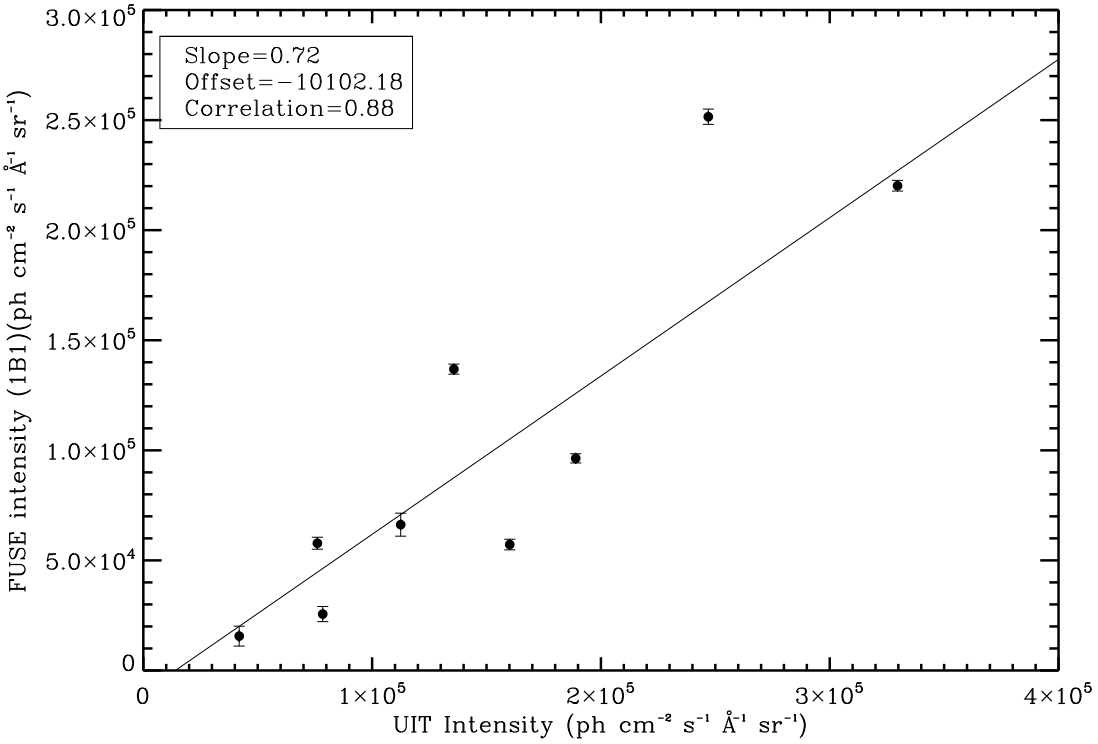

FIGURE 4.3: Correlation between the *FUSE* (1B1) and the *UIT* surface brightness is shown. The correlation coefficient is 0.88. The best fit line is with slope 0.72 and an offset of -10102.18 photons cm^{-2} s^{-1} sr^{-1} Å^{-1}. Errors in the observations are small (relative to Y-axis scale) to be visible and are not shown.

Our target locations are marked with plus sign on an IR 160 micron (Gordon et al. 2009) image of the SMC and the *UIT* fields are represented by circles (Figure 4.2). There is an excellent correlations exist between the *FUSE* bands with the correlation coefficients better than 0.9 in each case. Our observed surface brightnesses (Table 4.1) extracted from the *FUSE* bands (1000 Å– 1150 Å) range from a minimum of 1200 photons cm^{-2} s^{-1} sr^{-1} Å^{-1} to as high as 2.5 × 10^5 photons cm^{-2} s^{-1} sr^{-1} Å^{-1} in NGC 346, the youngest and largest H II region in the SMC. We have estimated the level of Galactic background at these wavelengths from the *Voyager* maps of Murthy et al. (1999) to be about 1000 photons cm^{-2} s^{-1} sr^{-1} Å^{-1}, below the *FUSE* detection limit.

We added observations from the *UIT* (Stecher et al. 1997) to extend our data into the near UV. The *UIT* observed four 37′ diameter fields which encompassed most of the bar of the SMC at 1615 Å (Cornett et al. 1997) with an angular resolution

of 3″ (Figure 4.2). Nine of our *FUSE* targets fell within the area covered by the *UIT* observations and we measured the diffuse *UIT* flux for them by rebinning the 1″.13 *UIT* pixels over the 30″x30″ *FUSE* LWRS aperture. These fluxes are listed in Table 4.1 and are highly correlated (r = 0.88) with the *FUSE* surface brightness as shown in the Figure 4.3.

Most of the FUV diffuse targets are present on the Bar region of the SMC except a bunch of bright FUV diffuse targets (nine targets) that are located in the north-east of the SMC which is a supernovae remnant. Although this region is off the SMC bar, we find this region very bright in UV. This is in close proximity to the N66 which is the largest star forming region in the SMC with numerous O type stars (Massey et al. 1989; Walborn et al. 2000) and also contains some of our bright diffuse targets. It is likely that some part of the diffuse light comes from the stars far away from the observed region where the dust grain is located. This is evident from the calculations of Cole et al. (1999a) and Pradhan et al. (2010) for the LMC where they found that much of the stellar radiation is non-local i.e., the diffuse light is actually the scattered light of distant stars by local dust. The north-east region is bright in IR 160 micron as seen in figure 4.2 showing that adequate amount of dusts are present which scatter the radiation from the OB stars of N66.

4.2.1 Diffuse Fraction

The fraction of the total FUV light emitted as diffuse radiation in the SMC provides important information in context to the regional distribution of dust. *UIT* observations cover the entire SMC bar (Figure 4.2) and Cornett et al. (1997) have provided a catalog of all the UV stars in this region. We measured the total integrated UV emission in the *UIT* images directly by summing the fluxes in pixels. We used the catalog of Cornett et al. (1997) to calculate the total stellar emission in each field at 1615 Å. We extended the stellar emision into the *FUSE* bands using the stellar radiation field model of Sujatha et al. (2004) that is based on Kurucz models (Kurucz 1992) and calculated their emission in *FUSE* bands. We

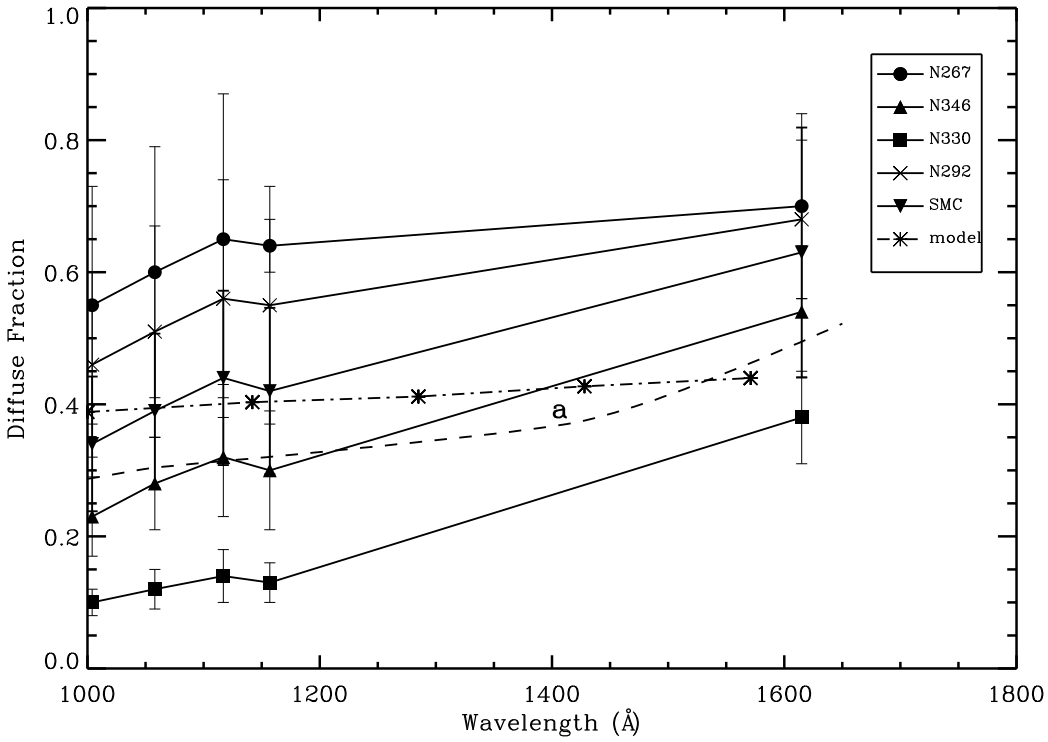

FIGURE 4.4: Variation of diffuse fraction against the wavelength for the *UIT* regions as well as for the SMC bar as a whole. Dust albedo (dashed line) is from the model calculations of Weingartner & Draine (2001). The error bars were empirically calculated by taking the extremes of the observed intensities and range from 20% to 30% of the data. The model calculation of diffuse fraction (dot-dashed line) is from Witt & Gordon (2000).

subtracted the total stellar emission from the integrated aperture emission to obtain the total diffuse emission in each field which is the sum of contributions from faint stars as well as dust scattered emissions. Cornett et al. (1997) predicted that 22% of the diffuse emission is contributed by the stars fainter than UV magnitude 14.5 at 1615 Å. We measured the dust scattered diffuse light by subtracting the faint star contribution. We extrapolated the diffuse emission into the *FUSE* bands using the observed *FUSE*/*UIT* diffuse emission ratio, i.e., the slope of the best fit line (Figure 4.3), obtained separately for each of the *FUSE* bands from their correlation with *UIT* band. We used these to calculate the fraction of diffuse light escaping the SMC, defined as the diffuse emission divided by the total emission (diffuse + stellar), in each region and over the entire SMC bar (Figure 4.4) with an estimated uncertainty of 20% – 30%. In all cases, the behaviour of the diffuse fraction is almost the same, rising by 10% from 1000 Å to 1150 Å and a further

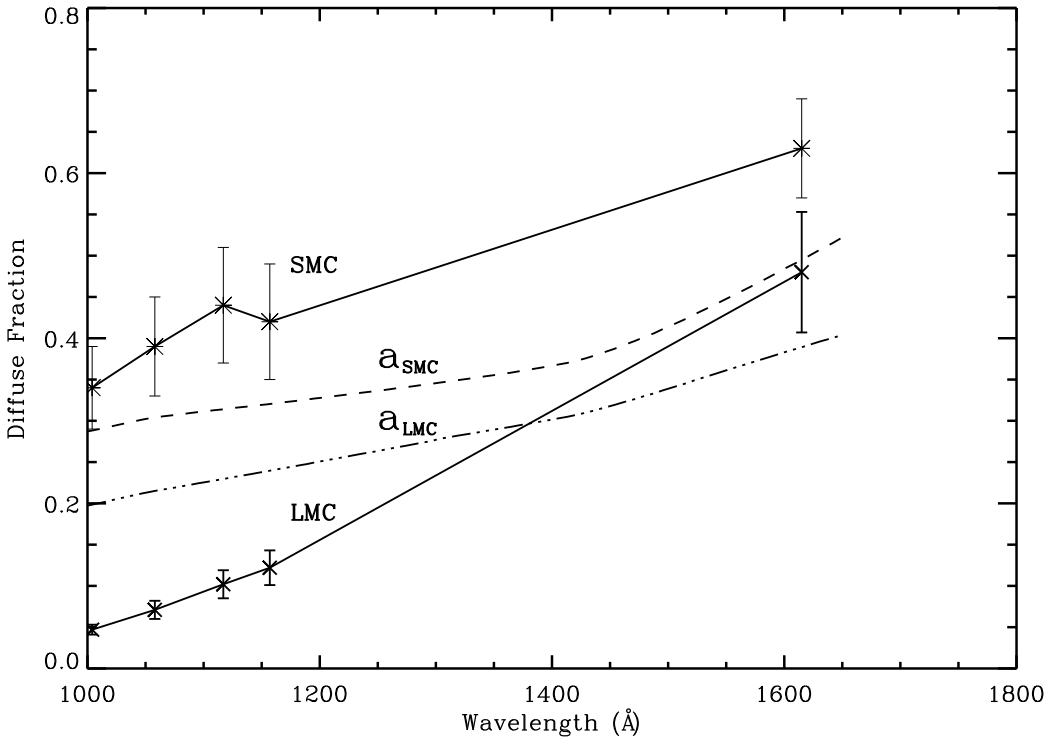

FIGURE 4.5: Comparison of FUV diffuse fraction of the LMC and the SMC. The dashed line represents the albedo of the SMC and the dot-dashed line represents the albedo of the LMC and are obtained from the model calculations of Weingartner & Draine (2001).

50% from 1150 Åto 1615 Å, suggesting that the albedo of the dust increases by about the same factor, in agreement with the theoretical predictions of Weingartner & Draine (2001) for a mix of spherical carbonaceous and silicate grains over the same wavelength range.

Integrating over the entire SMC bar, we find that 34% of the total radiation that escapes the SMC bar at 1000 Å is diffuse rising to 63% in the *UIT* bands at 1615 Å. The scattered light in the SMC has been modelled by Witt & Gordon (2000) using a multiple scattering code for a clumpy shell type dust geometry. The shell geometry has stars extending to 0.3 of the system radius and dust extending from 0.3 to 1 of the syestem radius. They found that the ultraviolet scattered radiation is in the range of 25% to 50% of the total integrated radiation coming from the SMC bar. We have also plotted their modelled FUV scattered fraction along with our observed fraction (Figure 4.4) which is agreeing the approximate observed

value of diffuse fraction computed by us. Considering only H II regions of the SMC, we found that around 20% of the total radiation at 1004Å is diffuse rising to 50% at 1615 Å. Studies for the Orion nebula (Bohlin et al. 1982) and NGC 595 (Malumuth et al. 1996) find similar results with 66% of the total radiation being diffuse at 1400 Å in Orion and 55% at 1700 Å in NGC 595. Pradhan et al. (2010) found significantly smaller values for the diffuse fraction in the LMC (Figure 4.5) perhaps due to the difference in grain size and composition between the two galaxies (Pei 1992; Weingartner & Draine 2001; Gordon et al. 2003). The albedo of the SMC dust is about 50% higher (Weingartner & Draine 2001) compared to the LMC dust (Figure 4.5) and this may explain the increased diffuse fraction in the SMC.

The shape of the FUV diffuse fraction in both the LMC and the SMC are very much similar in the wavelength range of 1000 Åto 1615 Å but show regional variation due to varying composition and distribution of dust as well as the variation 3of the number density of young hot stars. We have examined the variation of the diffuse fraction over different region in the SMC bar finding that it is larger in those areas where there are fewer stars (NGC 267 and NGC 292) suggesting that much of the diffuse radiation from those regions is actually due to distant stars. Similar results were found in the LMC (Pradhan et al. 2010) which show that the diffuse fraction is less in crowded regions such as 30 Doradus, SN 1987A and N11 (4% – 10%) and more in sparse regions such as N70 (24% – 45%). Cole et al. (1999b) modeled the escape fraction of NUV photons for the LMC where they show that much of the stellar light is non-local i.e., the light from the distant OB associations is scattered by local dust.

4.3 Correlation with the Hα Emission

The H II regions are accomplished copious Hα emitters with hot massive stars at the center. The catalog of the H II regions in the SMC was given by Davies et al. (1976) and the integrated Hα emission for them was calculated by Kennicutt & Hodge (1986) defining circular aperture sizes. We have computed the integrated

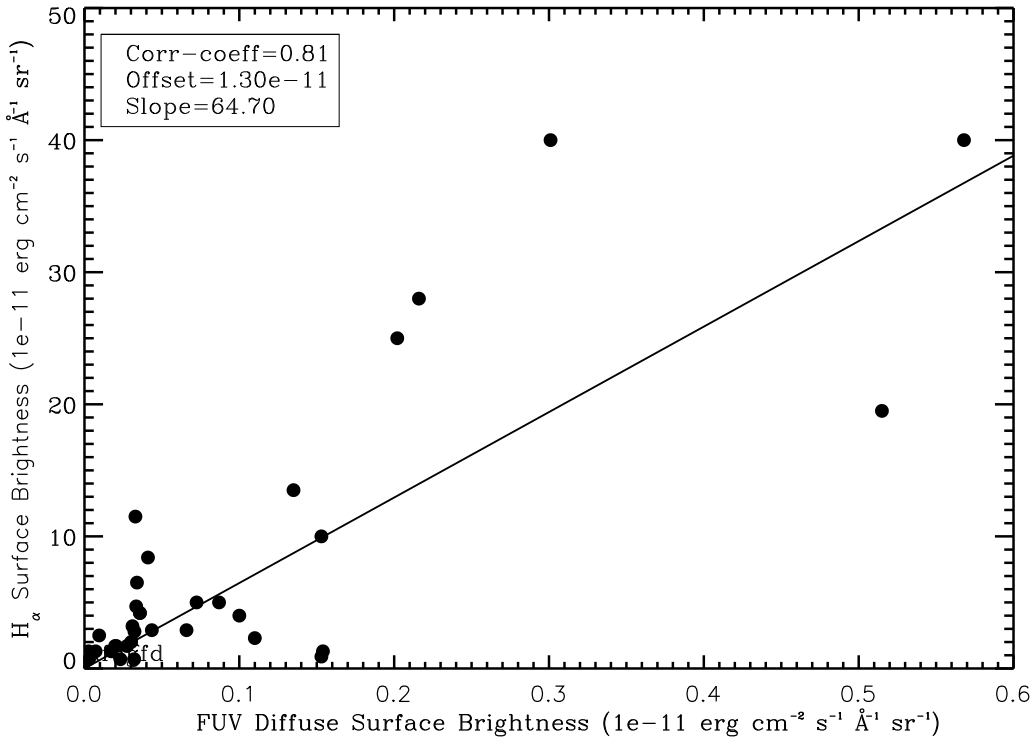

FIGURE 4.6: Plot of the FUV diffuse surface brightness and the Hα flux of the H II regions (Kennicutt & Hodge 1986). The best fit line is with slope 64.70 and an offset of 1.30e-11 ergs cm^{-2} s^{-1} sr^{-1} Å^{-1}. The correlation coefficient is 0.81.

FUV diffuse emission at *FUSE* bands for 36 H II regions those were used by Cornett et al. (1997). We found a good correlation with a correlation coefficient of 0.81 between the integrated diffuse FUV emission and Hα emission from H II regions of the SMC (Figure 4.6). This is as expected given that the Hα emission is proportional to the brightness of the eciting stars as is FUV emission.

4.4 Conclusion

We have presented the first observations of FUV (1000 – 1150 Å) diffuse radiation from the SMC based on observations made with the *FUSE*. These targets are present in various environments of the SMC. The diffuse radiation is primarily due to light from hot stars scattered by the interstellar dust grains and ranges

from around 10^3 photons cm^{-2} s^{-1} sr^{-1} Å^{-1} to as high as 2.5×10^5 photons cm^{-2} s^{-1} sr^{-1} Å^{-1} in the SMC. The FUV diffuse fraction is 34% – 44% in the *FUSE* bands (1000 – 1150 Å) with a further increase upto 63% at 1615 Å. Much less light is scattered in the FUV than at long wavelengths showing that a large percent of the light is absorbed by the dust. The FUV diffuse fraction emitted from the SMC is much higher than the LMC which is attributed to the relatively higher value of albedo of SMC dust compared to the LMC dust and less number of hot stars in the SMC compared to the LMC. The FUV diffuse emission also corellates with the Hα emission in the SMC.

We are now building a more detailed model to use the wealth of data now available in the MCs, particularly the data from *Spitzer* (Meixner et al. 2006). The UV and IR data are complementary in that they probe different aspects of the radiative transfer between stars and the dust with the part of the radiation not scattered in the UV radiated in the IR and an understanding of the absorption and subsequent re-emission of the starlight in a nearby galaxy such as the MCs will provide templates for more distant galaxies where only the convolution of the two is seen.

TABLE 4.1: Details of *FUSE* observations in the SMC.

FUSE ID	RA (LWRS)	Dec(LWRS)	LiF 1A1	LiF 1A2	LiF 1B1	LiF 1B2	UIT
G9310201	00 46 38.40	-73 08 24.0	1.33 ± 0.83	1.43 ± 0.36	1.56 ± 0.45	2.26 ± 0.53	16.02
G9310301	00 47 16.80	-73 08 24.0	0.97 ± 0.40	2.15 ± 0.22	2.56 ± 0.34	3.11 ± 0.38	32.96
G9310401	00 48 26.40	-73 19 12.0	2.78 ± 0.68	4.99 ± 0.29	6.62 ± 0.53	7.13 ± 0.65	24.69
G9310501	00 49 02.40	-73 14 24.0	3.28 ± 0.24	4.90 ± 0.13	5.78 ± 0.27	5.78 ± 0.24	18.90
G9310601	00 51 07.20	-73 21 36.0	9.07 ± 0.22	11.33 ± 0.11	11.09 ± 0.26	10.40 ± 0.28	13.57
F3230101	00 53 07.20	-74 39 00.0	3.87 ± 0.39	0.75 ± 0.63	0.48 ± 0.40	0.32 ± 0.29	4.19
F3230102	00 53 07.20	-74 39 00.0	0.15 ± 0.15	0.10 ± 0.09	0.28 ± 0.20	0.29 ± 0.23	7.84
F3230103	00 53 07.20	-74 39 00.0	0.87 ± 0.57	1.22 ± 0.40	0.94 ± 0.15	1.24 ± 0.15	11.25
F3230104	00 53 07.20	-74 39 00.0	0.12 ± 0.12	0.16 ± 0.11	0.27 ± 0.23	0.25 ± 0.14	7.61
F3230105	00 53 07.20	-74 39 00.0	0.15 ± 0.15	0.46 ± 0.32	0.40 ± 0.27	0.51 ± 0.27	
F3230106	00 53 07.20	-74 39 00.0	0.25 ± 0.15	0.78 ± 0.06	0.64 ± 0.34	0.76 ± 0.23	
D9110901	00 53 57.60	-70 37 48.0	0.22 ± 0.19	0.46 ± 0.41	0.22 ± 0.19	0.46 ± 0.41	
G9310701	00 58 19.20	-72 17 24.0	10.07 ± 0.17	12.81 ± 0.10	13.69 ± 0.23	12.45 ± 0.22	
P2030201	00 59 36.00	-72 07 48.0	17.03 ± 0.24	20.47 ± 0.17	25.15 ± 0.35	23.28 ± 0.36	
C1580101	00 59 43.20	-72 09 36.0	3.50 ± 0.25	4.80 ± 0.13	5.72 ± 0.24	5.81 ± 0.30	
S4057101	01 00 09.60	-72 08 24.0	8.96 ± 0.13	10.69 ± 0.07	9.63 ± 0.21	9.46 ± 0.18	
G9310801	01 00 24.00	-71 33 36.0	5.78 ± 0.24	7.76 ± 0.16	9.35 ± 0.27	7.98 ± 0.34	
G9310901	01 03 16.80	-72 09 36.0	15.90 ± 0.23	20.27 ± 0.12	22.02 ± 0.24	19.86 ± 0.22	
G9311002	01 03 33.60	-72 02 24.0	20.30 ± 0.27	24.25 ± 0.14	25.15 ± 0.22	23.29 ± 0.28	
C0830201	01 03 36.00	-71 58 48.0	14.64 ± 0.39	18.29 ± 0.17	16.64 ± 0.41	18.24 ± 0.41	
G0350101	01 03 48.00	-71 58 12.0	5.31 ± 0.22	6.79 ± 0.12	7.67 ± 0.21	7.48 ± 0.25	
E5110802	01 03 52.80	-72 54 00.0	2.69 ± 0.46	3.77 ± 0.20	4.41 ± 0.40	4.57 ± 0.44	
F3210103	01 03 52.80	-72 07 48.0	17.09 ± 0.12	24.79 ± 0.07	34.14 ± 0.15	33.34 ± 0.14	
F3210104	01 03 52.80	-72 07 48.0	22.18 ± 0.25	33.53 ± 0.11	46.05 ± 0.17	45.32 ± 0.21	
E5110801	01 03 57.60	-72 54 36.0	0.70 ± 0.52	0.86 ± 0.45	0.92 ± 0.40	0.90 ± 0.50	
A0750204	01 04 00.00	-72 01 48.0	24.65 ± 0.30	34.22 ± 0.16	30.03 ± 0.28	28.92 ± 0.27	
C0830302	01 04 33.60	-71 59 24.0	2.97 ± 0.24	3.31 ± 0.17	2.92 ± 0.18	2.78 ± 0.19	
G0350301	01 04 48.00	-72 01 12.0	8.17 ± 0.31	10.21 ± 0.17	9.93 ± 0.26	9.34 ± 0.40	
D9044301	01 05 12.00	-72 23 24.0	0.95 ± 0.17	1.32 ± 0.08	0.55 ± 0.09	0.71 ± 0.12	
D9044401	01 06 19.20	-72 05 24.0	1.85 ± 1.85	0.88 ± 0.27	1.64 ±1.20	0.78 ± 0.57	

Notes. Units of right ascension are hours, minutes, and seconds; units of declination are in degrees, arc minutes and arc seconds. The diffuse surface brightness in the *FUSE* and the *UIT* bands are in units of 10^4 photons cm^{-2} s^{-1} sr^{-1} Å^{-1}.

The *FUSE* uncertainties are 1σ error bar and the error in the *UIT* data is around 10%.

Chapter 5

Survey of OVI in the Large Magellanic Cloud

5.1 Introduction

The ISM of the MW and other galaxies is a complex mix of gas and dust. The processes involved in maintaining the mass, energy, and ionization balance of the ISM are not properly understood. The star and the ISM interact with each other by which the stellar ecosystem is maintained. Stars are formed from the material in the ISM and in turn stars also throw away a lots of mass to the ISM via cataclysmic processes such as stellar winds and supernovae explosions that are accompanied by release of a huge amount of energy which heats the ISM upto 10^6 degrees. This superheated ISM is studied either by X-ray emissions or absorption lines of atoms and ions produced via collisional ionization which fall in the ultraviolet wavelength range of the electromagnetic spectrum. Five times ionized oxygen atom (O VI) is one such ion produced in this environment and is a diagnostic of a temperatures of about 3×10^5 K (Cox 2005). Such temperatures are found at the interface of hot ($T > 10^6$ K) and warm ($T \sim 10^4$ K) ionized gas in the ISM. Thus, O VI absorption lines at 1031.9 Å and 1037.6 Å are crucial diagnostics of the energetic processes of interface environments in the ISM of galaxies. The gas at such temperatures

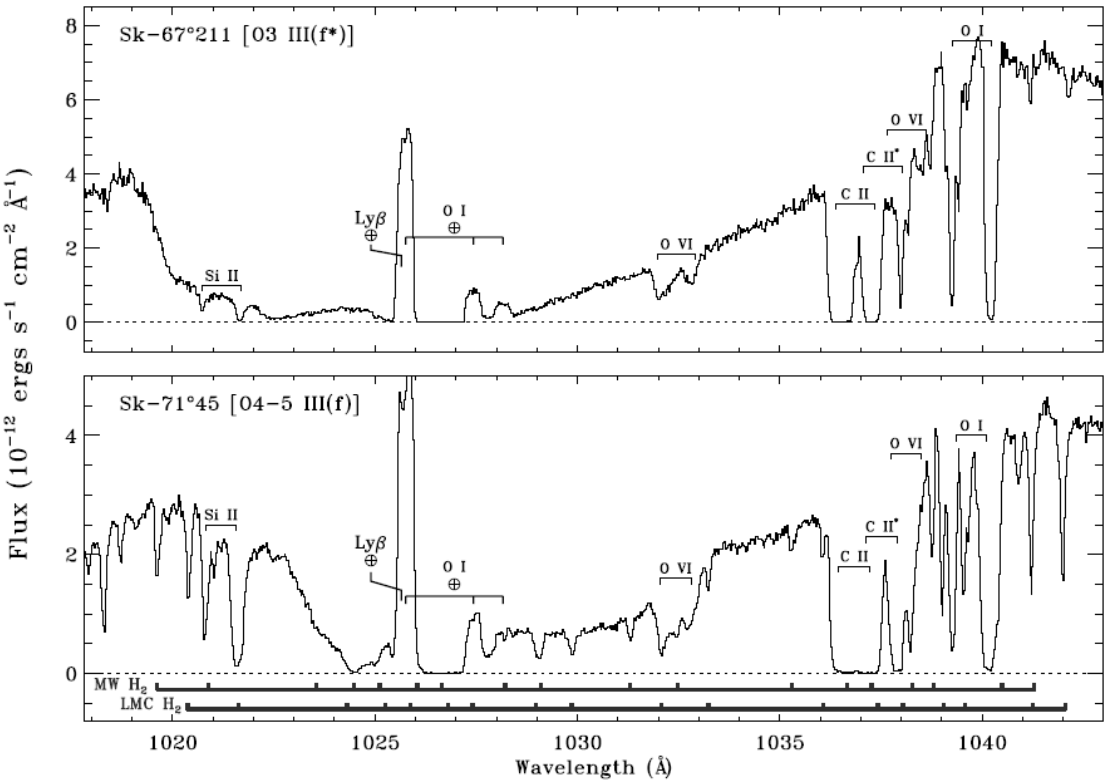

FIGURE 5.1: Sample *FUSE* spectra of two O-type stars showing O VI absorption profiles along with several other ionic species seen in the ISM of both the MW and the LMC and airglow lines. The spectra has been rebinned to ≈ 27 mÅ, or ∼ 7.8 km s^{-1}. Weak molecular hydrogen absorption lines of both the MW and the LMC are shown at the bottom of the spectra (Howk et al. 2002a).

is cooling radiatively which is essentially independent of density, metallicity and the heating mechanism (Edgar & Chevalier 1986; Heckman et al. 2002). O VI formation by photo-ionization is unable to explain the observed abundances, given the energy of photons needed to get such high ionization (114 eV). O VI is mostly produced by shock heating and is collisionally ionized (Indebetouw & Shull 2004).

Previous studies of O VI have been limited to observations by the *Copernicus satellite* (Jenkins 1978a,b) and the *Hopkins Ultraviolet Telescope* (Dixon et al. 1996). Shelton & Cox (1994) concluded that the hot gas exists in discrete regions rather than being continuously present in the ISM. The launch of *FUSE* enabled a wider and more descriptive study of O VI absorption and emission in the ISM and the intergalactic medium (IGM). With a spectral resolution of ≈ 20,000, *FUSE* has been able to resolve fine details of O VI in many different environments. It observed O VI absorption lines in the local ISM of the MW (Savage et al. 2000;

Wakker et al. 2003; Oegerle et al. 2005; Savage & Lehner 2006; Welsh & Lallement 2008), disk of the MW (Bowen et al. 2008), halo of the MW (Savage et al. 2003), the LMC (Howk et al. 2002a; Lehner & Howk 2007), the SMC (Hoopes et al. 2002), starburst galaxies (Grimes et al. 2009), IGM (Danforth & Shull 2005; Danforth et al. 2006), etc. Apart from absorption studies, *FUSE* has also recorded O VI spectra in emission from observations of diffuse ISM in the MW (Shelton et al. 2001; Shelton 2002; Dixon et al. 2006; Dixon & Sankrit 2008) and superbubbles in the LMC (Sankrit & Dixon 2007). These studies not only augmented our knowledge about the formation and distribution of O VI in the MW and the MCs but also helped in the understanding of the complexities of the ISM.

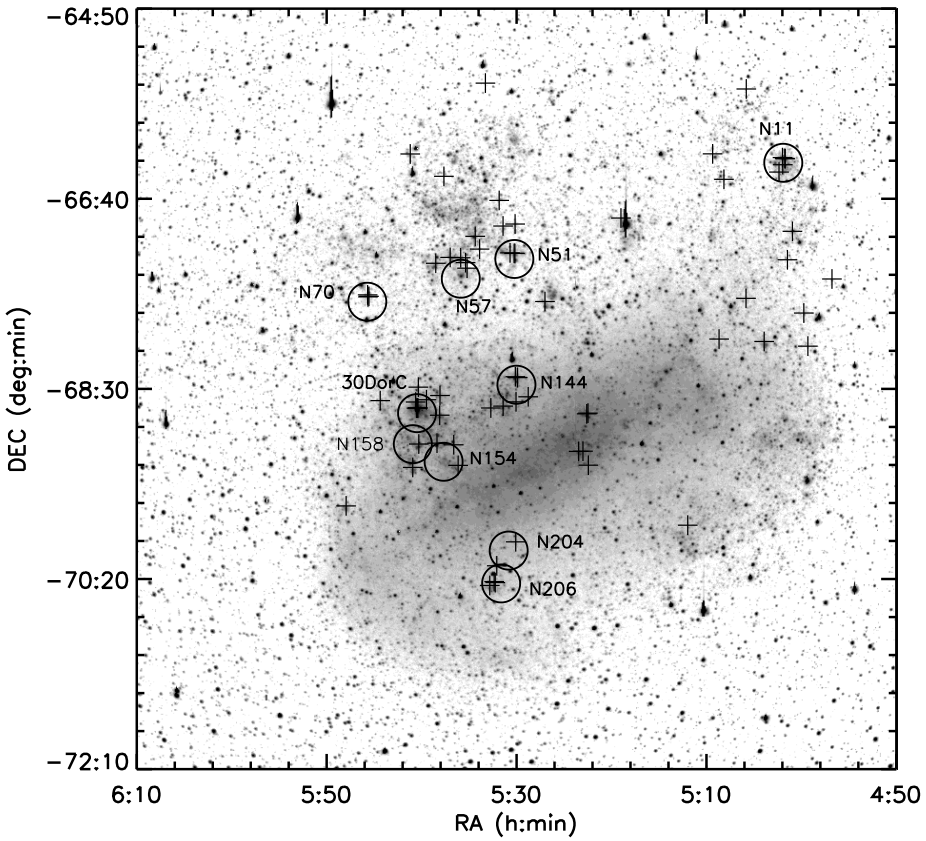

FIGURE 5.2: This is an R-band image of the LMC from Bothun & Thompson (1988) showing the 70 *FUSE* targets ('+' sign) towards which O VI absorption have been studied. Superbubbles are represented by circles with names aside.

Howk et al. (2002a) surveyed the distribution and kinematics of O VI towards 12 early type stars in the LMC, which was very selective and the targets were

restricted to Wolf-Rayet stars and O-type stars of spectral types O7 and earlier. Figure 5.1 shows sample *FUSE* spectra of two O-type stars with target names SK-67D211 and SK-71D45 respectively observed by Howk et al. (2002a). The O VI doublet transitions at 1031.9 Å and 1037.6 Å are marked on the spectra along with several other ionic absorption lines of both the MW and the LMC. The weaker absorption of the O VI doublet at 1037.6 Å is found to be inseparable from the C II* and H_2 absorption. The expected positions of the H_2 lines for $\lambda \geq 1018$ Å and J ≤ 4 for both the LMC and the MW are marked under the spectrum. The (6-0)P(3) and R(4) transitions of H_2 at rest wavelengths of 1031.19 and 1032.35 respectively can contaminate the O VI absorption at 1031.9 Å. We report an extensive survey of O VI absorption at 1032 Å in the LMC. The observation log is given in Table 5.1. The results presented in this survey become important as they not only provide a detailed mapping of the interface gas traced by O VI but also throw light on the small scale structure of the O VI distribution in various regions of the LMC. Figure 5.2 shows the lines of sight and different regions of the LMC including the superbubbles (marked by circles) that have been studied in this survey.

5.2 Observations and Data analysis

5.2.1 *FUSE* Data Analysis and Possible Contamination

The *FUSE* intrument is discussed in chapter 2 of this thesis. Depending on the coating of the spectrograph, observations are possible through SiC and LiF channels that are further divided into eight different segments; the SiC 1A, SiC 2A, SiC 1B and SiC 2B segments covering the wavelength range 905Å to 1105 Å and LiF 1A, LiF 2A, LiF 1B and LiF 2B segments covering the wavelength range 1000Å to 1187 Å. The data from SiC 2B segment have been known to suffer from a fixed noise. The sensitivity of LiF 1A segment near 1032 Å is almost double that of other segments and therefore, we have used only the LiF 1A observations (Sahnow et al. 2000). Most of the observations are from the LWRS with a few from the MDRS aperture.

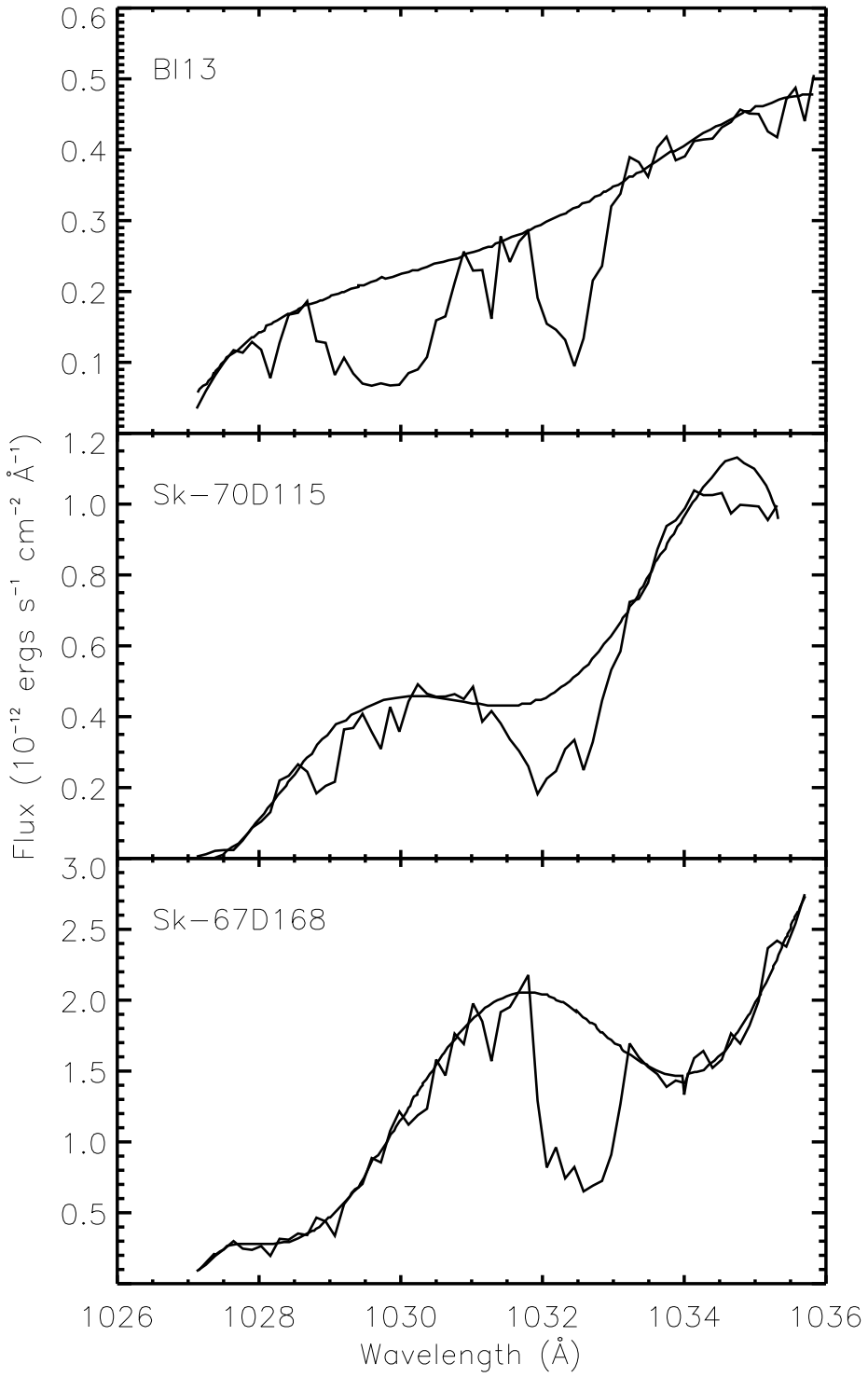

FIGURE 5.3: Examples of three sight lines showing the complexity of continuum fitting in the region near O VI absorption at 1031.92 Å. The top to bottom panels show the increasing complexity of fitting the stellar continuum.

The fully calibrated *FUSE* spectra were downloaded from the Multimission Archive at STScI (MAST) processed by the latest *FUSE* data reduction pipeline (CALFUSE version 3.2; Dixon et al. 2007). It made more than 600 pointings in and around the LMC. Several of the observations were rejected initially due to either non-existent or low signal-to-noise of O VI absorption profile in the spectra. 70 unique *FUSE* targets were selected based mainly on the simplicity of the continuum fitting in the vicinity of O VI (λ = 1031.9 Å). Of the 70 targets, O VI absorption for 1 of the sightline has been reported by Friedman et al. (2000), 11 have been covered by Howk et al. (2002a) survey, 3 by Danforth & Blair (2006a) and 1 by Lehner & Howk (2007). Spectral types and other stellar information was taken from Danforth et al. (2002) and Blair et al. (2009). We have downgraded all the spectra reported here to 35 km s^{-1} to have a higher signal-to-noise. This has been done for all the spectra irrespective of the quality to maintain uniformity in the data analysis procedure.

Fitting of the stellar continuum in the neighbourhood of the O VI absorption profile has been discussed in detail by Friedman et al. (2000) and Howk et al. (2002a). Howk et al. (2002a) have limited their study to early type stars based on the fact that these stars have completely developed O VI P Cygni profiles that are easier to fit as the early type stars have a high mass loss rate and have minimal wind variations. Lehner et al. (2001, 2003) have shown that for Galactic sight lines, the stellar wind variability has negligible effect on O VI absorption but may introduce substantial errors towards targets in the MCs. Lehner et al. (2001) did find variation in the equivalent width and column density towards a LMC star when estimated at two different times. This warrants for extra care while fitting the continuum for MCs targets. As discussed above, for the LMC, the estimation of stellar continuum in the vicinity of O VI absorption is not trivial. Our background targets are mostly early O and B type stars with several Wolf-Rayets. These have been selected based on the fact that the continuum near the O VI absorption at 1031.9 Å is simple to fit. A few of the lines of sight do show a complex behaviour near O VI absorption (for e.g., Sk-67D05, Sk-67D168, Sk-70D115, etc.). For such exceptional lines of sight, the complexity in the continuum fitting is due to a local dip or a sudden rise near the O VI absorption and these targets needed a comparatively higher order polynomial for the fitting. For a flavor of the complexity involved, sample continuum fitting for three lines of sight, BI13,

Sk-70D115 and Sk-67D168 are shown in Figure 5.3. Following the fitting procedure of Howk et al. (2002a) and Sembach & Savage (1992), the local stellar continuum was estimated for all the targets and were fitted by a Legendre polynomial fit of low order (≤ 5). Several continua were tested and the uncertainties involved for the complete data set were used in the measurement of the O VI column densities. The normalized spectra in the vicinity of O VI absorption are presented in Figure 5.10 (at the bottom of this chapter).

The O VI absorption may be contaminated by absorption from molecular hydrogen, however, it is minimal in the LMC velocity range. This is because the molecular fraction of H_2 in the LMC is only about 12% of the molecular fraction in the Galactic disk (Tumlinson et al. 2002). The closest absorption line of H_2 to O VI absorption in the LMC lies at 1032.35 Å (at $v_{lsr} \sim +123$ km s^{-1}), which is due to (6–0) R(4) transition. An estimation of possible contamination by H_2 towards 12 lines of sight in the LMC has been done by Howk et al. (2002a) where they find that H_2 absorption does not affect the LMC O VI column densities significantly. The H_2 absorption feature are usually not a problem for measurements of O VI absorption at velocities more than 20 km s^{-1} apart (Savage et al. 2003, and reference therein). We estimate the contamination from H_2 lines by fitting the (6–0) P(3) H_2 transition for the MW and (6–0) R(4) H_2 transition for the LMC (Figure 5.4). From this, we are able to estimate the contamination due to (6–0) R(4) MW H_2 line and (6–0) P(3) LMC H_2 line. Noticeable contamination is seen for the sightlines Sk-71D45 and Sk-67D250 which is well within the error bar of the derived column densities. An example of a sightline is also shown in Figure 5.4 in which the LMC O VI absorption is free from any contamination from molecular hydrogen. Owing to the negligible contribution, we have not excluded the contamination by H_2 in the O VI measurements for the LMC.

Another possible contaminant is the (6–0) R(0) transition of the HD molecule at 1031.91 Å that overlaps with the MW O VI absorption. Several lines of HD molecule is covered by *FUSE* and the complete list is given by Sembach (1999). H_2 column densities are significantly low in the LMC and contamination due to molecular hydrogen lines is non-significant for O VI measurements in the LMC.

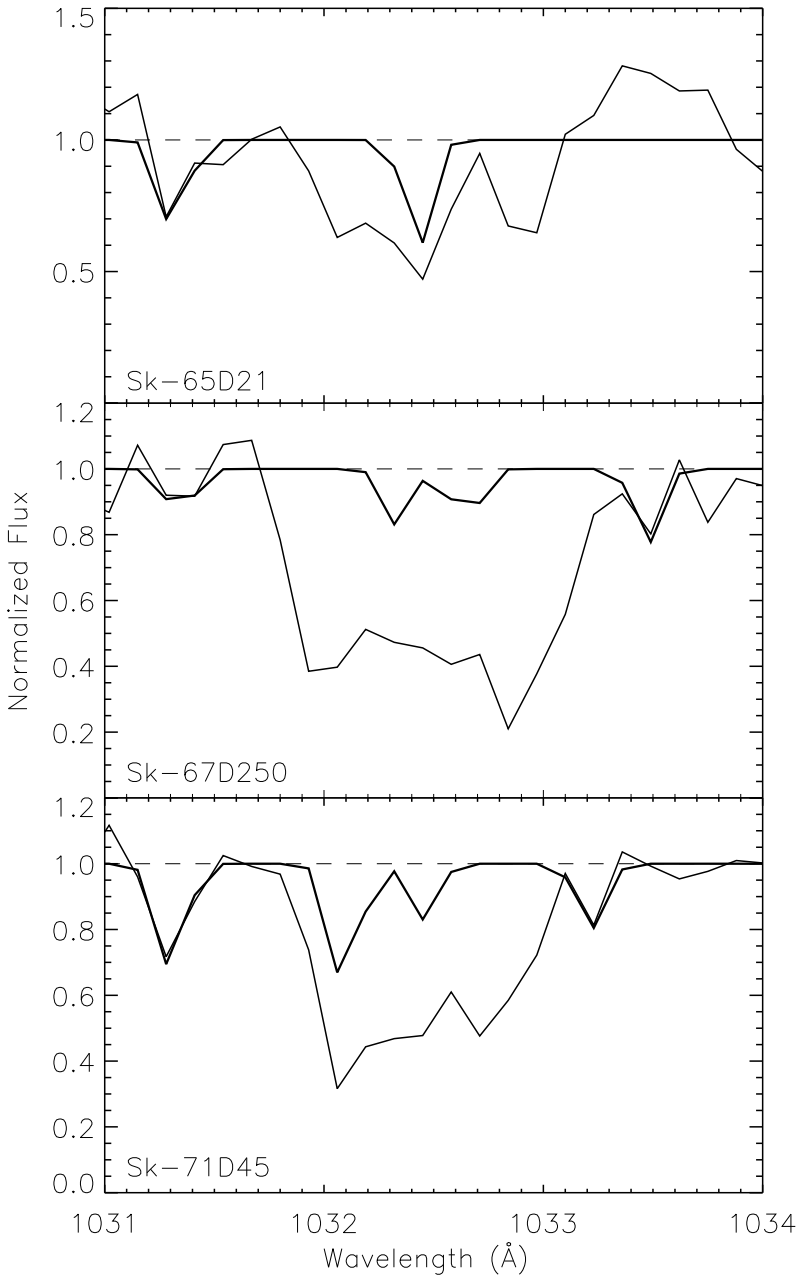

FIGURE 5.4: Model for H_2 absorption overplotted on the normalized O VI absorption profiles for 3 lines of sight. H_2 absorption does not contaminate the LMC O VI absorption for Sk-65D21, shows a maximum contamination for Sk-71D45 and a moderate contamination for Sk-67D250.

Absorption due to HD is about 4 orders weaker compared to H_2 transitions. Therefore, we neglect any contribution from HD molecule to the column densities of O VI in the LMC.

5.2.2 Measurement of O VI Column Densities

The measurement of equivalent widths and column densities of O VI absorption for all the lines of sight were done following Savage & Sembach (1991); Sembach & Savage (1992); Howk et al. (2002a). This apparent optical depth technique (Savage & Sembach 1991) is now commonly used in the analysis of interstellar absorption lines and is applicable to cases with non-saturated absorption profiles. Briefly the technique uses an apparent optical depth in terms of velocity, i.e., an instrumentally blurred version of the true optical depth, given as

$$\tau_a(v) = ln[I_o(v)/I_{obs}(v)], \tag{5.1}$$

where I_o is the estimated continuum intensity and I_{obs} is the intensity of the absorption line as a function of velocity. If the resolution of the instrument is very high compared to the FWHM of the absorption line, the apparent optical depth is a very good representation of the true optical depth. The apparent column density ($N_a(v)$ in atoms cm^{-2} (km s^{-1})$^{-1}$) is calculated by the following relation

$$N_a(v) = \frac{m_e c \tau_a(v)}{\pi e^2 f \lambda} = 3.768 \times 10^{14} \frac{\tau_a(v)}{f\lambda}, \tag{5.2}$$

where λ is the wavelength (Å) and f is the oscillator strength of the atomic species (for O VI, f value of 0.1325 has been adopted from Yan et al. 1998). Similar to Howk et al. (2002a), we find that the 1032 Å O VI profile is broad and is fully resolved by *FUSE*. However, the weaker absorption of the O VI doublet at 1037.6 Å is found to be inseparable from the C II* and H_2 absorption.

The details of the apparent optical depth measurements are listed in Table 5.2. The overlap of the O VI absorption of the MW and the LMC does not allow a precise measurement of column densities for the LMC. For the lines of sight

(Sk-65D21, Sk-67D69, Sk-67D105, HV2543, Sk-66D100, HV5936, Sk-67D211, Sk-69D220, Sk-66D172, Sk-68D137, D301-1005, and D301-NW8) where the LMC O VI is distinct from the MW O VI, the limits of velocities over which integration was performed were easy to obtain. Taking cue from these lines of sight, we estimate the lower velocity limit for the lines of sight where the LMC O VI was not separated from the MW O VI. The errors in the equivalent widths and column densities are 1σ uncertainties derived using the uncertainty in the *FUSE* data and the fitting procedures. The principal contributor to these errors is the ambiguity in the continuum fitting of several of the spectra.

5.3 Distribution and Properties of O VI in the LMC

5.3.1 Abundance and Linewidth of O VI

The LMC spectra were selected based on the quality of the spectra around O VI spectral feature. The survey presented here has more-or-less complete coverage of the well known regions of the LMC such as 30 Doradus, N11, LMC 4, etc., and thus, is very useful in studying the variation of O VI at small scales as well. We find a significant amount of variation in the O VI column densities in a single region and in different regions of the LMC.

Our data covers a wide range of targets; O type stars, B type stars, Wolf-Rayet objects, supernova remnants (SNR), etc. The complete list of the background targets is provided in Table 5.1. These observations give fine details of the small scale structure of O VI column density in the LMC probing to a scale of $\sim$ 10 pc in some regions. We find the O VI absorption in the LMC to be very patchy as is true for the MW. The O VI column density varies from the lowest value of 5.28 $\times 10^{13}$ atoms cm^{-2} near a H II region (DEM 7) to the highest value of 3.74 $\times 10^{14}$ atoms cm^{-2} just north of the LMC bar. Howk et al. (2002a) report the distribution of O VI in the LMC to be patchy as well with the log N(O VI) value

in the LMC varying from 13.9 to 14.6 atoms cm^{-2} and a mean of 14.37 atoms cm^{-2}. Their data did not provide any small scale variation in the column density of O VI with the smallest scale probed is about 450–500 pc.

Given the coverage of our data, we have studied the variation in O VI absorption in different regions of the LMC. We find that the 30 Doradus and SN 1987 A regions dominate in terms of the abundance of O VI. The mean and median values of log N(O VI) for targets in and around 30 Doradus and SNR 1987A are 14.30 and 14.27 atoms cm^{-2} respectively. 30 Doradus is the largest H II region of LMC with a dense concentration of early type massive stars and has thus, attracted extensive research in different wavelength bands (Walborn et al. 1992; Parker 1993; Malumuth & Heap 1994; Walborn & Blades 1997; Townsley et al. 2006; Indebetouw et al. 2009). We discuss in detail about the O VI distribution and its properties in 30 Doradus region in section 5.5. N11 region, which is associated with several OB associations and has a superbubble at its center, shows a high value of O VI column density. The mean of log N(O VI) in the N11 region is 14.21 atoms cm^{-2}.

Another interesting region is the LMC 4 Supergiant shell that includes the Shapley Constellation III, which is one of the largest region associated with star formation (Dopita et al. 1985; Dolphin & Hunter 1998). The log N(O VI) value in LMC 4 supershell varies from a minimum of 13.86 atoms cm^{-2} to a maximum of 14.45 atoms cm^{-2} with a mean value of 14.20 atoms cm^{-2} and a median value of 14.25 atoms cm^{-2}. Other regions of the LMC also show patchiness in the O VI distribution. Statistically, the mean of the O VI column density in the LMC is 1.88 $\times 10^{14}$ atoms cm^{-2} which is lower than 2.34 $\times 10^{14}$ atoms cm^{-2} given by Howk et al. (2002a) for 12 lines of sight. The difference is most likely due to the wide coverage of background targets in our data. The median value of the O VI column density is 1.66 $\times 10^{14}$ atoms cm^{-2} which also is less than the value reported by Howk et al. (2002a). Overall we find that there is an ubiquitous presence of O VI throughout the LMC.

The kinematics of O VI in the LMC is difficult to study because of the ambiguity in separating the LMC O VI absorption from the MW absorption. For some of

the *FUSE* targets, i.e., for Sk-65D21, Sk-67D69, Sk-67D105, HV2543, Sk-66D100, HV5936, Sk-67D211, Sk-69D220, Sk-66D172, Sk-68D137, D301-1005, and D301-NW8, O VI absorption at LMC velocities are distinct from the MW (Figure 5.10). Linewidth for the LMC O VI profiles are obtained with relatively less error for these lines of sight. The LMC O VI absorption profiles have all been fitted with a single Gaussian. The corresponding FWHM for these lines of sight are 55, 85, 78, 90, 90, 113, 100, 85, 105, 94, 107, and 91 km s^{-1} respectively. The temperature range estimated from these widths is T $\sim 1 \times 10^6 - 5 \times 10^6$ K. O VI abundance is maximum at a temperature of 3×10^5 K, thus, higher FWHM of these profiles is probably due to other broadening mechanisms such as more than one velocity component and/or collision and turbulence. This also represents the kinematic flow structure of O VI in the LMC.

The linewidth for the MW O VI profiles are narrower than the LMC profiles (Savage et al. 2003; Oegerle et al. 2005; Savage & Lehner 2006). For the Galactic halo, Savage et al. (2003) report a range for σ (linewidth) from 16 to 65 km s^{-1} (corresponding FWHM range is 38–153 km s^{-1}). Oegerle et al. (2005), for the local ISM, report average σ to be 16 km s^{-1} (FWHM = 38 km s^{-1}) while Savage & Lehner (2006) report σ values ranging from 15 km s^{-1} to 36 km s^{-1} (FWHM ranging from 35 km s^{-1} to 85 km s^{-1}). The linewidth of the SMC O VI absorption profile are comparable to that of the LMC. The FWHM range for the SMC O VI absorption is from 82 to 115 km s^{-1} with a mean of 94 km s^{-1} (Hoopes et al. 2002). We obtained a mean FWHM value of 91 km s^{-1} for the LMC selected lines of sight. Howk et al. (2002a) have compared O VI absorption profiles of the LMC with Fe II absorption and find that the Fe II profiles are much narrower suggesting that the thermal broadening effect for O VI absorption is much more significant.

5.3.2 Comparison with the MW and the SMC

The MW and the SMC offer a different ISM environment compared to the LMC especially due to the difference in the metallicity. The absorption profiles of the MW O VI are different from the LMC O VI and sometimes these profiles are difficult to separate in an unambiguous manner, thus, a comparison of the kinematics

is not possible. Howk et al. (2002a) have compared the O VI absorption with Fe II absorption at 1125.45 Å. While, the Fe II profiles for the MW and the LMC are clearly separated from each other, the O VI absorption suffers an overlap. This is due to the difference in width of the two absorption. The overlap of the MW O VI absorption profile with the LMC O VI absorption constrained Howk et al. (2002a) to arrive at a definite conclusion about the existence of outflows from the LMC. Following the discussion about the distribution of O VI in the LMC in the previous section, we have presented an overview of O VI in the MW and the SMC.

O VI in the MW has been extensively studied since the launch of *FUSE* (Savage et al. 2000; Howk et al. 2002b; Wakker et al. 2003; Savage et al. 2003; Oegerle et al. 2005; Savage & Lehner 2006; Bowen et al. 2008). Savage et al. (2000) were the first to study the O VI absorption in the disk and halo of the MW as seen towards 11 extragalactic objects (active galactic nuclei) using *FUSE*, confirming the large scale presence of hot gas in the halo (Spitzer 1956). The authors find that log $N_{\perp}$(O VI) varies from 13.80 to 14.64 atoms cm^{-2} and the distribution of O VI is quite patchy. To compare with the projected O VI column density on the plane of the MW, we calculated the projection of O VI column on to the plane of the LMC. Taking the inclination angle of the LMC to be 33°, we find the mean value of log $N_{\perp}$(O VI) $\equiv$ log N(O VI) cos θ = 14.16 atoms cm^{-2}. Savage et al. (2000) quote a mean value of 14.29 atoms cm^{-2} for their sample. The median value of our sample is 14.14 atoms cm^{-2}, while for the Savage et al. (2000) sample, it is 14.21 atoms cm^{-2}.

Savage et al. (2003) report *FUSE* observations of O VI absorption towards 100 extragalactic lines of sight to study the properties and distribution of O VI in the galactic halo. The average log N (O VI) for the complete sample is 14.36 atoms cm^{-2} while log N (O VI) sin $|b|$ value for the complete sample is 14.21 atoms cm^{-2}. The results reveal that there are substantial differences in the values of log N(O VI) and log N(O VI) sin$|b|$ in the northern Galactic hemisphere compared to the southern Galactic hemisphere. The patchiness in the distribution of O VI absorption is found to be similar over angular scales extending from $\leq 1°$ to 180°. An extensive survey of O VI in the MW disk has been reported by Bowen et al. (2008) in which the authors have studied O VI column density towards 148 early

type stars. The correlation between O VI column density and effective distance to a star establishes the fact that the O VI is interstellar in nature and points to the universal presence of the interstellar phenomena that gives rise to O VI throughout the Galaxy.

Hoopes et al. (2002) have surveyed O VI absorption towards 18 early type stars in the SMC and report a widespread presence of O VI. The mean value of log N(O VI) in the SMC is 14.53, which is higher than the LMC and the MW values. The O VI column density in the SMC correlates with the distance from NGC 346, a star forming region that shows the highest abundance of O VI in the SMC.

5.3.3 Comparison with X-ray and Hα

The LMC has been the focus of H_α and X-ray surveys to search for ionized structures in the ISM. H_α surveys have revealed the presence of H II regions, supernova remnants, and large scale structures including superbubbles and super-shells (Davies et al. 1976), whereas, X-ray observations have studied bright X-ray sources (Trumper et al. 1991), the hot gas in the ISM (Wang et al. 1989, 1991) and diffuse X-ray emission (Bomans et al. 1994). Since O VI traces the ISM gas with temperatures $\sim 10^5$K, which is at the interface between hot gas (T $\geq 10^6$K) traced by X-rays and warm gas (T $\sim 10^4$K) traced by H_α, correlation between O VI abundance and X-ray and H_α emissions is expected.

The O VI observations cover specific regions of the LMC with varying environmental conditions. To get an idea about the variation of O VI column densities with different environments in the LMC, we have overlaid O VI column densities as circles on H_α image (Gaustad et al. 2001, Figure 5.5). The diameter of the circle is linearly proportional to log N(O VI). Interestingly, it is noted that O VI abundance is high in regions with low H_α and X-ray emissions, i.e., regions that are relatively inactive. However, regions like superbubbles are O VI rich, for e.g., 30 Doradus C and N11. The gross picture suggests that O VI does not correlate with either H_α or X-ray emissions. We have plotted log N(O VI) against log relative H_α and X-ray surface brightnesses to have a better insight. The X-ray surface

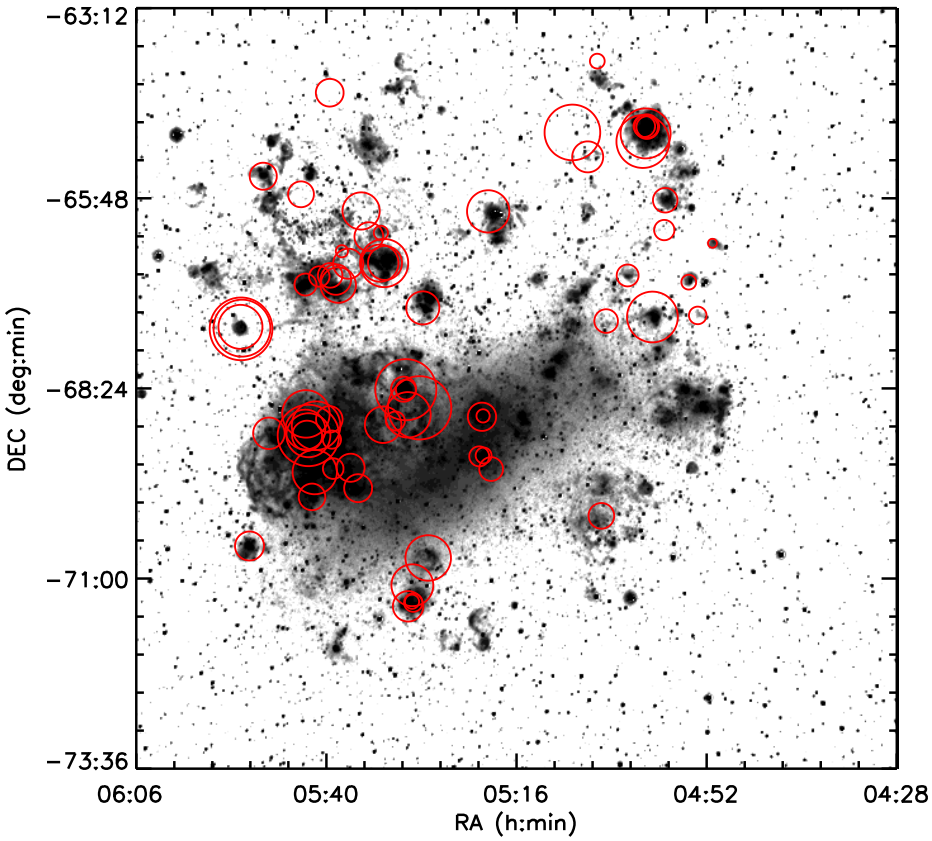

FIGURE 5.5: This is H_α image of the LMC from Gaustad et al. (2001) with circles showing O VI absorption around the 70 targets. The diameter of the circle is linearly proportional to the column density of O VI at LMC velocities.

brightness is obtained from *ROSAT* PSPC mosaic image of the LMC covering the energy range 0.52.0 keV (Snowden & Petre 1994). Figure 5.6 and Figure 5.7 show the correlation of log N(O VI) with H_α and X-ray surface brightnesses for the LMC barring five lines of sight in the X-ray correlation plot. Four of the excluded lines of sight (Sk-67D250, D301-1005, D301-NW8 and Sk-65D63) are not covered by the X-ray observations and one (Sk-69D257) has extremely high X-ray emission (about 2 orders of magnitude higher than other lines of sight). The H_α and X-ray surface brightness are measured by rebinning the corresponding images to match the *FUSE* LWRS and MDRS aperture size. The lack of correlation is evident in both plots as it is found by Howk et al. (2002a). Since, H_α traces warm ISM and star formation, there seems to be no direct relation between O VI formation and these processes. A better correlation with X-ray is expected as the hot gas traced

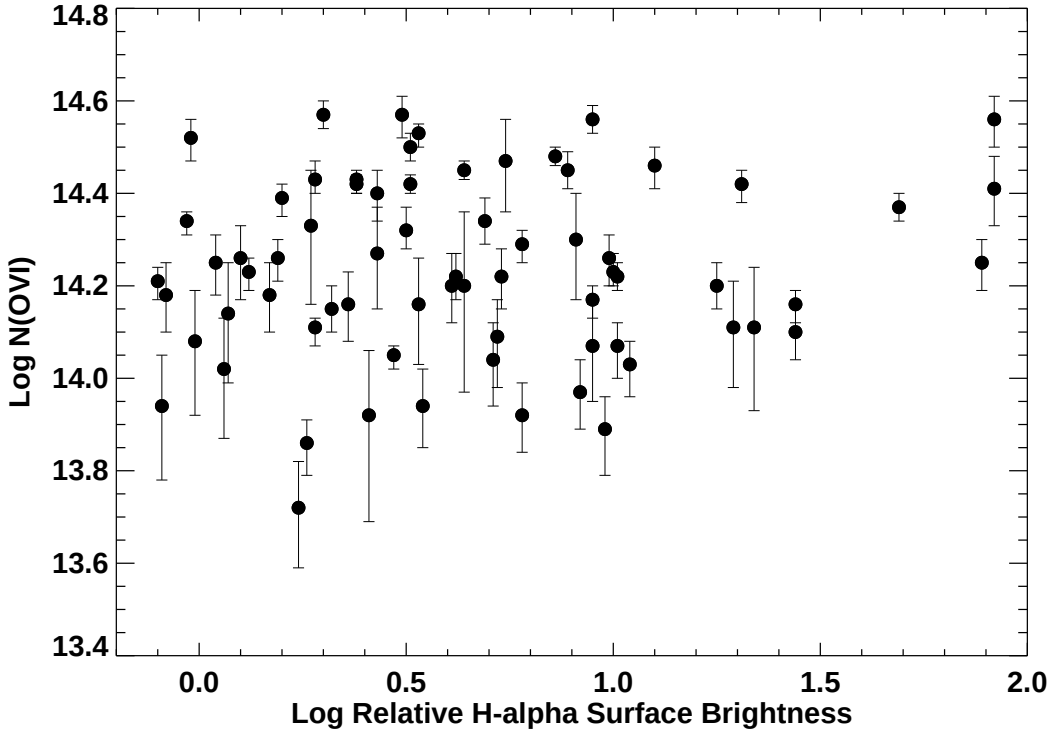

FIGURE 5.6: log N(O VI)) vs. log relative H_α surface brightness for all the 70 *FUSE* targets. H_α surface brightness is from Gaustad et al. (2001).

by X-ray is presumed to cool through temperatures where O VI formation takes place. There is a high abundance of O VI in supernova remnants and superbubbles of the LMC, whereas, bright X-ray emission is observed mostly from the supernova remnants of the LMC. X-ray emission associated with supernova remnants in the LMC is a factor of 2 to 3 times greater than the X-ray emission associated with supergiant shells and the Bar in the LMC (Points et al. 2001).

5.4 O VI in superbubbles of the LMC

Superbubbles may be formed due to the strong stellar wind from young stars and/or supernova explosions forming a local cavity in the surrounding ISM. These are excellent examples of the interaction of young hot stars and the ISM. Superbubbles contain hot gas ($\sim 10^6 K$) that is heated by shocks created by stellar

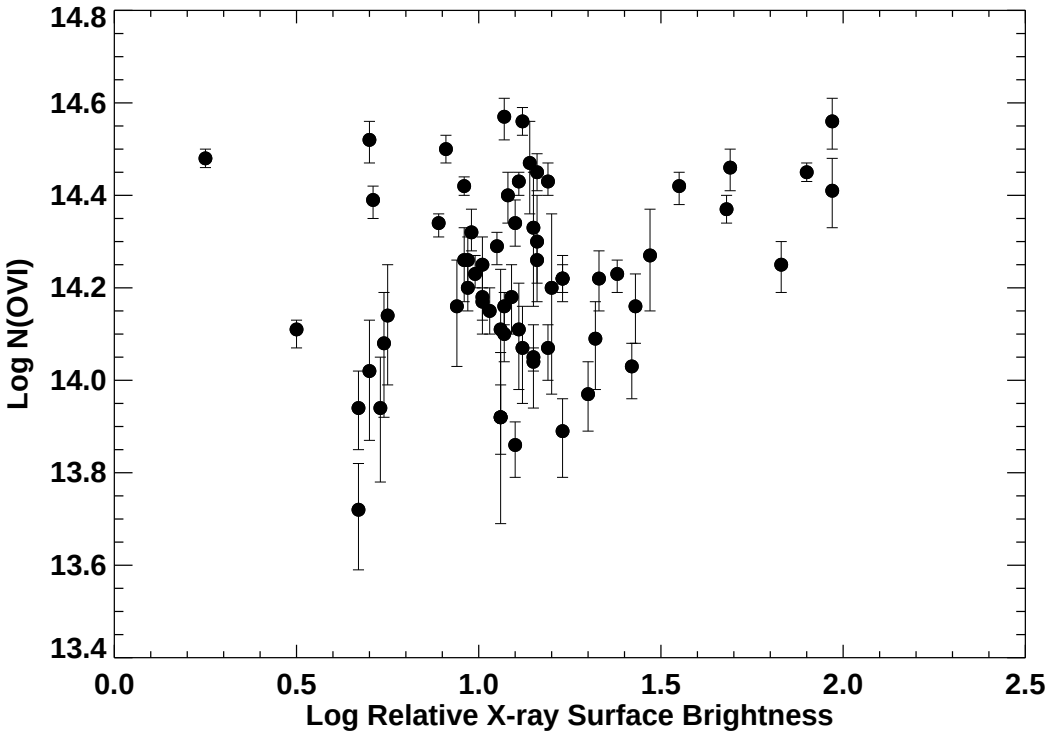

FIGURE 5.7: O VI column density (log N(O VI)) vs. log relative X-ray surface brightness for 65 targets. The X-ray surface brightness is taken from the *ROSAT* PSPC mosaic image (energy range 0.5–2.0 keV) (Snowden & Petre 1994). 4 targets (Sk-67D250, D301-1005, D301-NW8 and Sk-65D63) have not been covered by X-ray observations and one of the target Sk-69D257 has been excluded because it has extremely high X-ray emission.

winds (Castor et al. 1975; Weaver et al. 1977; Chu & Mac Low 1990), which is an ideal condition for the formation of O VI. The LMC hosts more than 20 superbubbles and recently O VI has been detected in a superbubble N70 (Danforth & Blair 2006a), where they have reported around 60% excess in abundance of O VI in comparison to non-superbubble lines of sight in the proximity of N70. The authors conclude that superbubbles act as local O VI reservoirs and have a different absorption profile compared to the non-superbubble O VI absorption profiles. They find that the O VI is formed by the thermal conduction between the interior hot X-ray producing gas and the cool photo-ionized shell of N70. Sankrit & Dixon (2007) have detected O VI in emission in several superbubbles in the LMC further emphasizing that superbubbles are important contributors to the overall O VI budget.

We have 22 O VI observations covering 10 superbubbles as shown in Figure 5.1. Of the 22 observations, 3 are in N70 (Sk-67D250, D301-1005 and D301-NW8) which have already been reported by Danforth & Blair (2006a) and 4 are in N144, N204, N206 and N154 respectively which have been discussed by Howk et al. (2002a). We report 15 new observations of O VI absorption in the superbubbles 30 Doradus C, N158, N11, N51, and N57. Significant variation in O VI abundance exists towards these lines of sight. The minimum value of log N(O VI) is 14.04 atoms cm^{-2} in superbubble N206 and the maximum value of log N(O VI) is 14.57 atoms cm^{-2} in superbubble N70. The properties of O VI in superbubbles reported here are tabulated in Table 5.3. Comparing the abundance of O VI for the superbubble and non-superbubble lines of sight, we find that the mean log N(O VI) for superbubble lines of sight is $\langle N_{SB} \rangle = 14.35$ atoms cm^{-2} while for the non-superbubble lines of sight this is $\langle N_{non-SB} \rangle = 14.19$ atoms cm^{-2}. Thus, an excess O VI abundance of about 40% in superbubbles of the LMC is found in comparison to non-superbubble regions. Combining the Danforth & Blair (2006a) and Howk et al. (2002a) data for superbubble and non-superbubble lines of sight (excluding Sk-67D05 sightline; see Howk et al. (2002a) for details), the O VI excess in superbubbles is about 46%, which is comparable to our results. Thus, results reported here support and confirm that superbubbles do show higher O VI abundance in comparison to the general halo absorption seen in other LMC lines of sight. Some of the non-superbubble lines of sight show an enhanced O VI column density owing to local effects. Lehner & Howk (2007) compared superbubble and non-superbubble lines of sight for the LMC and found that some quiescent environments showed an enhanced O VI abundance, sometimes even larger than that of superbubbles.

Even in a single superbubble, there are significant variations in the O VI column densities. We have four observations each for the superbubbles 30 Doradus C and N11. In the case of 30 Doradus C, we find that the variation in N(O VI) is more than a factor of 2 (from the minimum value of N(O VI) to the maximum value). For N11, this variation is about a factor of 2.5. The variation in N(O VI) for N70 is not much (for the three lines of sight included here) and this corroborates with the Danforth & Blair (2006a) data.

5.5 Properties of O VI in 30 Doradus

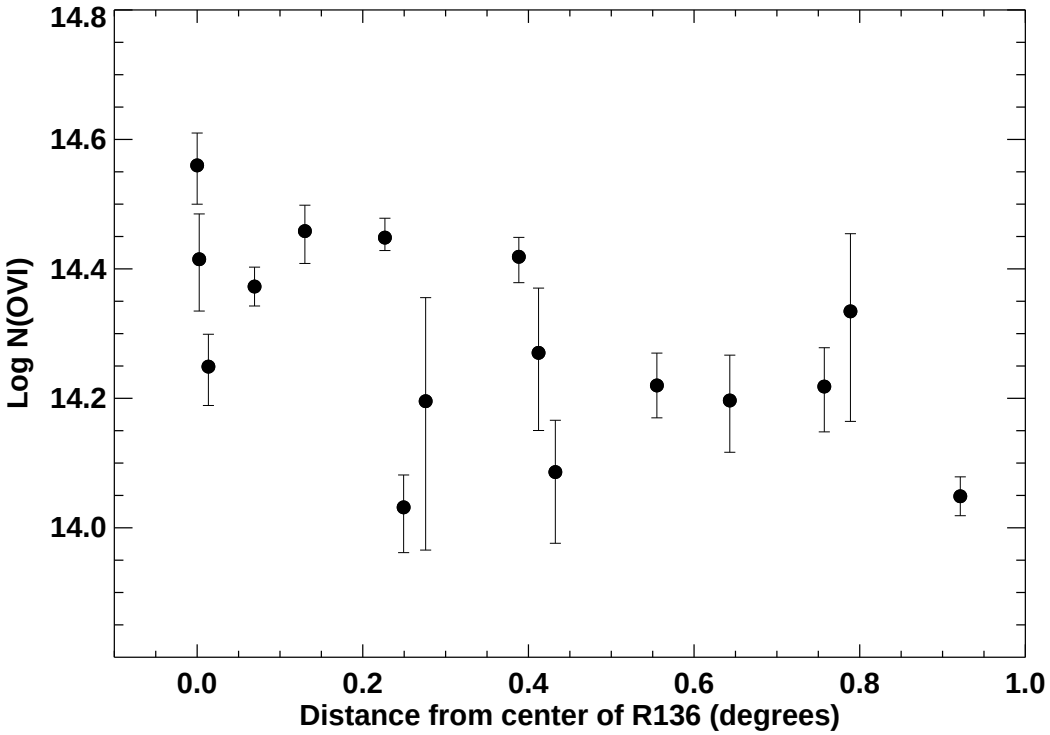

FIGURE 5.8: Variation of O VI column density (log N(O VI)) with increasing distance from the the centre of the star cluster R136 located in the 30 Doradus region of the LMC. Note that the variation is plotted within an angular distance of 1 degree from the the centre of R136.

The 30 Doradus region of the LMC is ideally suited to study the interaction between a high rate of star formation and the surrounding ISM. This region is dominated by the star forming cluster NGC 2070 that contains the very interesting star cluster R136 at the center. The proximity to 30 Doradus has allowed extensive research on the stellar content (Parker 1992; Parker & Garmany 1993a; Walborn & Blades 1997) and initial mass function (Andersen et al. 2009, and the references therein). 30 Doradus has also been investigated in detail in the infrared bands to study the dust properties (Sturm et al. 2000; Vermeij et al. 2002; Meixner et al. 2006). Indebetouw et al. (2009) studied the 30 Doradus in the mid-infrared wavelength band to determine the physical conditions of the ionized gas and found that the local effects of hot stars in 30 Doradus appear to dominate over any large-scale trend with distance from the central cluster R136.

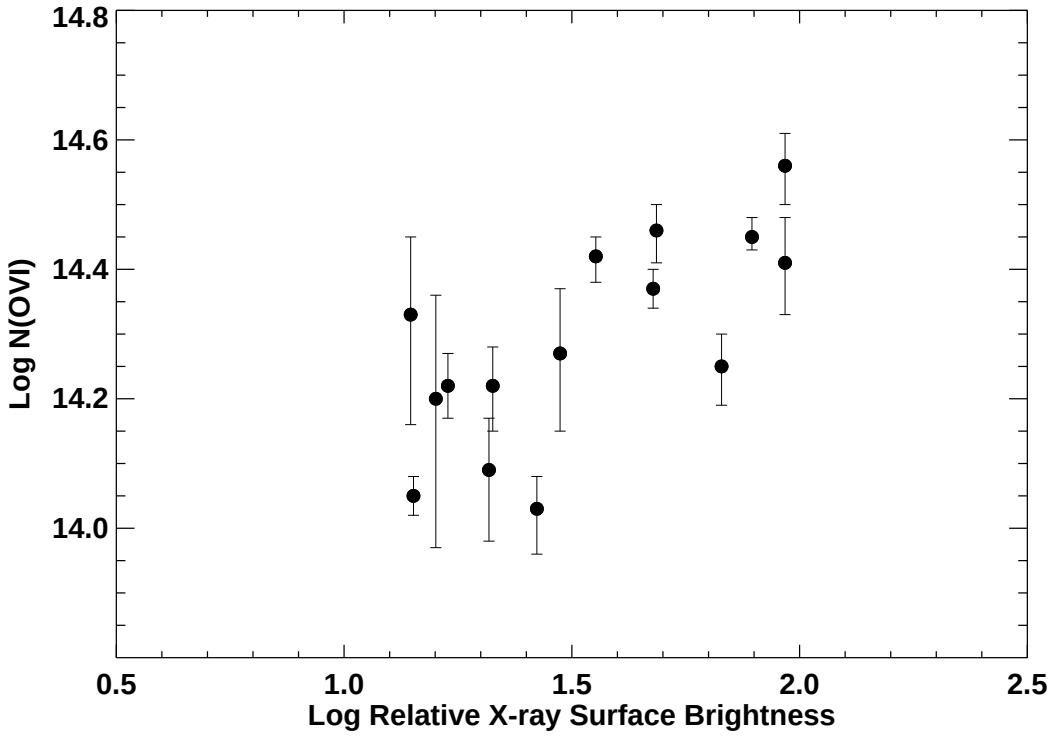

FIGURE 5.9: O VI column density (log N(O VI)) vs. X-ray luminosity for the 30 Doradus region of the LMC. The X-ray surface brightness is taken from the *ROSAT* PSPC mosaic image (energy range 0.5–2.0 keV) (Snowden & Petre 1994). A linear correlation is present which is not seen when all the targets of LMC are included (Figure 5.7) and for other individual regions in the LMC. The plot includes all lines of sight from Figure 5.8 except for 1 sightline (SK-69D257) as it shows an exceptionally high X-ray emission due to its proximity to X-ray binary LMC-X1 (Points et al. 2001).

The O VI abundance in 30 Doradus is higher than in other regions of the LMC with the highest value of log N(O VI) being 14.56 atoms cm^{-2} near the center of the cluster R136. Figure 5.8 shows the change in the log N(O VI) values from the center of R136 up to an angular distance of 1 degree. We find an overall decrease in the O VI abundance away from the center of R136. An interpretation of this plot could be that the processes involved in the formation of O VI are likely to be associated with stellar radiation field but local effects cannot be neglected on a large angular scale. It should be noted that we do not find any correlation between O VI absorption and H_α emission for LMC and thus, no relation between star formation is established on a larger scale.

As noticed earlier, log N(O VI) does not correlate with X-ray emission for the LMC as a whole but surprisingly there is a good correlation for the 30 Doradus lines of sight Figure 5.9. The correlation is between log N(O VI) and X-ray emission from 30 Doradus considering all the lines of sight within 1 degree around R136 except for one sightline (SK-69D257) that has exceptionally high value of X-ray surface brightness. One of the reasons for such high X-ray emission from SK-69D257 is its proximity to a high mass X-ray binary LMC X-1 (Points et al. 2001). The correlation in 30 Doradus suggests that O VI observed in this region is present in the ISM gas surrounding the X-ray emitting plasma, which may be due to the compactness, high density and non-uniform structure of 30 Doradus. The correlation confirms that the X-ray emitting gas cools through temperatures where O VI is being formed and supports the general consensus about the formation of O VI by collisional ionization in the interface regions between cooler photo-ionized ISM gas and hot exterior ISM gas (Slavin & Frisch 2002; Indebetouw & Shull 2004).

5.6 Summary & Conclusions

We have presented O VI column density measurements for the LMC using *FUSE* data for 70 lines of sight. This is the widest coverage of the LMC to date. The results reported here reveal significant variation in O VI column densities over a very small angular scale thus confirming the patchiness of O VI distribution in the LMC. The most important inferences drawn from this work are following:

1. This survey probes 70 lines of sight with varying environmental conditions. We find strong O VI absorption in the LMC that is not restricted to active regions. High O VI abundance is present even in relatively inactive regions of the LMC.

2. There are significant variations in the velocity profiles of O VI absorption. The O VI absorption profile is broader than the MW absorption for many lines of sight but it should be noted that unambiguous separation of the MW

and the LMC components is not possible for most of the lines of sight. This proves to be a significant hurdle in interpreting exact kinematics for O VI in the LMC (for e.g. outflows from the LMC, etc.).

3. The maximum column density measured for the LMC is log N(O VI) = 14.57 atoms cm^{-2} and minimum value is log N(O VI) = 13.72 atoms cm^{-2}. The mean value of O VI column density is <log N(O VI)> = 14.23 atoms cm^{-2}, which is slightly lower than the earlier reported value. The median value of O VI column density in the LMC comes to be 14.22 atoms cm^{-2}. The results corroborates with the previous finding that the distribution of O VI in the LMC is patchy.

4. Despite the fact that the LMC has lower metallicity than the MW, the abundance of O VI and properties of O VI absorption are similar in both the galaxies. The mean of log $N_{\perp}$(O VI) value for the MW is 14.29 atoms cm^{-2} while the projected column density for the LMC, i.e., log $N_{\perp}$(O VI) is 14.15 atoms cm^{-2}. A more extensive study for the MW suggests this value to be 14.21 atoms cm^{-2}. The SMC with even lower metallicity has higher O VI abundance with mean log N(O VI) = 14.53 atoms cm^{-2}.

5. O VI absorption in the LMC does not correlate with H_{α} (warm gas) or X-ray (hot gas) emission but we find a good correlation between O VI absorption and X-ray emission in the 30 Doradus region. It is also seen that the O VI absorption is decreasing with increasing angular distance from the star cluster R136 suggesting some correlation with stellar radiation field.

6. The observations reported cover 10 superbubbles of the LMC and for 5 superbubbles (30 Doradus C, N158, N51, N11 and N57) O VI absorption is reported for the first time. Superbubbles are O VI rich and have 40% excess compared to non-superbubble lines of sight.

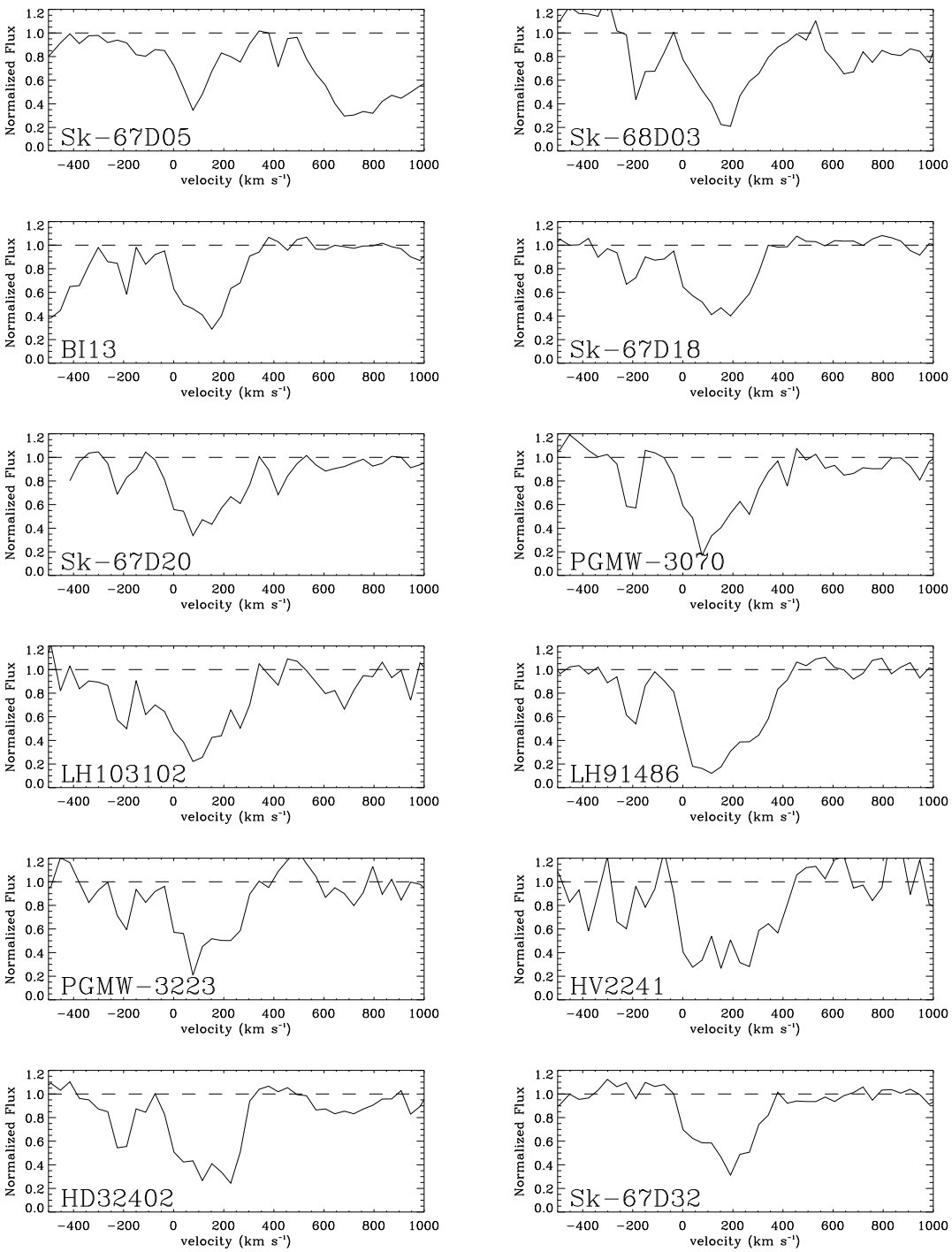

(a) Normalized OVI absorption profiles.

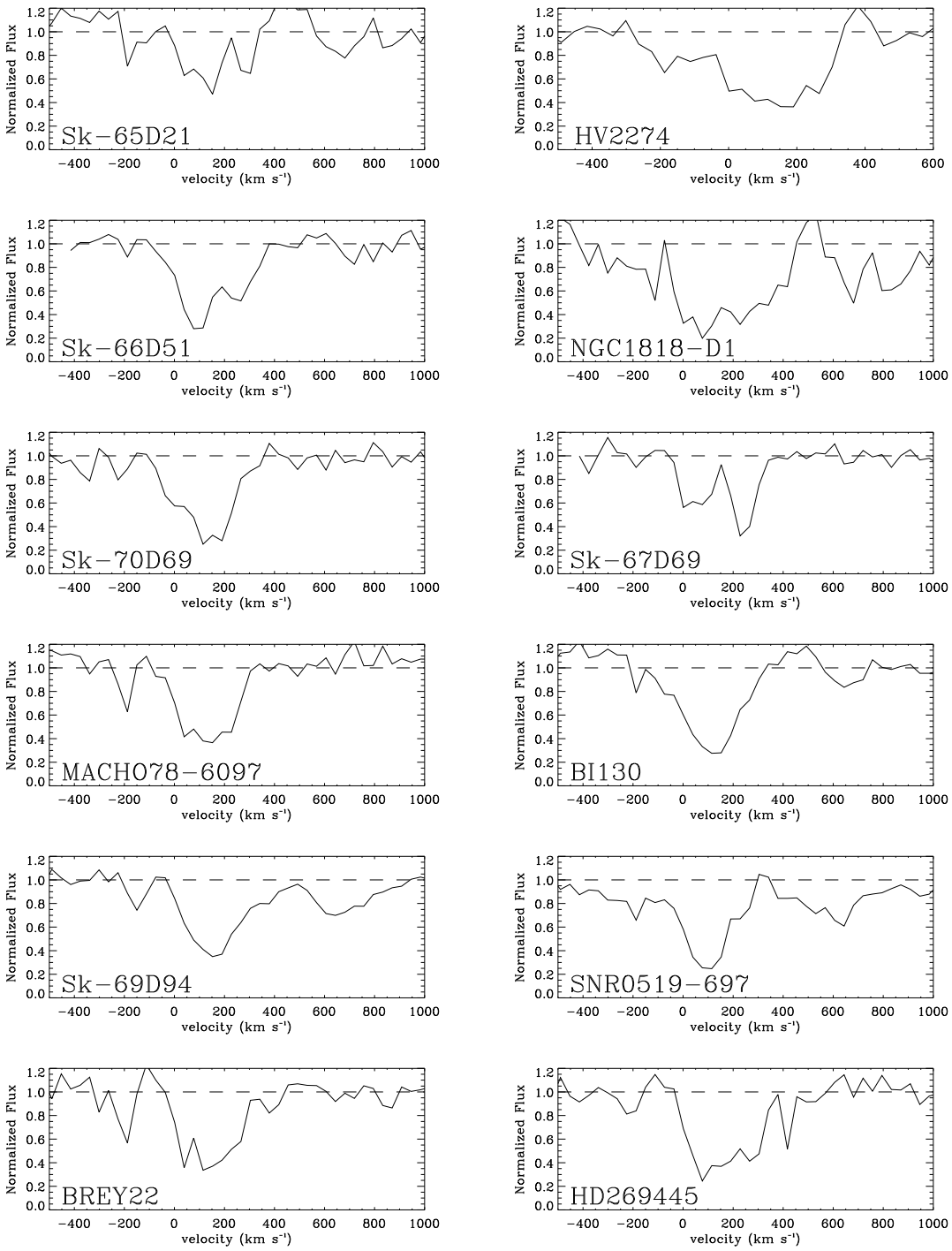

(b) Normalized OVI absorption profiles.

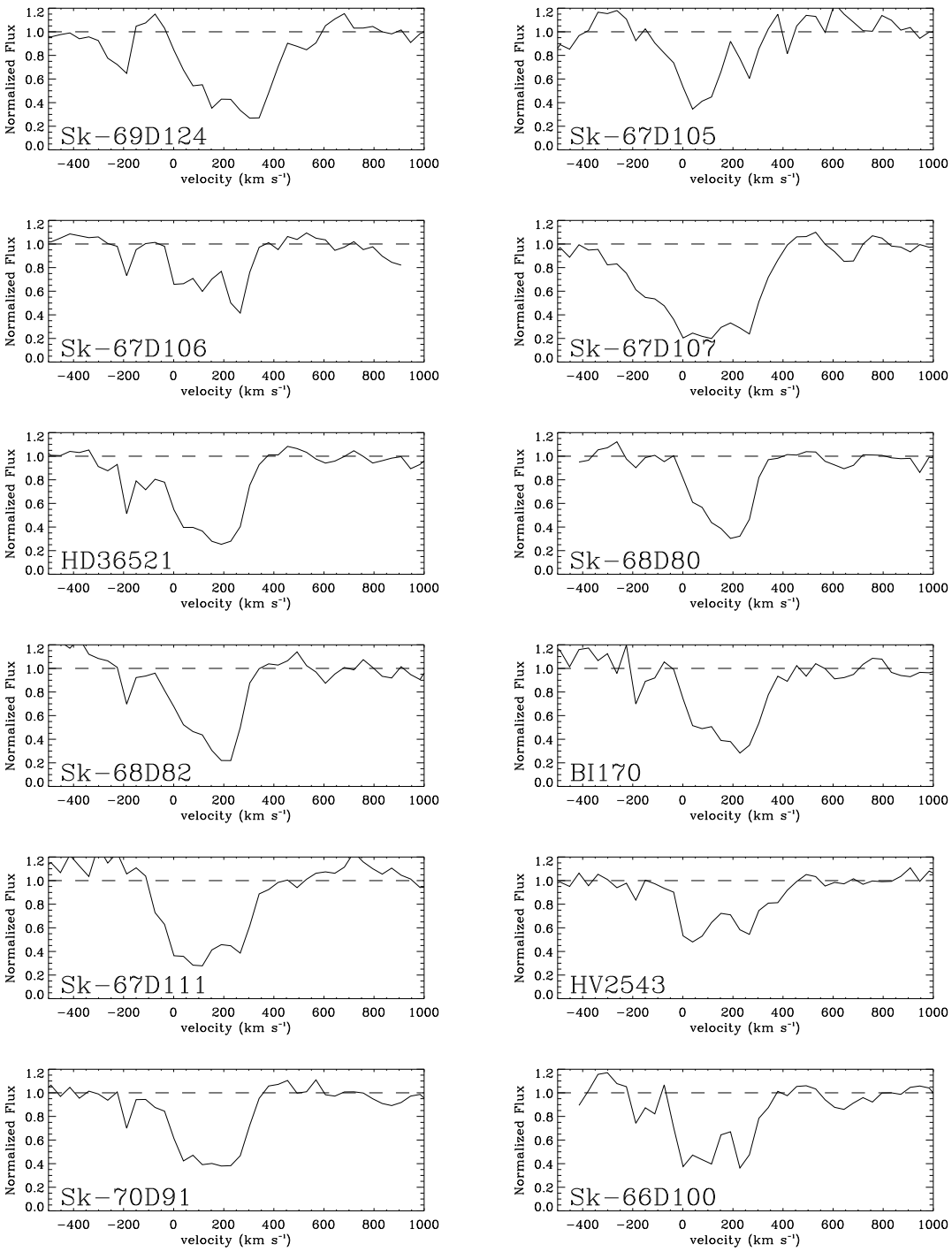

(c) Normalized OVI absorption profiles.

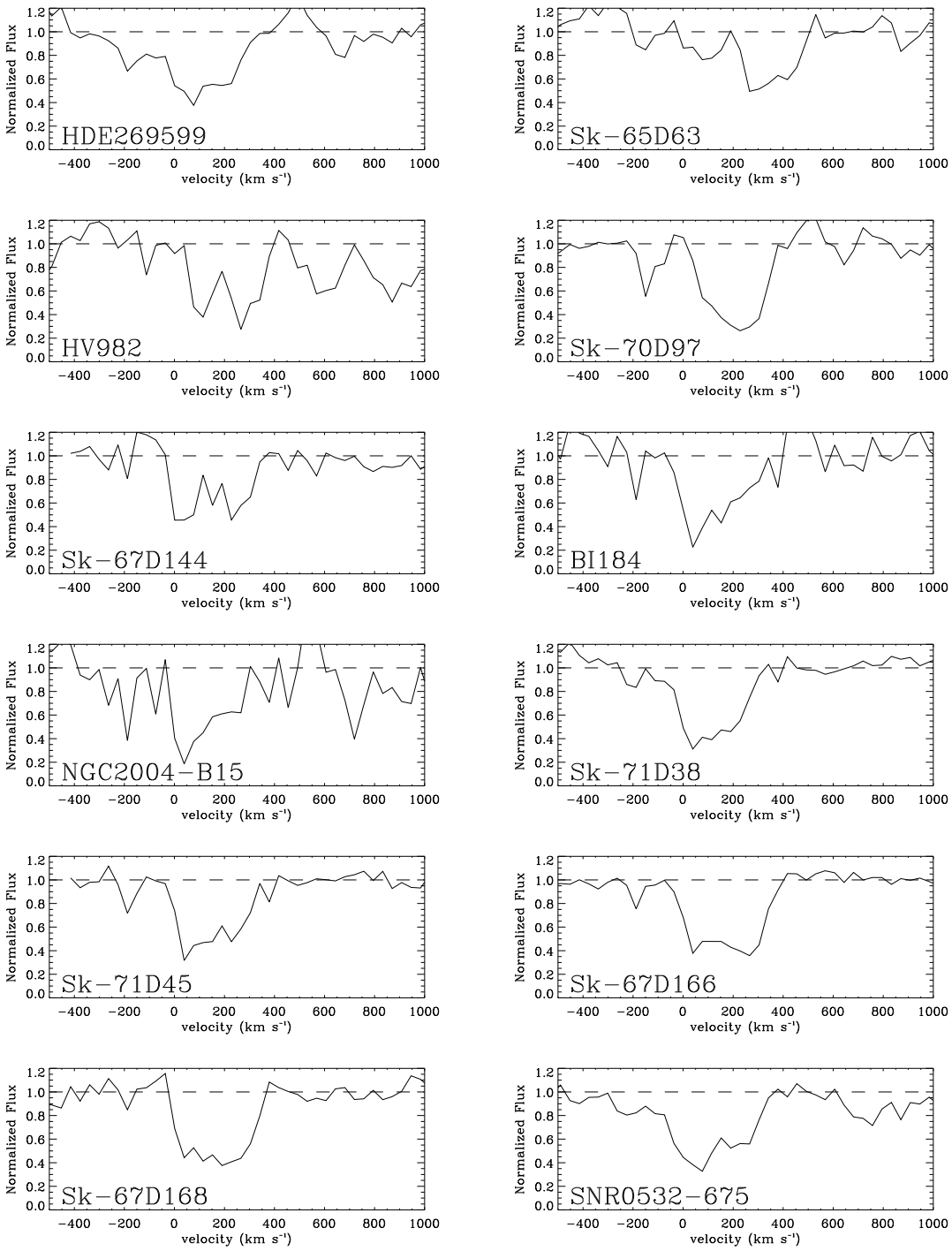

(d) Normalized OVI absorption profiles.

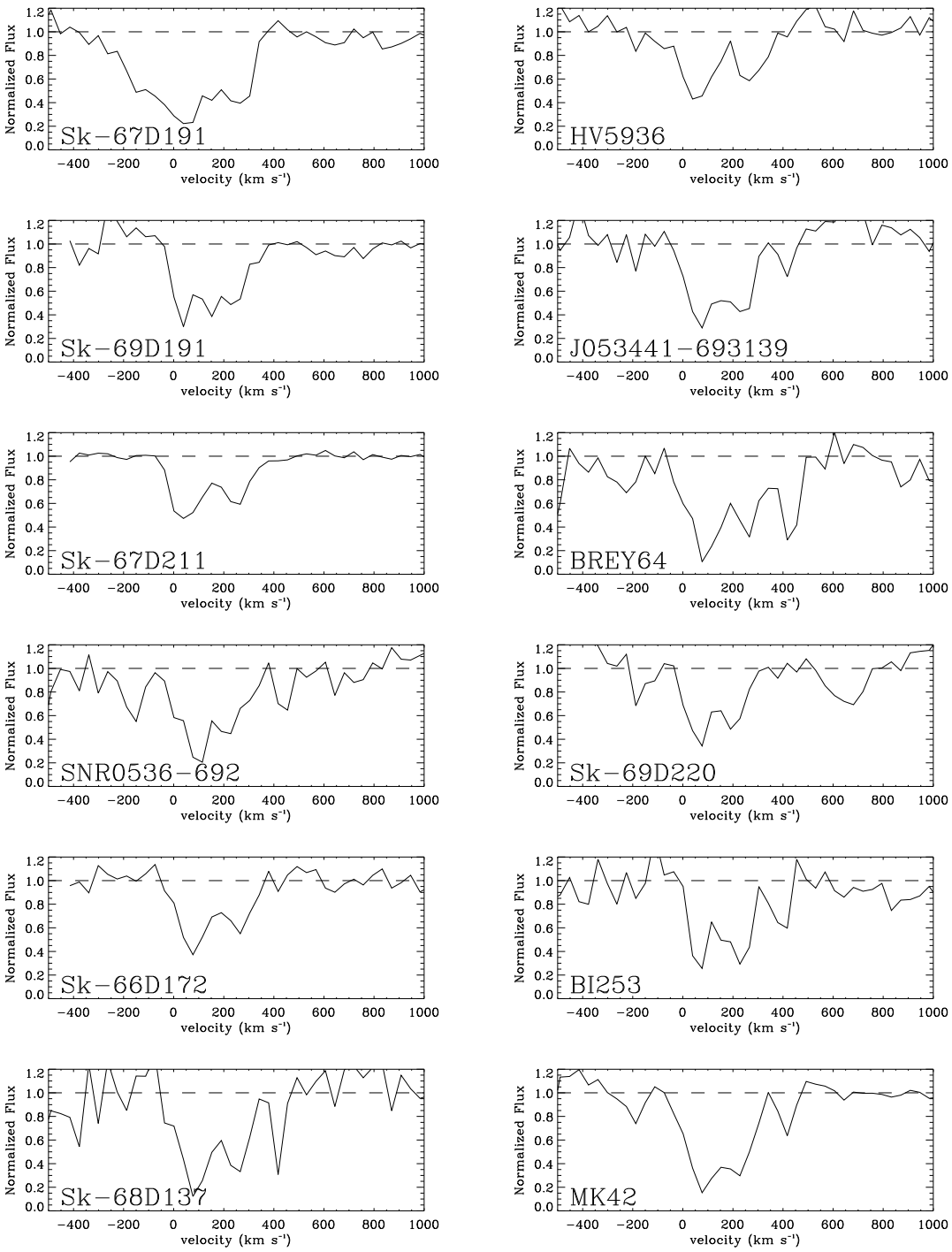

(e) Normalized OVI absorption profiles.

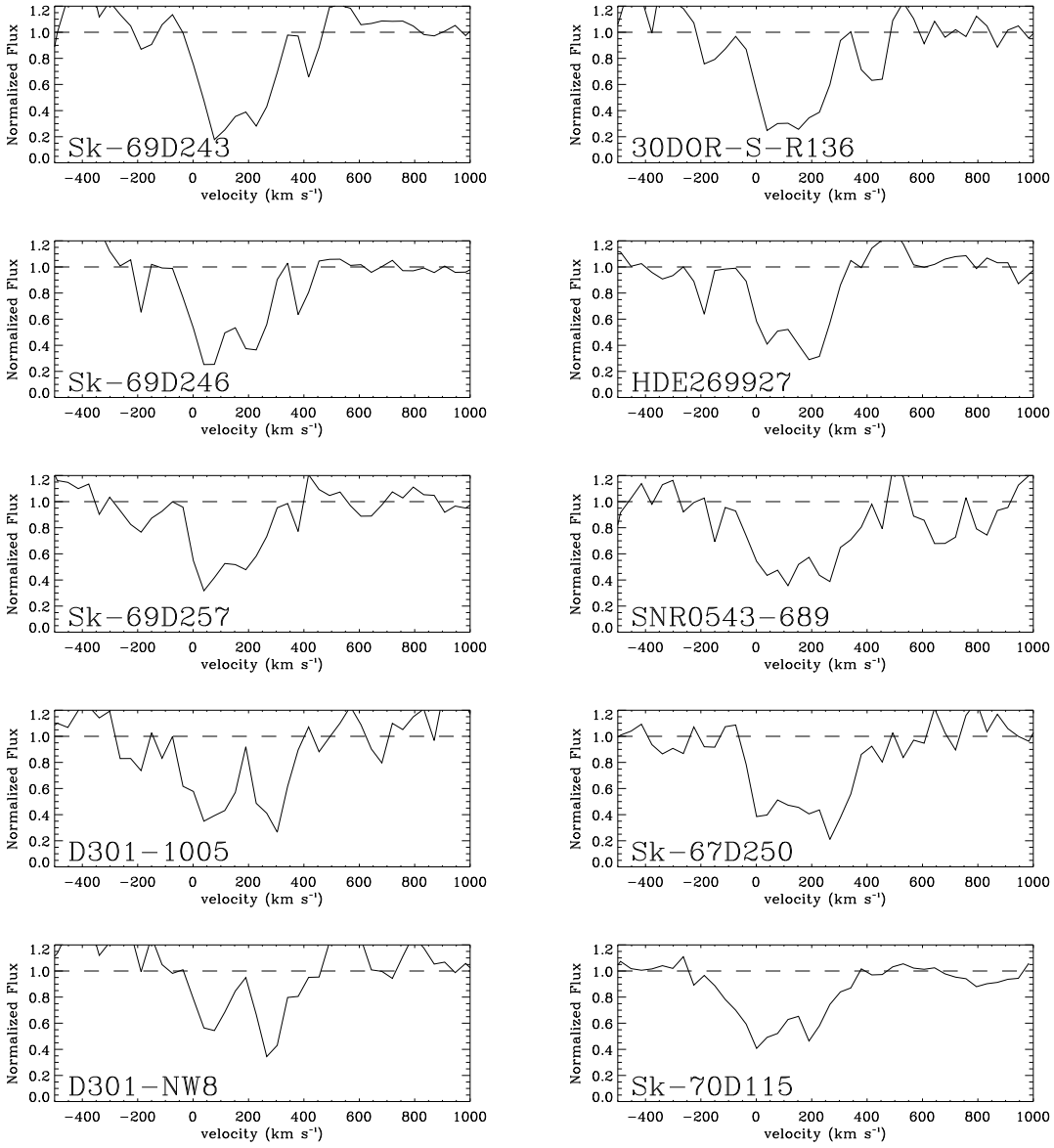

(f) Normalized OVI absorption profiles.

FIGURE 5.10: Normalized O VI absorption profiles for the 70 lines of sight.

TABLE 5.1: Log of *FUSE* observations for the 70 targets in the LMC.

FUSE ID	Object name	Aperture	Right Ascension	Declination	Spec Type	V mag.	Ref
P1030703	Sk-67D05	LWRS	04 50 18.96	-67 39 37.9	O9.7Ib	11.34	1
A0490402	Sk-68D03	LWRS	04 52 15.56	-68 24 26.9	O9I	13.13	2
E5111901	BI13	LWRS	04 53 06.48	-68 03 23.1	O6.5V	13.75	3
D0980801	Sk-67D18	MDRS	04 55 14.90	-67 11 24.5	O6-7n-nm	11.95	1
P1174401	Sk-67D20	LWRS	04 55 31.50	-67 30 01.0	WN4b	13.86	4
B0100201	PGMW-3070	MDRS	04 56 43.25	-66 25 02.0	O6V	12.75	5
D0300302	LH103102	MDRS	04 56 45.40	-66 24 45.9	O7Vz	13.55	5
D0300101	LH91486	MDRS	04 56 55.58	-66 28 58.0	O6.5Vz	14.2	5
B0100701	PGMW-3223	MDRS	04 57 00.80	-66 24 25.3	O8.5IV	12.95	5
F9270604	HV2241	LWRS	04 57 15.83	-66 33 54.8	O7-III	13.5	5
P1174901	HD32402	LWRS	04 57 24.19	-68 23 57.2	WC		3
Z9050801	Sk-67D32	LWRS	04 59 52.30	-67 56 55.0	WN	14.48	3
P1030901	Sk-65D21	LWRS	05 01 22.33	-65 41 48.1	O9.7Iab	12.02	6
B0770201	HV2274	LWRS	05 02 40.96	-68 24 21.3	B0-B2III-I	14.2	5
P1174501	Sk-66D51	LWRS	05 03 10.20	-66 40 54.0	WN8h	12.71	4
D1380201	NGC1818-D1	LWRS	05 04 32.56	-66 24 51.0	B0-B2V-IV	14.93	5
P1172101	Sk-70D69	LWRS	05 05 18.73	-70 25 49.8	O5V	13.94	6
P1171703	Sk-67D69	LWRS	05 14 20.16	-67 08 03.5	O4III(f)	13.09	7
C1030101	MACHO78-6097	LWRS	05 18 04.70	-69 48 19.0	B0-B2V-IV	14.4	5
E5112902	BI130	LWRS	05 18 06.06	-69 14 34.5	O8.5V((f))	12.53	3
Z9050201	Sk-69D94	LWRS	05 18 14.53	-69 15 01.0	B0-B2III-I	9.72	5
D9044701	SNR0519-697	LWRS	05 18 44.20	-69 39 12.4	SNR		
D0880104	BREY22	MDRS	05 19 16.40	-69 39 19.5	WC/O9.5Ib	12.3	1
B0270101	HD269445	LWRS	05 22 59.87	-68 01 46.6	WN	11.45	1
P1173602	Sk-69D124	LWRS	05 25 18.37	-69 03 11.1	O9Ib	12.81	2
D1530104	Sk-67D105	LWRS	05 26 06.37	-67 10 57.6	Of	12.42	5
A1110101	Sk-67D106	MDRS	05 26 15.20	-67 29 58.3	B0-B2III-I	11.78	8
A1110201	Sk-67D107	MDRS	05 26 20.67	-67 29 55.4	B0-B2III-I	12.5	8
C1510101	HD36521	LWRS	05 26 30.32	-68 50 25.4	WC	12.42	9
P1031402	Sk-68D80	LWRS	05 26 30.43	-68 50 26.6	WC4+OB	12.40	10
P2030104	Sk-68D82	LWRS	05 26 45.31	-68 49 52.8	WN5?b+(B3I)	9.86	5
P1173701	BI170	LWRS	05 26 47.79	-69 06 11.7	O9.5Ib	13.09	11
C1550201	Sk-67D111	LWRS	05 26 47.95	-67 29 29.9	O6:Iafpe	12.57	11
F9270701	HV2543	LWRS	05 27 27.40	-67 11 55.4	O8+O9	12.92	5
P1172501	Sk-70D91	LWRS	05 27 33.74	-70 36 48.3	O6.5V	12.78	11
P1172303	Sk-66D100	LWRS	05 27 45.59	-66 55 15.0	O6II(f)	13.26	6
E9570301	HDE269599	LWRS	05 28 22.68	-69 08 32.2	Be	10.18	5

Continued on Next Page...

Table 5.1 – Continued

FUSE ID	Object name	Aperture	Right Ascension	Dec	Spectral Type	V mag.	Ref
M1142001	Sk-65D63	LWRS	05 28 39.50	-65 39 01.1	O9.7I	12.56	12
C1030201	HV982	LWRS	05 29 52.50	-69 09 22.0	B0-B2V-IV	14.6	5
E5113602	Sk-70D97	LWRS	05 30 11.35	-70 51 42.2	O9III	13.33	5
P1175001	Sk-67D144	LWRS	05 30 12.22	-67 26 08.4	WC4+OB	13.6	13
P2170301	BI184	LWRS	05 30 30.60	-71 02 31.3	B0-B2V-IV	13.84	3
D1380301	NGC2004-B15	MDRS	05 30 36.58	-67 17 42.3	B0-B2V-IV	14.18	5
Z9050601	Sk-71D38	LWRS	05 30 38.77	-71 01 47.9	WC	13.1	5
P1031502	Sk-71D45	LWRS	05 31 15.55	-71 04 08.9	O4-5III(f)	11.51	1
A1330123	Sk-67D166	LWRS	05 31 44.31	-67 38 00.6	O4If+	12.27	1
B0860901	Sk-67D168	MDRS	05 31 52.10	-67 34 20.8	O8Iaf	12.08	12
D9042002	SNR0532-675	LWRS	05 32 23.00	-67 31 02.0	SNR		
P1173101	Sk-67D191	LWRS	05 33 34.12	-67 30 19.6	O8V	13.46	2
B0770302	HV5936	LWRS	05 33 39.00	-66 37 39.8	B0-B2V-IV	14.8	5
P1175101	Sk-69D191	LWRS	05 34 19.39	-69 45 10.0	WC4	13.35	13
F3210301	J053441-693139	LWRS	05 34 41.30	-69 31 39.0	O2-O3.5If*	13.7	14
P1171603	Sk-67D211	LWRS	05 35 13.92	-67 33 27.0	O2III(f)*	12.28	14
Z9051001	BREY64	LWRS	05 35 54.45	-68 59 07.4	WN9h	13.21	3
D9043101	SNR0536-692	LWRS	05 36 07.70	-69 11 52.6	SNR		
Z9050701	Sk-69D220	LWRS	05 36 43.83	-69 29 47.4	WNorOiafpe	10.58	1
P1172201	Sk-66D172	LWRS	05 37 05.56	-66 21 35.7	O2III(f)*+OB	13.13	14
C0020601	BI253	LWRS	05 37 34.49	-69 01 09.8	Of	13.76	3
E5114201	Sk-68D137	LWRS	05 38 24.77	-68 52 32.8	O3IIIf	13.29	3
P1171803	MK42	LWRS	05 38 42.10	-69 05 54.7	O3If/WN6-A	10.96	15
P1031706	Sk-69D243	LWRS	05 38 42.57	-69 06 03.2	WN5+OB	9.5	16
F9140101	30DOR-S-R136	LWRS	05 38 51.70	-69 06 00.0	H II region		
P1031802	Sk-69D246	LWRS	05 38 53.50	-69 02 00.7	WN	11.16	4
P1174601	HDE269927	LWRS	05 38 58.25	-69 29 19.1	WN	12.63	4
P2170101	Sk-69D257	LWRS	05 39 58.91	-69 44 03.2	O9II	12.53	5
D9042801	SNR0543-689	LWRS	05 43 07.20	-68 58 52.0	SNR		
D0981401	D301-1005	MDRS	05 43 08.30	-67 50 52.4	O9.5V	14.11	3
D0981201	Sk-67D250	MDRS	05 43 15.48	-67 51 09.6	O7.5II(f)	12.68	17
D0981501	D301-NW8	MDRS	05 43 15.96	-67 49 51.0	D301-NW8	14.37	3
I8120701	Sk-70D115	LWRS	05 48 49.76	-70 03 57.5	O6.5Iaf	12.24	5

Notes. Units of right ascension are hours, minutes, and seconds; units of declination are in degrees, arcminutes and arcseconds.

References – (1) Walborn (1977); (2) Conti et al. (1986); (3) Massey (2002); (4) Smith et al.

(1996); (5) Blair et al. (2009); (6) Walborn et al. (1995); (7) Garmany & Walborn (1987) (8) Rousseau et al. (1978); (9) Moffat et al. (1990); (10) Smith et al. (1990); (11) Walborn et al. (2002b) (12) Fitzpatrick & Massa (1988); (13) Torres-Dodgen & Massey (1988); (14) Walborn et al. (2002a); (15) Walborn & Blades (1997); (16) Massey & Hunter (1998); (17) Massey et al. (1995).

TABLE 5.2: Equivalent widths and column densities with corresponding velocity limits over which the integration is performed for O VI absorption in the LMC.

Target name	Equivalent width (mÅ)	log N(O VI) (dex)	Integration limits (km s^{-1})
Sk-67D05	73±6	$13.72^{+0.10}_{-0.13}$	175, 330
Sk-68D03	112±8	$14.02^{+0.11}_{-0.15}$	180, 330
BI13	88±4	$13.94^{+0.08}_{-0.09}$	175, 315
Sk-67D18	132±7	$14.16^{+0.09}_{-0.13}$	165, 330
Sk-67D20	147±8	$14.08^{+0.11}_{-0.16}$	175, 335
PGMW-3070	132±23	$14.10^{+0.13}_{-0.18}$	180, 345
LH103102	132±23	$14.16^{+0.03}_{-0.04}$	180, 330
LH91486	266±29	$14.47^{+0.09}_{-0.11}$	175, 385
PGMW-3223	129±15	$14.10^{+0.06}_{-0.07}$	175, 315
HV2241	271±18	$14.50^{+0.04}_{-0.03}$	165, 365
HD32402	271±8	$14.48^{+0.02}_{-0.02}$	160, 320
Sk-67D32	129±7	$14.11^{+0.03}_{-0.04}$	165, 360
Sk-65D21	94±23	$13.94^{+0.11}_{-0.16}$	225, 340
HV2274	160±11	$14.14^{+0.10}_{-0.15}$	165, 345
Sk-66D51	185±10	$14.26^{+0.07}_{-0.09}$	170, 370
NGC1818-D1	280±13	$14.52^{+0.05}_{-0.05}$	150, 340
Sk-70D69	182±12	$14.18^{+0.07}_{-0.08}$	150, 295
Sk-67D69	232±28	$14.40^{+0.05}_{-0.06}$	170, 340
MACHO78-6097	151±25	$14.15^{+0.05}_{-0.05}$	165, 320
BI130	94±7	$13.89^{+0.07}_{-0.09}$	165, 320
Sk-69D94	150±3	$14.22^{+0.03}_{-0.03}$	160, 340
SNR0519-697	97±4	$13.97^{+0.07}_{-0.08}$	160, 300
BREY22	126±24	$14.07^{+0.06}_{-0.07}$	160, 330
HD269445	200±10	$14.29^{+0.04}_{-0.05}$	175, 365
Sk-69D124	331±8	$14.57^{+0.04}_{-0.05}$	190, 430
Sk-67D105	110±8	$13.92^{+0.14}_{-0.23}$	180, 320
Sk-67D106	180±7	$14.30^{+0.10}_{-0.13}$	175, 345
Sk-67D107	254±10	$14.45^{+0.04}_{-0.05}$	160, 360

Continued on Next Page...

Table 5.2 – Continued

Target name	Equivalent width (mÅ)	log N(O VI) (dex)	Integration limits (km s^{-1})
HD36521	126±9	$14.07^{+0.09}_{-0.12}$	175, 340
Sk-68D80	303±16	$14.56^{+0.04}_{-0.03}$	145, 335
Sk-68D82	141±10	$14.17^{+0.04}_{-0.04}$	165, 320
BI170	235±20	$14.43^{+0.02}_{-0.03}$	165, 365
Sk-67D111	214±19	$14.34^{+0.05}_{-0.05}$	175, 365
HV2543	156±42	$14.23^{+0.04}_{-0.03}$	160, 365
Sk-70D91	256±7	$14.43^{+0.04}_{-0.03}$	160, 365
Sk-66D100	214±21	$14.34^{+0.03}_{-0.03}$	160, 340
HDE269599	123±6	$14.05^{+0.03}_{-0.03}$	165, 320
Sk-65D63	184±8	$14.21^{+0.04}_{-0.04}$	180, 375
HV982	208±58	$14.33^{+0.12}_{-0.17}$	175, 360
Sk-70D97	226±4	$14.39^{+0.03}_{-0.04}$	175, 375
Sk-67D144	194±10	$14.25^{+0.06}_{-0.07}$	165, 335
BI184	118±10	$14.04^{+0.08}_{-0.10}$	165, 330
NGC2004-B15	92±7	$13.86^{+0.05}_{-0.07}$	175, 330
Sk-71D38	94±7	$13.92^{+0.07}_{-0.08}$	165, 315
Sk-71D45	194±9	$14.26^{+0.06}_{-0.06}$	160, 345
Sk-67D166	206±9	$14.32^{+0.05}_{-0.05}$	165, 390
Sk-67D168	186±12	$14.26^{+0.05}_{-0.05}$	165, 375
SNR0532-675	147±9	$14.16^{+0.07}_{-0.08}$	165, 345
Sk-67D191	229±16	$14.42^{+0.02}_{-0.02}$	165, 340
HV5936	174±8	$14.18^{+0.07}_{-0.08}$	175, 375
Sk-69D191	185±25	$14.22^{+0.06}_{-0.07}$	165, 340
J053441-693139	182±33	$14.22^{+0.05}_{-0.05}$	165, 330
Sk-67D211	144±8	$14.11^{+0.10}_{-0.13}$	160, 350
BREY64	139±8	$14.20^{+0.16}_{-0.23}$	180, 330
SNR0536-692	116±7	$14.03^{+0.05}_{-0.07}$	165, 320
Sk-69D220	128±9	$14.09^{+0.08}_{-0.11}$	160, 315
Sk-66D172	173±9	$14.20^{+0.05}_{-0.05}$	175, 360
BI253	259±46	$14.46^{+0.04}_{-0.05}$	160, 300

Continued on Next Page...

Table 5.2 – Continued

Target name	Equivalent width (mÅ)	log N(O VI) (dex)	Integration limits (km s^{-1})
Sk-68D137	234±7	$14.45^{+0.03}_{-0.02}$	165, 330
MK42	228±24	$14.41^{+0.07}_{-0.08}$	160, 330
Sk-69D243	307±15	$14.56^{+0.05}_{-0.06}$	150, 345
30DOR-S-R136	185±25	$14.25^{+0.05}_{-0.06}$	165, 320
Sk-69D246	211±7	$14.37^{+0.03}_{-0.03}$	155, 325
HDE269927	245±8	$14.42^{+0.03}_{-0.04}$	160, 320
Sk-69D257	171±8	$14.20^{+0.07}_{-0.08}$	160, 315
SNR0543-689	186±34	$14.27^{+0.10}_{-0.12}$	160, 360
D301-1005	284±57	$14.53^{+0.02}_{-0.03}$	165, 385
Sk-67D250	316±33	$14.57^{+0.03}_{-0.03}$	165, 375
D301-NW8	228±30	$14.42^{+0.02}_{-0.03}$	175, 365
Sk-70D115	186±11	$14.23^{+0.03}_{-0.04}$	165, 330

Notes. The errors in equivalent widths and column densities are 1σ error estimates. Integration limits gives the velocity range over which the LMC O VI absorption profile was integrated.

TABLE 5.3: O VI column densities in the superbubbles (SB) of the LMC.

Target name	Superbubble	Column density (10^{14} atoms cm^{-2})	log N(O VI) (dex)
Sk-69D246	30Dor C	$2.36^{+0.18}_{-0.14}$	$14.37^{+0.03}_{-0.03}$
MK42	30Dor C	$2.60^{+0.46}_{-0.45}$	$14.41^{+0.07}_{-0.08}$
30DOR-S-R136	30Dor C	$1.77^{+0.20}_{-0.24}$	$14.25^{+0.05}_{-0.06}$
Sk-69D243	30Dor C	$3.63^{+0.40}_{-0.45}$	$14.56^{+0.05}_{-0.06}$
Sk-69D191	N154	$1.65^{+0.26}_{-0.23}$	$14.22^{+0.06}_{-0.07}$
HDE269927	N158	$2.62^{+0.16}_{-0.21}$	$14.42^{+0.03}_{-0.04}$
Sk-68D80	N144	$3.61^{+0.30}_{-0.26}$	$14.56^{+0.04}_{-0.03}$
HD36521	N144	$1.18^{+0.28}_{-0.28}$	$14.07^{+0.09}_{-0.11}$
BI184	N206	$1.09^{+0.22}_{-0.22}$	$14.04^{+0.08}_{-0.10}$
Sk-71D45	N206	$1.80^{+0.24}_{-0.21}$	$14.26^{+0.06}_{-0.06}$
Sk-70D91	N204	$2.69^{+0.24}_{-0.17}$	$14.43^{+0.04}_{-0.03}$
PGMW-3223	N11	$1.27^{+0.18}_{-0.18}$	$14.10^{+0.06}_{-0.07}$
LH103102	N11	$1.46^{+0.10}_{-0.13}$	$14.16^{+0.03}_{-0.04}$
PGMW-3070	N11	$1.27^{+0.43}_{-0.43}$	$14.10^{+0.13}_{-0.18}$
LH91486	N11	$2.96^{+0.68}_{-0.68}$	$14.47^{+0.09}_{-0.11}$
Sk-67D111	N51	$2.20^{+0.29}_{-0.24}$	$14.34^{+0.05}_{-0.05}$
Sk-67D107	N51	$2.85^{+0.27}_{-0.27}$	$14.45^{+0.04}_{-0.05}$
Sk-67D106	N51	$2.01^{+0.50}_{-0.53}$	$14.30^{+0.10}_{-0.13}$
Sk-67D166	N57	$2.09^{+0.25}_{-0.20}$	$14.32^{+0.05}_{-0.05}$
Sk-67D250	N70	$3.71^{+0.23}_{-0.23}$	$14.57^{+0.03}_{-0.03}$
D301-1005	N70	$3.37^{+0.17}_{-0.22}$	$14.53^{+0.02}_{-0.03}$
D301-NW8	N70	$2.60^{+0.09}_{-0.13}$	$14.42^{+0.02}_{-0.03}$
Total SB (this work)		2.31±0.12	14.35±0.18
Total non-SB (this work)		1.68±0.12	14.19±0.23
Total SB N70[1]		3.04±0.45	14.48±0.06
Total non-SB[1]		2.03±0.58	14.29±0.14
Total SB[2]		3.07±0.62	14.48±0.09
Total non-SB[2]		2.10±0.50	14.31±0.11

Notes. The superbubble lines of sight are shown in Figure 5.1.

(1) Danforth & Blair (2006a); (2) Combined data of Howk et al. (2002a) and Danforth & Blair (2006a).

Chapter 6

Summary & Conclusions

6.1 Summary

The ISM is the space between stars consisting of atoms, molecules and ionized gases at various temperatures and dust grains that contain a large fraction of the elements heavier than hydrogen and helium. Although dust grains account for only 1% of the mass of the ISM, these are observed in every line of sight obscuring stars and galaxies. Therefore, the analysis of spectra of celestial objects requires a proper understanding of the physical and chemical properties of the ISM and in particular the interstellar dust. Most of the energy input into the dust comes from energetic UV photons emitted by hot young stars (Law et al. 2011). A part of the stellar UV radiation is scattered by interstellar dust, which is observed as diffuse UV radiation and the rest is absorbed and re-emitted in the IR wavelength band of the electromagnetic spectrum. We have given an overview of the dust grain properties such as extinction, emission, absorption, scattering, polarization and distribution, and the properties of gas components at different temperatures with a brief description of their detection methods in chapter 1.

The Magellanic Clouds are interesting nearby extra-galactic objects to investigate the connection between starlight and diffuse light as well as the properties of the

dust and gas in the ISM condition with low metallicity and under abundance of dust. The ISM of the MCs can be treated as relatively primitive because of its low metallicty and can be the stepping stone in our understanding of the ISM in high red-shift galaxies. We have presented the first observations of the FUV diffuse emission (1000 Å– 1150 Å) from the MCs that is dependent on both the amount of starlight and the relative geometry of the dust and the stars.

Diffuse UV light is dominated by radiation from hot stars scattered by interstellar dust grains. The intensity of this background radiation depends on the distribution of hot stars, amount and distribution of dust grains, optical depth and the optical parameters of dust. Chapter 2 provides a comprehensive literature survey on FUV diffuse background radiation and discusses about the various components of it. We have also described the data reduction method (Murthy & Sahnow 2004) that is employed to extract the diffuse surface brightness from the *FUSE* spectra and presented the first observations of FUV diffuse emission for the MCs. A brief description of the *FUSE* instrument along with the data reduction techniques are also given in Chapter 2.

81 bright FUV diffuse observations in the LMC are reported in Chapter 3. Most of these observation are near OB associations. The intensities of these observations range from around 10^3 photons cm^{-2} s^{-1} sr^{-1} Å^{-1} to as high as 3×10^5 photons cm^{-2} s^{-1} sr^{-1} Å^{-1} at *FUSE* bands with negligibly small contribution from the Galactic diffuse radiation. A good correlation between the *FUSE* diffuse radiation and the diffuse radiation measured from the *UIT* exists. Based on this correlation, and using the stellar catalog of Parker et al. (1998), we have estimated the fraction of diffuse radiation emanating from the LMC. These fractions vary in different regions of the LMC. The fractions range from 5% to 20% of the total integrated emission at 1100 Å, with a high of 45% in the superbubble N70, and with an observed error of 12% – 17%. The shape of the diffuse fraction is same in all the 10 *UIT* regions rising by a factor of about 5 from 1000 Åto 1500 Å, suggesting that most of the heating of the interstellar dust comes in the FUV in the LMC is shown by Law et al. (2011) for starburst galaxies.

We report 30 diffuse observations in various environments of the SMC in Chapter

4. These observations cover different regions of the SMC with several near hot stars of the bar region to regions further out in the edges of the galaxy. The strength of these diffuse signals range from around 10^3 photons cm^{-2} s^{-1} sr^{-1} Å^{-1} to as high as 2.5 $\times$ 10^5 photons cm^{-2} s^{-1} sr^{-1} Å^{-1}. We estimated the FUV diffuse fraction in the SMC and found significant variations in different regions. The diffuse FUV fraction ranges between 34% – 44% in the *FUSE* bands (1000 – 1150 Å) with a further increase upto 63% at 1615 Å. In case of the SMC, the behaviour of the diffuse fraction is almost the same as the LMC, rising by 10% from 1000 Å to 1150 Å and a further 50% from 1150 Åto 1615 Å, suggesting that the albedo of the dust increases by about the same factor. The FUV diffuse emission in the H II regions of the SMC correlates nicely with the Hα emissions.

The behaviour and distribution of FUV diffuse emission and emission fraction are quite similar in both the LMC and the SMC. It is also seen that much of the stellar radiation in the MCs is non-local i.e., the diffuse (scattered) light in a particular region is the light coming from distant stars being scattered by local dust. The diffuse fraction in the SMC is higher than the LMC which is attributed to the relatively higher value of albedo of SMC dust compared to the LMC dust.

Interstellar dust manifests itself by interaction with ambient radiation field of ISM and plays an important role in over all energy balance of ISM either by heating or cooling the ISM. Five times ionized oxygen (O VI) is a tracer of hot gas at a temperature of around 3$\times$ 10^5 K. High resolution absorption spectra taken by *FUSE* for 70 lines of sight is reported in Chapter 5. These observations have been used as a wide survey of O VI column density measurements for the LMC. The measurement details are given in Howk et al. (2002a); Savage & Sembach (1991); Sembach & Savage (1992). The O VI column density varies from a minimum of log N(O VI) = 13.72 atoms cm^{-2} to a maximum value of log N(O VI) = 14.57 atoms cm^{-2}. A high abundance of O VI both in active (super bubble region) and inactive regions of the LMC is found. The abundance and properties of O VI absorption are similar in the LMC and the MW despite the fact that the LMC has lower metallicity than the MW. O VI absorption in the LMC does not correlate with Hα (warm gas) or X-ray (hot gas) observations but shows correlation with X-ray brightnesses in the 30 Doradus region, the most active star formation region in the

LMC and the O VI column density decreases with an increase in angular distance from the star cluster R136 suggesting that the strength of the stellar wind from the central cluster decreases outwards.

6.1.1 Future Plans

Using the *FUSE* spectra, we have been able to report for the first time FUV diffuse emission measurements for two nearby galaxies, the LMC and the SMC. The importance of the FUV diffuse emission measurement lies in the fact that they provide a good idea about the distribution of dust and its interaction with FUV starlight in these galaxies. An important result obtained by these studies is that the scattered FUV diffuse radiation in a particular region is not only due to local stars but also from distant stars. We found that the scattering correlates well with the albedo values of the dust in the MCs, thus proving that the diffuse FUV emission is starlight scattered off dust.

Based on these measurements, we plan to do a detailed theoretical modelling. The theoretical models will be of utmost use in providing the optical properties of the dust in the MCs *i.e.*, the albedo and the phase function for the dust grains. We would also like to extend our estimation of FUV diffuse measurements to other wavelength bands such as optical and IR. We would especially be using data obtianed by the *SPITZER* and *Herschel* space telescope for the MW, the MCs. We plan to have a spectral energy distribution plot of the diffuse emission ranging from the UV to IR wavelength bands.

I have also studied OVI (O+5) absorption in the LMC and OVI emission for symbiotic stars in the SMC which tells us about the properties of hot gas in the interstellar medium and its dependence on environmental conditions. Studies of the hot gaseous content of the Milky Way and the Magellanic Clouds are important for understanding the energy input into the ISM from the stars. One way to study the hot gas content is through the analysis of ultraviolet absorption and emission lines such as lithium like oxygen ion (OVI). So both absorption and emission from atoms in the extreme and FUV wavelengths is key to our understanding of the

origin, distribution and physical processes of the hot ISM as well as kinematics of gases. We have also assessed a much broader sample of observations from FUSE archive to look into the distribution of OVI absorption in the LMC and obtained a small scale distribution to look more closely the global distribution of OVI absorption in the LMC. We found a patchiness of OVI distribution even in small spatial scale. Now I am looking into an expanded morphology analysis, incorporating not only the optical data, but Spitzer (IR) and Rosat (X-ray) aspects in the same sight lines of both the LMC and the SMC and pursue the kinematics analysis of OVI. Intervening O VI absorbers are believed to trace shock-heated gas in the ISM and may thus play a key role in our understanding about the baryonic mass existing in the local group. We plan to use *FUSE* data for doing a survey of O VI absorption measurements for the nearby intergalactic medium. For higher red shift studies, we would be using data from the *SDSS*.

All the above mentioned studies will help in providing a better understanding of the ISM of the MW. The MCs are galaxies that are similar in metallicity to galaxies at very high redshift (early type galaxies). An understanding of the ISM and the components of interstellar dust in these galaxies will act as clues to the understanding of the evolution of galaxies with low metallicity environments.

Bibliography

Adams, W. S., 1949, ApJ, 109, 354

Andersen, M. et al. 2009, ApJ, 707, 1347

Anderson, L. D. et al. 2009, ApJS, 181, 255

Asplund, M., Grevesse, N., Sauval, A. J., Allende, P. C., & Kiselman, D. 2004, A&A, 417, 751

Bakes, E. L. O., & Tielens, A. G. G. M. 1994, ApJ, 427, 822

Beals, C. S. 1936, MNRAS, 96, 661

Bernard, J. -P. et al. 2008, AJ, 136, 919

Blair, W. P. et al. 2009, PASP, 121, 634

Blum, R. D. et al. 2006, AJ, 132, 2034

Bohlin, R. C., Savage, B. D., & Drake, J. F. 1978, ApJ, 224, 132

Bohlin, R. C., Hill, J. K., Stecher, T. P., & Witt, A. N. 1982, ApJ, 255, 87

Bohren, C.F., & Huffman, D. R., 1983, Absorption and Scattering of Light by Small Particles (New York: Wiley)

Bolatto, A. D. et al. 2007, ApJ, 655, 212

Bomans, D. J., Dennerl, K., & Kurster, M. 1994, A&A, 283, L21

Bonanos, A. Z. et al. 2010, AJ, 140, 416

Bot, C., Boulanger, F., Lagache, G., Cambresy, L., & Egret, D. 2004, A&A, 423, 567

Bothun, G. D., & Thompson, I. B. 1988, AJ, 96, 877

Bouchet, P., Lequeux, J., Maurice, E., Prevot, L., & Prevot-Burnichon, M. L. 1985, A&A, 149, 330

Bowen, D. V. et al. 2008, ApJS, 176, 59

Bowyer, S. 1991, ARA&A, 29, 59

Burke, J. R., & Hollenbach, D. J. 1983, ApJ, 265, 223

Burrows, D. N., & Mendenhall, J. A. 1991, Nature, 351, 629

Cardelli, J. A., Clayton, G. C., & Mathis, J. S. 1989, ApJ, 345, 245.

Carruthers, G. 1970, ApJL, 161, L81.

Castor, J., McCray, R., & Weaver, R. 1975, ApJL, 200, L107

Chu, Y. -H., & Mac Low, M. -M. 1990, ApJ, 365, 510

Clayton, G. C., & Martin, P. G. 1985, ApJ, 288, 558

Clayton, G. C., Wolff, M. J., Sofia, U. J., Gordon, K. D., & Misselt, K. A. 2003, ApJ, 588, 871

Cohen, R. S., Dame, T. M., Garay, G., Montani, J., Rubio, M., & Thaddeus, P. 1988, ApJL, 331, L95

Cole, A. A., Nordsieck, K. H., Gibson, S. J., & Harris, W. M. 1999a, AJ, 118, 2280

Cole, A. A., Wood, K., & Nordsieck, K. H. 1999b, AJ, 118, 2292

Conti, P. S., Garmany, C. D., & Massey, P. 1986, AJ, 92, 48

Cornett et al. 1994, ApJL, 425, L117

Cornett et al. 1997, AJ, 113, 1011

Cornett, R. H., Hollis, J., & Stecher, T. P. 1997a, AIPC, 408, 55

Cox, D. P. 2005, ARA&A, 43, 337

da Cunha, E., Charlot, S, & Elbaz, D. 2008, MNRAS, 388, 1596

Danforth, C. W., Howk, J. C., Fullerton, A. W., Blair, W. P., & Sembach, K. R. 2002, ApJS, 139, 81

Danforth, C. W., & Shull, J. M. 2005, ApJ, 624, 555

Danforth, C. W., Shull, J. M., Rosenberg, J. L., & Stocke, J. T. 2006, ApJ, 640, 716

Danforth, C. W., & Blair, W. P. 2006a, ApJ, 646, 205

Davidsen, A. F. 1993, Science, 259, 327

Davies, R. D., Elliott, K. H., & Meaburn, J. 1976, MNRAS, 81, 89

Desert, F. -X., Boulanger, F., & Puget, J. L. 1990, A&A, 237, 215

Dickey, J. M., Terzian, Y., & Salpeter, E. E. 1978, ApJS, 36, 77

Dickel, J. R., Mcintire, V. J., Gruendl, R. A., & Milne, D. K. 2005, AJ, 129, 790

Dixon, W. V. D., Hurwitz, M, & Ferguson, H. C. 1996, ApJL, 469, L77

Dixon, W. V., Sallmen, S., Hurwitz, M., & Lieu, R. 2001, ApJL, 552, L69

Dixon, W. V. D., Sankrit, R., & Otte, B. 2006, ApJ, 647, 328

Dixon, W. V. et al. 2007, PASP, 119, 527

Dixon, W. V. D, & Sankrit, R. 2008, ApJ, 686, 1162

Dobashi, K., Bernard, J. P., Hughes, A., Paradis, D., Reach, W. T., & Kawamura, A. 2008, A&A, 484, 205

Dobashi, K., et al. 2009, AJ, 137, 5099

Dolphin, A. E., & Hunter, D. A. 1998, AJ, 116, 1275

Dopita, M. A., Mathewson, D. S., & Ford, V. L. 1985, ApJ, 297, 599

Draine, B. T., 1989, IAU Symposium, Interstellar Dust, edited by Allamandola, L. J. and Tielens, A. G. G. M. (Dordecht: Kluwer), 135, 313

Draine, B. T., & Weingartner, J. C. 1997, ApJ, 480 633

Draine, B. T., & Li, A. 2001, ApJ, 551, 807

Draine, B. T. 2003, ApJ, 598, 1017

Draine, B. T., & Li, A. 2007, ApJ, 657, 810

Dufour, R. J. 1984, IAU Symposium, Structure and Evolution of the Magellanic Clouds, edited by S. van den Bergh & K. S. de Boer (Dordrecht: Reidel), 108, 353

Duley, W. W., & Williams, D. A. 1980, ApJ, 242, L179

Edgar, R. J., & Chevalier, R. A. 1986, ApJ, 310, L27

Ewen, H. I., & Purcell, E. M. 1951, Nature, 168, 356

Falgarone, E., & Puget, J, -L. 1985, A&A, 142, 157

Feast, M. 1999, In New Views of the Magellanic Clouds, ed. Y. -H. Chu, N. Suntzeff, J. Hesser, & D. Bohlender, IAU Symposium, 190, 542

Feldman, P. D., Sahnow, D. J., Kruk, J. W., Murphy, E. M., & Moos, H. W. 2001, Journal of Geophysical Research, 106, 8119

Ferriere, K. M. 2001, Rev. Mod. Phys., 73, 1031

Field, G. B., Goldsmith, D. W., & Habing, H. J. 1969, ApJL, 155, 149L

FitzGerald, M. P., Stephens, T. C., & Witt, A. N. 1976 ApJ, 208, 709

Fitzpatrick, E. L., & Massa, D. 1988, ApJ, 328, 734

Fix, J. D., Craven, J. D., & Frank, L. A. 1989, ApJ, 345, 203

Friedman, S. D. et al. 2000, ApJL, 538, L39

Fukui, Y. et al. 2008, ApJS, 178, 56

Fukui, Y. et al. 1999, PASJ, 51, 745

Garmany C. D., & Walborn N. R. 1987, PASP, 99, 240

Gaustad, J. E., McCullough, P. R., Rosing, W., & Van Buren, D. 2001, PASP, 113, 1326

Grimes, J. P. et al. 2009, ApJS, 181, 272

Goldsmith, P. F., & Langer, W. D. 1978, ApJ, 222, 881

Goldsmith, P. F. 1987, In Interstellar Processes, edited by Hollenbach, D. J., & Tronson, H. A.,Jr (Reidel, Dordrecht), 51

Gordon, K. D., Clayton, G. C., Misselt, K. A., Landolt, A. U., & Wolff, M. J. 2003, ApJ, 594, 279

Gordon, K. D. et al. 2009, ApJL, 690, L76

Habing, H. J. 1968, BAIN, 19, 421

Haikala, L. K. et al. 1995, ApJ, 443, L33

Hartmann, J. 1904, ApJ, 19, 268

Hayakawa, S., Yamashita, K., & Yoshioka, S. 1969, A&SS, 5, 493

Hayes, D. S., & Latham, D. W. 1975, ApJ, 197, 593

Haynes, R. F. et al. 1991, A&A, 252, 475

Heckman, T. M., Norman, C. A., Strickland, D. K., & Sembach, K. R. 2002, ApJ, 577, 691

Henry, R. C. 1991, ARA&A, 29, 89

Henyey, L. G., & Greenstein, J. L. 1941, ApJ, 93, 70

Hilditch, R. W., Howarth, I. D., & Harries, T. J. 2005, MNRAS, 357, 304

Hildebrand, R. H., Dotson, J. L., Dowell, C. D., Schleuning, D. A. & Vaillancourt, J. E. 1999, ApJ, 516, 834

Hoopes, C. G., Sembach, K. R., Howk, J. C., Savage, B. D., & Fullerton, A. W. 2002, ApJ, 569, 233

Howk, J. C., Sembach, K. R., Savage, B. D., Massa, D., Friedman, S. D., & Fullerton A. W. 2002a, ApJ, 569, 214

Howk, J. C, Savage, B. D., Sembach, K. R., & Hoopes, C. G. 2002b, ApJ, 572, 264

Hurwitz, M., Bowyer, S. & Martin, C. 1991, ApJ, 372, 167

Hutchings, J.B. 1982, ApJ, 255, 70

Indebetouw, R., & Shull J. M. 2004, ApJ, 605, 205

Indebetouw, R. et al. 2009, ApJ, 694, 84

Israel, F. P., de Graauw, Th., Van de Stadt, H., & de Vries, C. P. 1986, ApJ, 303, 186

Ita, Y. et al. 2004, MNRAS, 347, 720

Jakobsen, P., Bowyer, S., Kimble, R., Jelinsky, P., Grewing, M.,Kramer, G., & Wulf-Mathies, 1984, A&A, 139, 481

Jakobsen, P., de Vries, J. S., & Paresce, F. 1987, A&A, 183, 335

Jenkins, E. B., & Meloy, D. A. 1974, ApJL, 193, L121

Jenkins, E. B. 1978a, ApJ, 219, 845

Jenkins, E. B. 1978b, ApJ, 220, 107

Jenkins, E. B. 1987, In Interstellar Processes, edited by Hollenbach, D. J., & Tronson, H. A.,Jr (Reidel, Dordrecht), (Reidel, Dordrecht), p. 533

Joubert, M., Masnou, J. L., Lequeux, J., Deharve, J. M., & Cruvellier, P. 1983, A&A, 128, 114

Jura, M. 1980, ApJ, 241, 965

Kato, D. et al. 2007, PASJ, 59, 615

Kennicutt, R. C. Jr., & Hodge, P. W. 1986, ApJ, 306, 130

Kim, S. -H, & Martin, P. G. 1995, ApJ, 444, 293

Kim, S., Staveley-Smith, L., Dopita, M. A., Freeman, K. C., Sault, R. J., Kesteven, M. J., & McConnell, D. 1998, ApJ, 503, 674

Kim, S., Staveley-Smith, L., Dopita, M. A., Sault, R. J., Freeman, K. C., Lee, Y., & Chu, Y. -H. 2003, ApJS, 148, 473

Koornneef, J., & Code, A. D. 1981, ApJ, 247, 860

Koornneef, J. 1982, ApJ, 107, 247

Kulkarni, S. R., & Heiles, C. 1987, in Interstellar Processes, edited by Hollenbach, D. J., & Tronson, H. A.,Jr (Reidel, Dordrecht), 87

Kurucz, R. L. 1992, The Stellar Populations of Galaxies, ed. B. Barbuy, & A. Renzini (Dordrecht: Kluwer), IAU Symposium, 149, 225

Law, K. H., Gordon, K. D., & Misselt, K. A. 2011, ApJ, 738, 124

Lampton, M., Margon, B., & Bowyer, S. 1976, ApJ, 208, 177

Lee, D. -H. et al. 2006, ApJL, 644, L181

Leger, A., & Puget, J. L. 1984, A&A, 137, L5

Lehner, N., Fullerton, A. W., Sembach, K. R., Massa, D. L., & Jenkins, E. B. 2001, ApJ, 556, L103

Lehner, N., Fullerton, A. W., Massa, D., Sembach, K. R., & Zsargo, J. 2003, ApJ, 589, 526

Lehner, N., & Howk, J. C. 2007, MNRAS, 377, 687

Leinert, C. et al. 1998, A&AS, 127, 1

Lequeux, J., Maurice, E., Prevot-Burnichon, M. -L., Prevot, L., & Rocca-Volmerange, B. 1982, A&A, 113, L15

Lequeux, J., 2004, The Interstellar medium, (Springer) 91-108

Leroy, A., Bolatto, A., Stanimirovic, S., Mizuno, N., Israel, F., & Bot, C. 2007, ApJ, 658, 1027

Li, A., & Greenberg, J. M. 1997, A&A, 323, 566

Li, A., & Draine, B. T. 2001, ApJ, 550, 213L

Li, A., & Draine, B. T. 2002, ApJ, 576, 762

Lillie, C. F., & Witt, A. N. 1969, ApJL, 3, 201L

Lucke, P. B., & Hodge, P. W. 1970, AJ, 75,171

Luks, Th., & Rohlfs, K. 1992, A&A, 263, 41

Maloney, P. & Black, J. H. 1988, ApJ, 325, 389

Malumuth, E. M., & Heap, S. R. 1994, AJ, 107, 1054

Malumuth, E. M., Waller, W. H., & Parker, J. Wm. 1996, AJ, 111, 1128

Martin, N., Maurice., E., & Lequeux, J. 1988, A&A, 215, 219

Martin, C., Hurwitz, M., & Bowyer, S. 1990b, ApJ, 354, 220

Martin, P. G., & Whittet, C. C. B. 1990a, ApJ, 357, 113

Maucherat-Joubert, M., Lequeux, J., & Rocca-Volmerange, B. 1980a, A&A, 86, 299

Maucherat-Joubert, M., Deharveng, J. M., & Cruvellier, P. 1980b, A&A, 88, 323

Massey, P., Parker, J. W., & Garmany, C. D. 1989, AJ, 98, 1305

Massey, P., Lang, C. C., Degioia-Eastwood, K., & Garmany, C. D. 1995, ApJ, 438, 188

Massey, P., & Hunter, D. A. 1998, ApJ, 493, 180

Massey, P. 2002, ApJS, 141, 81

Mathis, J. S., Rumpl, W., & Nordsieck, K. H. 1977, ApJ, 217, 425

Mathis, J. S. 1990, ARA&A, 28, 37

Mathis, J. S. 1996, ApJ, 472, 643

McCray, R., & Snow, T. P., Jr. 1979, ARA&A, 17, 213

Meaburn, J. 1980, MNRAS, 192, 365

Meier, R. R. 1991, SSR, 58, 1

Meixner, M. et al. 2006, AJ, 132, 2268

Misselt, K. A., Clayton, G. C., & Gordon, K. D. 1999, ApJ, 515, 128

Mizuno, N., Rubio, M., Mizuno, A., Yamaguchi, R., Onishi, T., & Fukui, Y. 2001, PASJ, 53, 45

Moffat, A. F. J., Niemela, V. S., & Marraco, H. G. 1990, ApJ, 348, 232

Moos, H. W. et al. 2000, ApJ, 538, 1

Murthy, Jayant, Hall, D., Earl, M., Henry, R. C., & Holberg, J. B. 1999, ApJ, 522, 904

Murthy, Jayant, & Sahnow, D. J. 2004, ApJ, 615, 315

Murthy, Jayant 2008, A&SS, 320, 21

Murthy, J., Henry, R. C., & Sujatha, N. V. 2010, ApJ,692, 1333

Nandy, K., & Morgan, D. H. 1978, Nature, 276, 478

Oegerle, W. R., Jenkins, E. B., Shelton, R., Bowen, D. V., & Chayer, P. 2005, ApJ, 622, 377

Onaka, T., & Kodaira, K. 1991, ApJ, 379, 532

Page, T., & Carruthers, G. R. 1981, ApJ, 320, 609

Paradis, D. et al. 2009, ApJ, 138, 196

Paresce, F., & Jakobsen, P. 1980, Nature, 288, 119

Paresce, F., McKee, C.F., & Bowyer, S. 1980a, ApJ, 240, 387

Paresce, F. 1990, in IAU Symp. 139, The Galactic and Extragalactic Background Radiation, ed. S. Bowyer & C. Leinert (Dordrecht: Kluwer), 307

Parker, J. W. 1992, PASP, 104, 1107

Parker, J. W. 1993, SSR, 66, 55

Parker, J. W., & Garmany, C. D. 1993a, AJ, 106, 1471

Parker, J. Wm. et al. 1998, AJ, 116, 180

Parravano, A., Hollenbach, D. J., & McKee, C. F. 2003, ApJ, 584, 797

Pei, Y. C. 1992, ApJ, 395, 130

Perault, M., Lequeux, J., Hanus, M., & Joubert, M. 1991, A&A, 246, 243

Points, S. D., Chu, Y.-H., Snowden, S. L., & Smith R. C. 2001, ApJS, 136, 99

Pradhan, A. C., Pathak, A., & Murthy, Jayant 2010, ApJL, 718, L141

Prevot, M. L., Lequeux, J., Maurice, E., Prevot, L., & Rocca-Volmerange, B. 1984, A&A, 132, 389

Reynolds, R. J. 1985, ApJ, 294, 256

Reynolds, R. J. 1987, ApJ, 323, 118

Rousseau, J., Martin N., Prevot, L., Rebeirot, E., Robin, A., & Brunet, J. P. 1978, A&AS, 31, 243

Roesler, F. L., Reynolds, R., Scherb, J. F., & Ogden, P. M. 1978, In High Resolution Spectroscopy, Proceedings of the Fourth Colloquium on Astrophysics of the Trieste Observatory, edited by M. Hack (Osservatorio Astronomico di Trieste, Trieste), p. 600

Rubio, M., Garay, G., Montani, J., & Thaddeus, P. 1991, ApJ, 368, 173

Sahnow, D. J. et al. 2000, ApJ, 538, 7

Sakon, I. et al. 2006, ApJ, 651, 174

Sankrit, R., & Dixon, W. V. D. 2007, PASP, 119, 284

Sasseen, T. P., Deharveng, J.-M. 1996, ApJ, 469, 691

Sauvage, M., Vigroux, L., & Thuan, T. X. 1990, A&A, 237, 296

Savage, B. D., & Sembach, K. R. 1991, ApJ, 379, 245

Savage, B. D. et al. 2000, ApJ, 538, L27

Savage, B. D. et al. 2003, ApJS, 146, 125

Savage, B. D., & Lehner, N. 2006, ApJS, 162, 134

Schiminovich, D., Friedman, P. G., Martin, C., & Morrissey, P. F. 2001, ApJL, 563, L161

Schlegel, D. J., Finkbeiner, D. P., & Davis, M. 1998, ApJ, 500, 525

Schwering, P. B. W., & Israel, F. P. 1989, A&AS, 79, 79

Scoville, N. Z., & Sanders, D. B. 1987, In Interstellar Processes, edited by D. J. Hollenbach and H. A. Thronson, Jr. (Reidel, Dordrecht), 21

Sellgren, K., Allamandola, L. J., Bregman, J. D., Werner, M. W., & Wooden, D. H. 1985. ApJ, 299, 416

Sembach, K. R., & Savage, B. D. 1992, ApJS, 83, 147

Sembach, K. R., 1999, in Gibson, B. K., Putman, M. E. eds., ASP Conf. Ser. 166, Stromlo Workshop on High Velocity Clouds (San Francisco:ASP), 243

Seon, Kwang-Il, Edelstein, J., Korpela, E., Witt, A., Min, Kyoung-Wook, Han, W., Shinn, J., Kim, Il-Joong, Park, Jae-W. 2011, ApJS, 196, 15S

Serkowski, K., Mathewson, D. S., & Ford, V. L. 1975, ApJ, 196, 261

Shelton, R., & Cox, D. P. 1994, ApJ, 434, 599

Shelton, R. L. et al. 2001, ApJ, 560, 730

Shelton, R. L. 2002, ApJS, 569, 758

Shelton, R. L., Sallmen, S. M., & Jenkins, E. B. 2007, ApJ, 659, 365 (2007)

Simon, J. D. et al. 2007, ApJ, 669, 327

Sivan, J. P. 1974, A&AS, 16, 163

Slavin, J. D., & Frisch, P. C. 2002, ApJ, 565, 364

Smith, A. M., & Stecher, T. P. 1971, ApJL, 164, L43

Smith, A. M., Cornett, R. H., & Hill, R. S. 1987, ApJ, 320, 609

Smith, L. F., Shara, M. M., & Moffat, A. F. J. 1990, ApJ, 358, 229

Smith, L. F., Shara, M. M., & Moffat, A. F. J. 1996, MNRAS, 281, 163

Snowden, S. L., & Petre, R. 1994, ApJL, 436, L123

Spitzer, L. 1956, ApJ, 124, 20

Spitzer, L., Jr. 1990, ARA&A, 28, 71

Stanimirovic, S. et al. 2000, MNRAS, 315, 791

Stecher, T. P. et al. 1997, PASP, 109, 584

Sturm, E. et al. 2000, A&A, 358, 481

Sujatha, N. V., Shalima, P., Murthy, J., & Henry, R. C. 2004, BASI, 32, 151

Sujatha, N. V., Chakraborty, P., Murthy, J., & Henry, R. C. 2005, ApJ, 633, 257

Sujatha, N. V., Shalima, P., Murthy, J., & Henry, R. C. 2007, ApJ, 665, 363

Sujatha, N. V.,Murthy, J., Karnataki, A., Henry, R. C., & Bianchi, L. 2009, ApJ,692, 1333

Sujatha, N. V., Murthy, J., Suresh, R., Henry, R. C., & Bianchi, L. 2010, ApJ,723, 1549

Tielens, A. G. G. M., Allamandola, L. J., Barker, J. R., & Cohen, M. 1987, In Polycyclic Aromatic Hydrocarbons and Astrophysics, edited by A. Leger, L. d'Hendecourt, & N. Boccara (Dordrecht: Reidel), 273

Tielens, A. G. G. M, & Allamandola, L., J. 1987, In Interstellar Processes, edited by D. J. Hollenbach and H. A. Thronson, Jr. (Reidel, Dordrecht), 397

Torres-Dodgen, A. V., & Massey, P. 1988, AJ, 96, 1076

Townsley, L. K., Broos, P. S., Feigelson, E. D., Garmire, G. P., & Getman, K. V. 2006, AJ, 131, 2164

Trumper, J. et al. 1991, Nature, 349, 579

Trumpler, R. J. 1930, Lick Obs. Bull., 420, 154

Tumlinson, J. et al. 2002, ApJ, 566, 857

van der Marel, R. P., & Cioni, M. -R. L. 2001, AJ, 122, 1807

van der Marel, R. P., Alves, D. R., Hardy, E. S., & Nicholas, B. 2002, AJ, 124, 2639

Vangioni-Flam, E., Lequeux, J., Maucherat-Joubert, M., & Rocca-Volmerange, B. 1980, A&A, 90, 73

Van Steenberg, M. E., & Shull J. M. 1988, ApJ, 330, 942

Vermeij, R., Peeters, E., Tielens, A. G. G. M., & van der Hulst, J. M. 2002, A&A, 382, 1042

Wakker, B. P. et al. 2003, ApJS, 146, 1

Walborn, N. R. 1977, ApJ, 215, 53

Walborn, N. R., Ebbets, D. C., Parker, J. Wm., Nichols-Bohlin, J., & White, R. L. 1992, ApJL, 393, L13

Walborn, N. R., Lennon, D. J., Haser, S. M., Kudritzki, R. -P., & Voels, S. A. 1995, PASP, 107, 104

Walborn, N. R., & Blades, J. C. 1997, ApJS, 112, 457

Walborn, N. R., Lennon, D. J., Heap, S. R., et al. 2000, PASP, 112, 1243

Walborn, N. R. et al. 2002a, AJ, 123, 2754

Walborn, N. R. et al. 2002b, ApJS, 141, 443

Wang, Q., Hamilton, T., & Helfand, D. J. 1989, Nature, 341, 309

Wang, Q., Hamilton, T., Helfand, D. J., & Wu, X. 1991, ApJ, 374, 475

Weaver, R., McCray, R., Castor, J., Shapiro, P., & Moore, R. 1977, ApJ, 218, 377

Weingartner, J. C., & Draine, B. T. 2001, ApJ, 548, 296

Weller, C. 1983, ApJ, 268, 899

Welsh, B. Y. et al. 2007, A&A, 472, 509

Welsh, B. Y., & Lallement, R. 2008, A&A, 490, 707

Werner, M. W., Silk, J., & Rees, M, J. 1970, ApJ, 161, 965

Westerlund, B. E. 1997, The Magellanic Clouds (New York: Cambrige Univ. Press), 122, 1807

Whitney, B., et al. 2008, AJ, 136, 18

Whittet, D. C. B. 2003, IOP series in Astronomy and Astrophysics, Dust in Galactic Environment, 390

Wilke, K., Stickel, M., Haas, M., Herbstmeier, U., Klaas, U. & Lemke, D. 2003, A&A, 401, 873

Wilking, B. A., Lebofsky, M. J., & Rieke, G. H. 1982, AJ, 87, 695

Witt, A. N., & Gordon, K. D. 2000, ApJ, 528, 799

Wolfire, M. G., Hollenbach, D., McKee, C. F., Tielens, A. G. G. M., Bakes, E. L. O. 1995, ApJ, 443, 152

Wright, E. L. 1992, ApJ, 391, 34

Yan, Z. -C., Tambasco, M., & Drake, G. W. F. 1998, Phys. Rev. A, 57, 1652

Yao, Y., Wang, Q. D., Hagihara, T., Mitsuda, K., McCammon, D., & Yamasaki, N. Y. 2009, ApJ, 690, 143

Zaritsky, D., Harris, J., Thompson, I. B., & Grebel, E. K. 2004, AJ, 128, 1606